Silicon Photonics Devices with Sub-wavelength Grating Waveguides

A THESIS

submitted by

SUMI R

for the award of the degree

of

DOCTOR OF PHILOSOPHY

DEPARTMENT OF ELECTRICAL ENGINEERING.
INDIAN INSTITUTE OF TECHNOLOGY MADRAS.

Tuesday 10th March, 2020

THESIS CERTIFICATE

This is to certify that the thesis titled **Silicon Photonics Devices with Sub-wavelength Grating Waveguides**, submitted by **SUMI R.**, to the Indian Institute of Technology Madras, for the award of the degree of **Doctor of Philosophy**, is a bonafide record of the research work done by her under our supervision. The contents of this thesis, in full or in parts, have not been submitted to any other Institute or University for the award of any degree or diploma.

Prof. Bijoy Krishna Das
Research Guide
Professor
Dept. of Electrical Engineering
IIT-Madras, 600 036

Prof. Nandita DasGupta
Research Co-Guide
Professor
Dept. of Electrical Engineering
IIT-Madras, 600 036

Place: Chennai, India
Date: Tuesday 10th March, 2020

"If we knew what it was we were doing, it wouldn't be called research, would it?"

- Albert Einstein

Dedicated to my beloved **Parents**

and loving **Husband**

ACKNOWLEDGEMENTS

My PhD journey has been a truly transforming experience and it was possible with the guidance and endless support that I received from many people.

First and foremost, I would like to extend my sincere gratitude to my research guide Prof. Bijoy Krishna Das for introducing me to this exciting field of Silicon Photonics and for his guidance, encouragement and continuous support throughout my PhD. He has always inspired me by his hardworking and passionate attitude towards research and his strive towards achieving high quality work.

I am highly indebted to my research co-guide Prof. Nandita DasGupta for her guidance and encouragement. I feel privileged to be associated with a person like her during my PhD.

I would like to thank Prof. C Vijayan who gave me the flavour of research and motivated me to pursue PhD.

I would like to acknowledge the members of my Doctoral Committee, Prof. Enakshi Bhattacharya, Dr. Ananth Krishnan and Dr. Manu Jaiswal for their valuable comments and suggestions during the review meetings.

I would like to acknowledge the Center for NEMS and Nanophotonics (CNNP), IIT Madras for providing world-class fabrication facilities. I thank all the technicians and staff members in the MEMS and Microelectronics Lab for all the technical help provided during fabrication of devices.

I thank Dr. K V Reddy for providing financial assistance to attend conference in USA as well as hosting me and my husband during our stay in USA.

My sincere gratitude goes to all my fellow labmates in integrated optoelectronics group who made my stay a memorable and fruitful experience. I thank Dr. Sujith for his scientific inputs, personal helps and friendly nature. I thank Meenatchi Sundaram

for introducing me to the fabrication labs and teaching me with lot of patience. My heartfelt thanks to Siddharth, Saket, Sireesha, Dadavali, Mani Teja, Riddhi and Ramesh for creating a wonderful working atmosphere in lab. Riddhi was the first person I met in the group and I thank her for being a friend whom I can always count on no matter what. Ramesh was always there to help me, right from doing experiments to giving me company for going home. My heartfelt thanks to my seniors Dr. Santhanu, Dr. Parimal, Rashmi, Sreevatsa, Vivek and Seethalakshmi for their guidance and moral support. I thank all my fellow labmates in Integrated Optoelectronics group, Arnab, Meena, Suvarna, Ram Mohan, Ashithosh, Pratyasa, Anushka, Vishnu, Vinoth and Malu for their wishes and encouragements and I wish them all the best in their future endeavours. A special mention of thanks to my friends outside of IO group, Anusha, Manu, Nidhin and Prashant.

I would like to express my deepest gratitude to my Pappa and Mummy for believing in me and giving me emotional support, no matter which path I chose in life. Words are not enough to say how grateful I am to both of you. My heartfelt regards goes to my father-in-law and mother-in-law for their love and support. I also thank my best friend, Tresa for her prayers and encouragement.

Saving the most important to the last, I wish to express heartfelt thanks to my dear husband, Sterin, whose patience, unconditional love and constant support enabled me to complete this thesis. Your words of encouragement have helped me to keep things in perspective whenever I thought that it was impossible to continue.

ABSTRACT

KEYWORDS: Silicon Photonics, Silicon-on-Insulator, Waveguides, Integrated Optics, Sub Wavelength Gratings, Optical Filters, Lab-on-chip Sensor, Mach-Zehnder Interferometers, Thermo-optic Switch.

In the recent past, sub-wavelength grating (SWG) waveguide in silicon-on-insulator (SOI) platform has emerged as an important component for silicon photonics technology due to its flexibility in engineering the effective refractive index and dispersion characteristics of the guided mode. Most of the demonstrations in SWG primarily deal with improving the performance of the conventional silicon photonic devices like wavelength independent directional couplers, high Q ring resonators, low loss waveguide crossings, mode converters etc. by replacing the straight/bent waveguide sections with SWG waveguides. Integrated SWG waveguides are also being investigated for various applications like refractive index sensing, wavelength filtering, delay lines etc. Nevertheless, most of the SWG based filters demonstrated till date have limited spectral bandwidth and are suitable for narrow-band add-drop multiplexing. For improved transmission capacity and spectral efficiency, it is desirable to have on-chip tunable optical flat-top filters which can either switch, route or duplex a large bandwidth of optical signal. In the field of refractive index sensing, SWG based integrated photonic sensors reported so far are limited to wavelength interrogation mechanisms which require expensive equipment like spectrum analyzers. Integrated Mach-Zehnder interferometer (MZI) is a less expensive alternative for sensing via intensity dependent interrogation. However, there has been no demonstration of SWG integrated MZI sensors. This PhD thesis intends to extend the prospects of integrated SWG waveguides in silicon photonics platform for on-chip filtering and sensing applications that could address the pitfalls in the existing state of the art and specifically cater to the recent advancements in this field. All the devices are demonstrated using SOI substrate with device layer thickness of 220 nm, buried oxide (BOX) layer thickness of 2 μm, and handle wafer thickness of

500 μm; which is commonly used in silicon photonics foundries.

We first demonstrated an integrated optical ultra wide-band add-drop filter/switch circuit designed by integrating two identical SWG waveguides in two arms of a 2×2 MZI. The circuit is designed such that successive stopband and passband can be separated into the drop port and cross/bar port of the MZI, respectively. They are designed to operate in TE-polarization with a well defined band-edge wavelength $\lambda_{edge} \sim 1565$ nm (roll-off > 70 dB/nm). The band-edge wavelength could be thermo-optically tuned with a slope efficiency of 22 pm/mW. The passband switching between bar- and cross port is demonstrated with more than 15 dB extinction and the measured switching power $P_{\pi} \sim 54$ mW. Thermo-optic modulation is also demonstrated simultaneously at cross-, bar- and drop ports for an operating wavelength λ = 1571 nm (slightly above λ_{edge}). The rise-time and fall-time in thermo-optic modulation is recorded as $\sim$5 μs and $\sim$4 μs, respectively.

In addition, we have explored the capability of an apodized SWG waveguide to achieve improved filter functionalities. The filter band-edge exhibits smooth roll-off with a stopband extinction > 40 dB. The typical edge slope of ~ 3.5 dB/nm is obtained for SWG waveguide with grating length L_g = 70 μm and width W_g = 2.5 μm. The position and slope of the band-edge can be engineered by tailoring SWG waveguide width and length, respectively.

This is followed by the experimental demonstration of a refractive index sensor device designed by integrating a SWG waveguide in one of the arms of a MZI. The phase difference between guided lightwaves through the sensing and reference arms are engineered to remain nearly constant for a desired range of wavelengths (at $\lambda \sim 1550$ nm). The devices operating at these wavelengths exhibit a sensitivity of $\sim$ 5 dB/0.01 change in clading refractive index, which is again linearly scalable with the sensing arm length of the proposed MZI.

TABLE OF CONTENTS

LIST OF TABLES

LIST OF FIGURES

ABBREVIATIONS

Acronyms

BOX	Buried Oxide
BW	Bandwidth
CMOS	Complementary Metal Oxide Semiconductor
DC	Directional Coupler
DI	De-ionized (water)
DSO	Digital Storage Oscilloscope
DUT	Device Under Test
EBL	Electron Beam Lithography
ER	Extinction Ratio
FBMS	Fixed Beam Moving Stage
FG	Function Generator
FSR	Free Spectral Range
GC	Grating Coupler
GDS-II	Graphic Database System-II (mask file format)
HSQ	Hydrogen Silsesquioxane
ICPRIE	Inductively Coupled Plasma Reactive Ion Etching
IL	Insertion Loss
OSA	Optical Spectrum Analyzer
PD	Photodetector
PIC	Photonic Integrated Circuit
PMMA	Poly(methyl methacrylate)
MMI	Multi-Mode Interference
MRR	Microring Resonator
MZI	Mach-Zehder Interferometer
SEM	Scanning Electron Microscope
SMF	Single Mode Fiber

SMU	Source Measure Unit
SOI	Silicon-on-Insulator
SWG	Sub-Wavelength Grating
TE	Transverse Electric (polarization)
TM	Transverse Magnetic (polarization)
WDM	Wavelength Division Multiplexing
WIDC	Wavelength Independent Directional Coupler

Chemical Names

CHF_3	Tri-fluoro Methane
HF	Hydrofluoric Acid
HNO_3	Nitric Acid
H_2O	Water
H_2O_2	Hydrogen Peroxide
H_2SO_4	Sulphuric Acid
NH_4OH	Ammonium Hydroxide
SF_6	Sulfur Hexafluoride
Si	Silicon
SiO_2	Silicon dioxide
TCE	Tri-chloro Ethylene

Units

dB	decibel
dBm	decibel milli-watt
K	Kelvin
µm	micrometer
µW	micro watt
µs	microsecond
mW	milli watt
mbar	milli-bar
ml	milli-litre
mTorr	milli-Torr (of pressure)

nm	nanometer
ns	nanosecond
sccm	standard cubic centimeter per minute

NOTATIONS

$\mathbf{n}$	Refractive index
$\mathbf{n}_{eff}$	Effective refractive index
$\boldsymbol{\epsilon}$	Permitivity
$\boldsymbol{\lambda}$	Wavelength
$\boldsymbol{\beta}$	Propagation constant
$\boldsymbol{\phi}$	EM wave phase
$\boldsymbol{\kappa}$	Coupling coefficient
$\boldsymbol{S_H}$	Thermal sensitivity
W_g	SWG grating width
Λ	Grating period
δ	Grating Duty-cycle
H	Silicon device layer thickness
h	Silicon slab thickness
t_{BOX}	Buried oxide thickness
S_b	Bulk sensitivity

CHAPTER 1

Introduction

Sub-wavelength grating (SWG) is emerging as a promising waveguiding technology for silicon photonics in realizing high performance and compact integrated photonic devices and circuits for on-chip optical interconnects, quantum photonics and sensing applications. SWG waveguide demonstrations till date are enriched with devices that tailor the light properties for efficient power coupling, polarization control, phase engineering, wavelength filtering etc. This PhD thesis intends to explore and extend the capability of SWG waveguides by coming up with device demonstrations that can be used to realize more complex photonic integrated circuits (PIC) with improved features or new functionalities. In particular, the filtering and sensing prospects of SWG waveguides are explored and the devices are designed keeping in mind the feasibility of on-chip integration with the already demonstrated devices in our research group such as broadband power splitters, efficient grating couplers, thermo-optic phase shifters etc. All the devices discussed in this thesis are designed, fabricated and characterized using the in-house facilities available at IIT Madras. In this introductory chapter, we present the motivation for carrying out present research through an exhaustive literature review, which eventually streamlines the objectives and a brief overview on the organization of the remaining chapters.

1.1 Motivation

Silicon photonics is currently one of the most active disciplines in academia as well as industry in view of its immense potential in bonding two technological areas that have transformed the last century - electronics and photonics [1]. In pre-silicon-photonics era, stand-alone photonic devices were realized in various material platforms; for example, indium phosphide for lasers [2], lithium niobate for modulators [3, 4, 5] and Germanium and III-V semicunductors for photodetectors [6, 7]. Naturally, the significant

portion of the final manufacturing cost for these devices arises from the photonic packaging processes making them suitable for application specific fiber-optic systems. The advent of CMOS compatible silicon photonics technology has opened up the feasibility for large-scale photonics integration as well as futuristic co-integration with electronic driver circuits and processors. The early works which served as key technology milestones in the field of silicon photonics began in the mid of 1980's when Soref et al. proposed silicon as a material platform for integrated photonics [8, 9, 10]. As early as 1992, Abstreiter conceived the concept of opto-electronic integrated circuits (OEIC) where he envisioned the integration of photonic structures with advanced silicon microelectronics on the same substrate [11]. This was extended by Soref in the following year by proposing a visionary concept, which he named as 'superchip' using silicon based optical waveguides on a silicon bench, as shown in Figure 1.1 [12]. In the scheme, all the

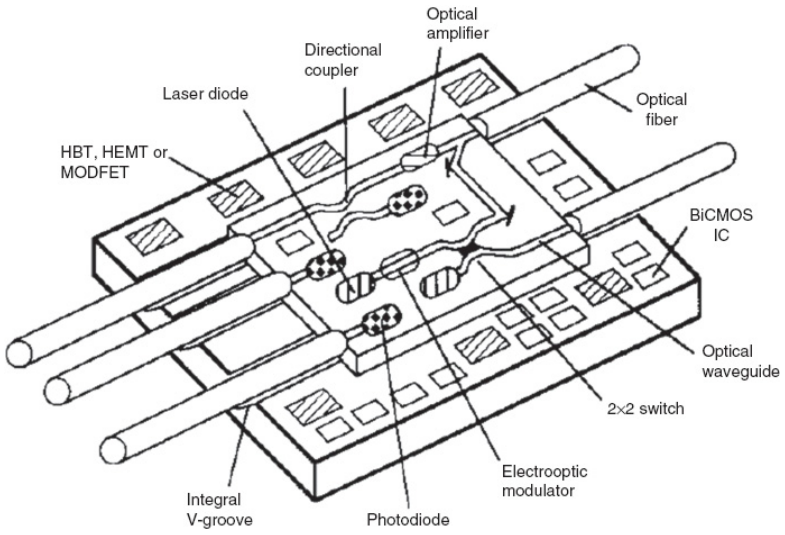

Figure 1.1: Schematic illustration of Opto-Electronic Integrated Circuit (OEIC) "superchip" envisioned by Soref [12]

fundamental blocks, photodiode, modulator, switch, laser diode, integrated waveguides and couplers can be seen sharing a single platform. The design places fibers on etched V-grooves of the substrate to butt-couple into the chip: which is still a challenging task. Among the various substrate configurations studied, such as, silicon-on-sapphire (SOS) [13], silicon germanium [14] and SOI [15], the SOI platform became the most popular for silicon based waveguide systems. Since then, silicon photonics had no look back and over the past few decades, the silicon photonics community has made tremendous progress in developing a wide variety of photonic devices for building complex pho-

tonic integrated circuits (PICs) such as low-loss optical waveguides [16], high speed modulators [17, 18, 19, 20], high speed switches [21, 22, 23] and tunable or reconfigurable optical filters [24], etc. These research advancements paved the way towards the evolution of photonic integration for realizing high performance systems on-chip. Microprocessor circuits that could communicate with other chips using on-chip photonic devices were demonstrated in SOI substrate as shown on Figure 1.2 [25]. It comprised

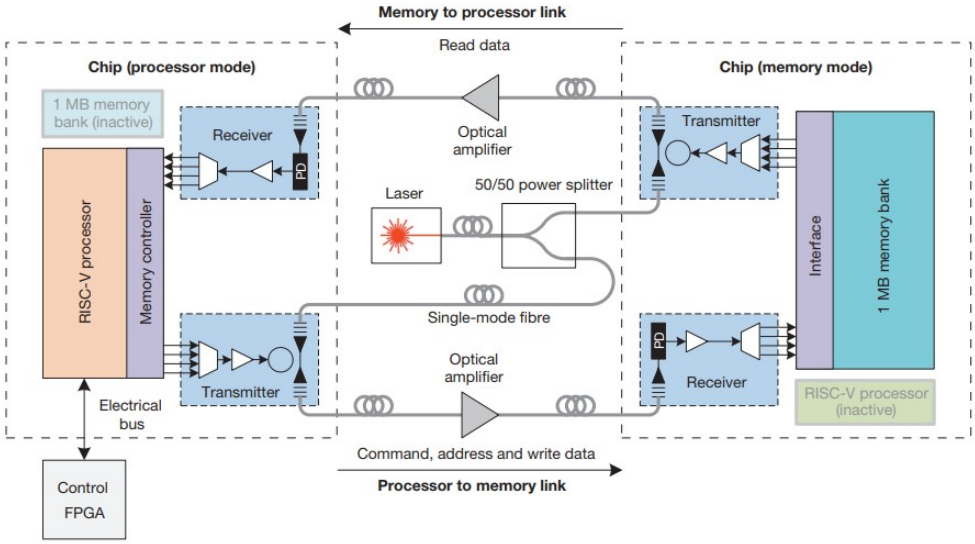

Figure 1.2: Block diagram of optical memory system that uses optical links to communicate between two chips [25].

of 70 million transistors and 850 photonic components co-integrated using standard microelectronics foundry process. In April 2018, two papers were published almost simultaneously in Nature and Science journals reporting dense electronic-photonics co-integration on a bulk chip [26] and large scale silicon photonics quantum circuit [27], respectively. The former enabled the monolithic integration of photonic components like optical waveguides, grating couplers, micro-ring modulators and avalanche photodetectors into a CMOS chip which is housing analog and digital electronics as shown in Figure 1.3. The photonic components are made of a thin layer of polycrystalline silicon deposited on silicon dioxide islands in trenches within the bulk CMOS chip. This integration approach enabled the addition of optical components to existing chips with little modification of their designs. On the other hand, the on-chip quantum photonic circuit demonstrates the on-chip generation and manipulation of entangled quantum states having potential applications in information processing and quantum communications as shown in Figure 1.4. Approximately 550 photonic components are integrated

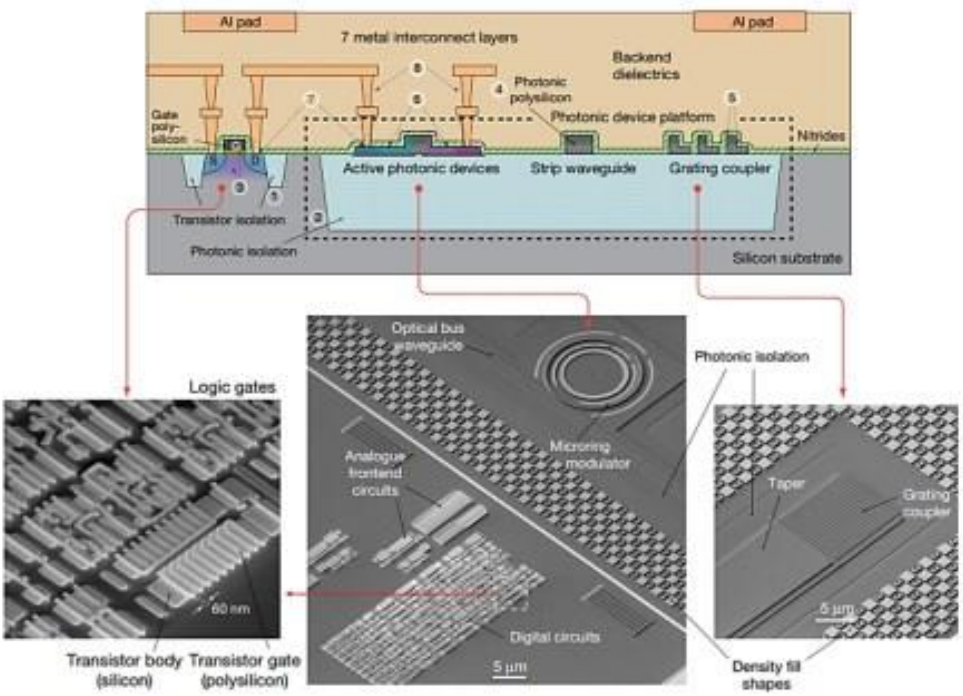

Figure 1.3: (Top): Schematic illustration of the Electronic-Photonic chip with the photonic devices realized in polysilicon film (220 nm) deposited on a photonic trench isolation. The numbers indicate the order in which fabrication process steps are carried out. (Bottom): SEM images of various electronic and photonic components in the monolithic platform [26].

monolithically on a single chip including 16 photon sources, 93 thermo-optic phase shifters, 256 waveguide crossings, 122 MMI beam-splitters and 64 grating couplers. It is evident from the demonstration of large-scale integrated optical devices that silicon photonics technology has become a matured platform to enable on-chip generation, manipulation and analysis of multidimensional quantum systems. Significant research effort has also been invested in developing short-reach optical interconnects, such as data centers and high-performance computing in order to meet the demand for rapidly increasing data transfer rate, owing to their inherent advantages over their electrical counterparts in terms of bandwidth, distance, and power consumption [28]. Electronic giant Intel recently announced that it had expanded its 100 G silicon photonics products from data centers to the 5G network edge. Intel's 400G products are expected to enter volume production in the second half of 2019 [29]. Acacia Communications has recently released AC200-CFP2-LH module targeted for long-haul dense wavelength division multiplexing (DWDM) networks that can reach upto 2500 km [30]. Besides data communication, silicon photonics integrated circuit technology has become a promis-

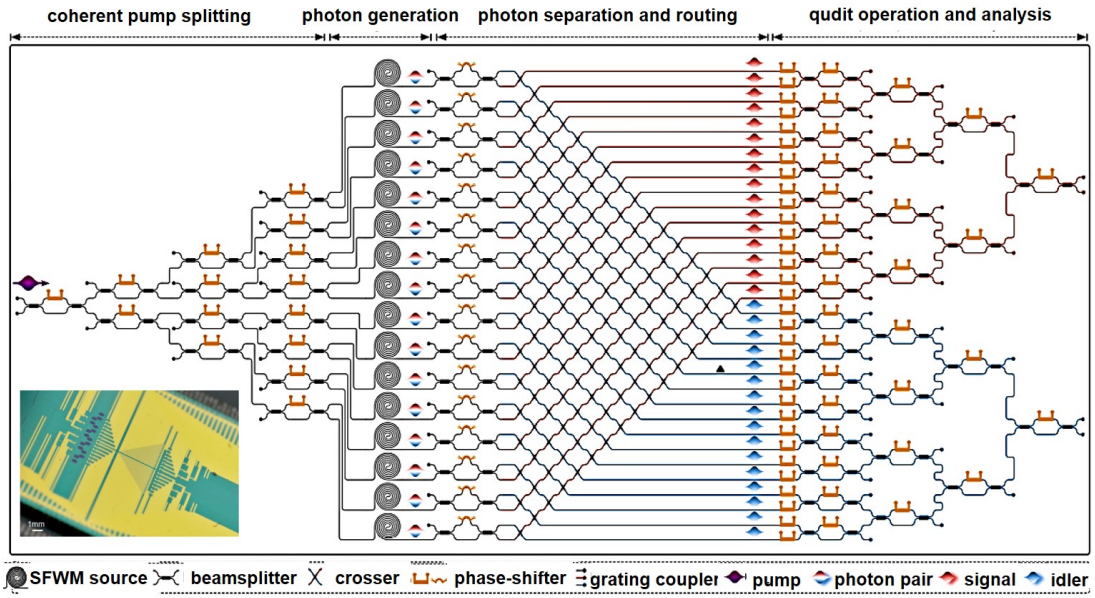

Figure 1.4: Circuit diagram of the multifunctional silicon quantum photonic chip. The inset shows the photograph of the fabricated device [27].

ing platform for realizing label-free optical sensors for point of care diagnosis [31, 32]. Apart from CMOS compatibility, the high refractive index contrast between silicon and the surrounding media facilitates the development of multiple compact sensing devices on a single chip. The major sensing mechanisms that are generally used in integrated optical sensors are a) refractive index (RI) sensing [33]; b) absorption sensing [34]; and c) fluorescence sensing [35, 36]. Among these, silicon photonic bio-sensors rely primarily on RI sensing wherein the evanescent field of the near infrared wavelengths light confined within nano-meter scale silicon waveguides interact with the surrounding volume thereby creating an external RI sensitive region as shown in Fig.1.5 [37]. This change in effective refractive index is translated into a measurable quantity de-

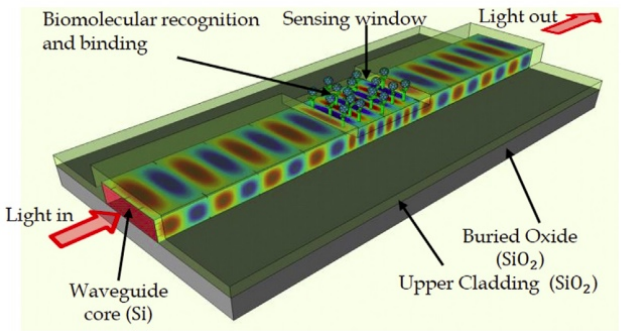

Figure 1.5: Silicon photonic wire waveguide for bio-sensing [37].

pending on the device configuration, say, resonant wavelength in microring/microdisk

resonators [38, 39, 40], photonic crystal cavity [41] or Bragg grating resonators [42] and output power intensity in interferometric structures [43].

Silicon waveguide is the fundamental and indispensable framework for building any silicon photonics device for the aforementioned applications. Significant research effort has been devoted in this area since its first report by Soref et al. in 1980s [8, 9]. The schemes of different kinds of waveguides realized in SOI platform is shown in Figure 1.6. The standard and conventional waveguides used for silicon photonics are strip

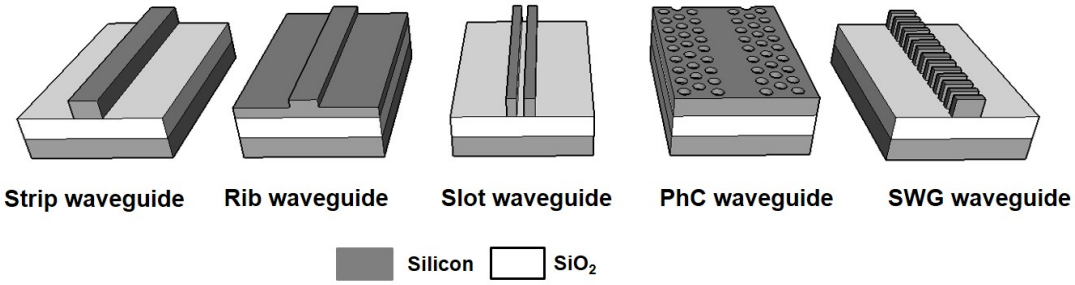

Figure 1.6: Schematic 3D view of various optical waveguides realized in SOI platform.

waveguide and rib waveguide, in which the light is confined primarily within the silicon region having higher refractive index based on the total internal reflection [16, 44]. In addition to the rib and strip waveguides, owing to the high refractive index nature of silicon platform, other novel types of waveguides which rely on different guiding mechanisms have been developed, such as slot waveguide, photonic crystal waveguide (PhCW) and SWG waveguide. In slot waveguide, which is formed by a low index (air/oxide) narrow slot region (few tens of nanometers) embedded between two rails of high index (silicon) waveguides, the overlap of the evanescent tail of the high intensity modes at the two interfaces of the slots leads to a greatly enhanced light field confinement in the low-index slot region [45, 46]. Since the light is tightly confined in the oxide/air slot region which has relatively less non-linearity compared to silicon, the slot waveguide features reduced non-linearity and facilitates chip-scale optical interconnects [47, 48, 49]. In addition to it, the slot region can be filled with an active material or analyte leading to the combination of a huge confinement and a high overlap of the optical field with the analyte making it a potential candidate for bio-sensing applications [50, 51, 52, 53]. In PhCW, on the other hand, the guiding mechanism is based on the photonic bandgap effect which was conceptually proposed by Yablonovitch and John

in 1987 [54, 55]. PhC possesses a periodic dielectric structure and the light is confined at the scale of optical wavelength in the channel waveguide surrounded with photonic-crystal region [56, 57, 58, 59]. Due to their promising features like ultra compact size, flexibility in design, high measurement sensitivity and suitability for monolithic integration, PhC based devices have been demonstrated for various applications like filters [60, 61, 62], sensors [63, 64, 65, 66], modulators [67, 68], delay-lines [69, 70, 71] etc. However, PhCW suffers from inherent polarisation and wavelength dependent losses. Sub-wavelength grating (SWG) waveguide is a new type of photonic waveguide that has attracted immense research interest in the recent past due to their low loss and flexibility in tailoring the effective refractive index of the guided mode. A comprehensive study on sub-wavelength gratings was first carried out by Rytov in 1956 where he proposed to treat the grating as a homogeneous waveguide [72]. This was followed by the detailed and comprehensive study of effective medium theory by Lallane [73, 74]. The use of sub-wavelength gratings for integrated optics was first proposed in 1992 [75]. However, they found widespread applications in photonic integrated circuits in silicon-on-insulator platform only in the 21^{st} century after the development of high-resolution lithography techniques [76]. A typical SWG waveguide consists of periodic arrangement of high and low refractive index material with pitch smaller than one wavelength. Waveguides with periodic perturbations behave differently in different frequency regions. Figure 1.7(b) shows the frequency (ω) vs. wave-vector (k) relationship of a 1-D uniform periodic grating formed by alternating layers of high refractive index n_1 and low refractive index n_2 materials.The gratings are considered to have finite width and device layer thickness. The black solid lines denote the allowed modes that are guided through the periodic waveguide. The propagating modes lie between two lines with slopes c/n_1 and c/n_2 which are called the lightlines. The phase velocity ($V_{ph} = c / n_{eff}$) of truly guided modes is always greater than c/n_1 and less than c/n_2. When the mode is fully confined, it approaches the c/n_1 lightline and when the mode is near the cut-off, it approaches the c/n_2 lightline where the wave is leaked to the outside cladding. Based on the ratio of the grating pitch Λ to the operating wavelength λ, the periodic grating can operate in three regions [77]:

Radiation region ($\Lambda > \lambda$), where the incoming beam scatters to different diffraction orders

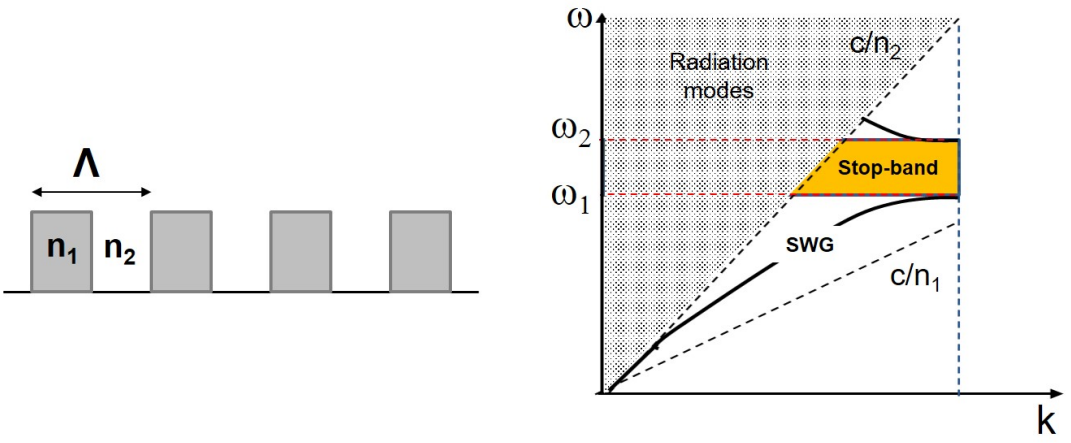

(a) (b)

Figure 1.7: (a) Cross-section schematic of a 1-D periodic grating formed by alternating layers of high refractive index n_1 and low refractive index n_2 materials. (b) Corresponding dispersion curve (ω - k relationship) with dashed lines representing the cladding light-lines and the solid lines representing the guided modes. The yellow region denotes the band-gap where there are no allowed solutions.

Reflection region ($\Lambda \approx \lambda$), where the incoming beam completely reflects back into the waveguide

Propagation region ($\Lambda << \lambda$) where the diffraction effects due to the periodicity is suppressed and the wave propagates like a normal waveguide mode. In this region, the grating structures can be approximated as homogeneous waveguides with equivalent refractive index calculated using effective refractive index theory proposed by Rytov in 1956 [72]:

$$n_{||} = \left[n_1^2.\delta + n_2^2.(1-\delta)\right]^{1/2} \tag{1.1}$$

$$\frac{1}{n_\perp} = \left[\frac{\delta}{n_1^2} + \frac{(1-\delta)}{n_2^2}\right]^{1/2} \tag{1.2}$$

where $n_{||}$ and $n_\perp$ denote the zeroth order approximation of the equivalent refractive index for the polarization along the x direction and z direction respectively. A brief description on effective medium theory is given in Appendix-B. In silicon platform, the SWG waveguide was first proposed and experimentally demonstrated by the National Research Council of Canada (NRC) in 2010 [78] by interleaving the high refractive index silicon material with low refractive index air. Figure 1.8(a) shows the SEM image

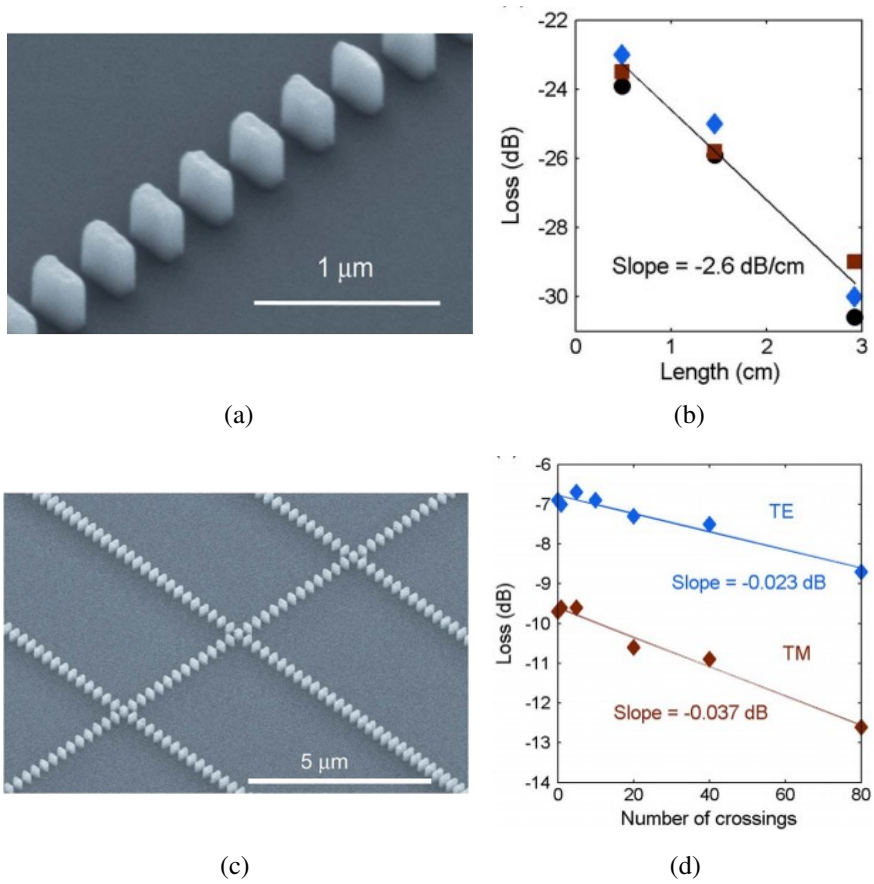

(a) (b)

(c) (d)

Figure 1.8: (a) SEM of a fabricated SWG waveguide with Λ = 300 nm, w = 250 nm and duty cycle = 0.33 and (b) measured transmission loss as a function of straight waveguide length for TE mode [78]; (c) SEM of SWG waveguide crossings and (d) measured transmission loss as a function of number of crossings [78, 79].

.

of their fabricated SWG waveguide with Λ = 300 nm, grating width W_g = 250 nm and grating duty cycle δ = 0.33. The measured length dependent waveguide propagation loss is shown in Figure 1.8(b) where the linear fit to the measurements yields a typical propagation loss of 2.6 dB/cm for the TE mode with negligible polarization dependent loss. The same group also demonstrated low loss waveguide crossings as shown as SEM image in Figure 1.8(c) [79]. This demonstration is particularly important in the current scenario since the feasibility to intersect waveguides with minimal cross-talk is a prerequisite for designing complex high density PIC. Till then, waveguide crossings mostly comprised of widened channels in the crossing region [80] and optimization of the shape of the wide channel in the crossing area [81]. In both the cases, the measured crossing losses were $\sim$ 0.2 dB and crosstalk of -40 dB or greater for TE polariza-

tion. However, when conventional waveguides are replaced by SWG waveguides in the crossing region, there is relatively smaller overlap of the delocalized SWG waveguide mode with the index perturbation caused by the intersecting waveguide. The loss per crossing was measured for a series of crossings as shown in Figure 1.8(d) and a linear fit resulted in 0.023 dB for TE and 0.037 dB for TM polarized mode with a crosstalk greater than -40 dB. These results were much superior to the previously demonstrated waveguide crossings. Since then, there due to their unique potential to engineer the propagation of light in planar waveguides, SWG waveguides had no turnback. Two key features that make them stand apart from their counterparts are their ultra-broadband operation and the feasibility for dispersion engineering. Most of the demonstrations using SWG waveguide primarily deal with improving the performance of the conventional passive silicon photonic devices like grating couplers [82, 83, 84, 85, 86, 87, 88, 89], mode converters [90, 91, 92], directional couplers [93, 94, 95, 96], ring resonators [97, 98, 99, 100, 101, 102, 103, 104], multimode interference couplers [105, 106, 107], beam splitters [108, 109] etc. which can be used to develop complex photonic integrated circuits. For example, directional couplers are mostly used in integrated optics as bus waveguides to ring resonators [110], optical switches [111], demultiplexers [112] etc. The main drawback of these devices are the inherent wavelength dependent coupling coefficient which hinders from getting a broadband response [113]. To obtain improved performance, often more complex and large footprint design solutions are proposed and demonstrated. By replacing the traditional strip waveguides with SWG waveguides, a compact broadband directional coupler was demonstrated [96]. Similarly, SWG based ring resonators are gaining attraction in the field of sensing because of its unique property to guide weekly confined modes with large mode field area, thereby enhancing mode-analyte interaction. While conventional ring resoantor bio-sensors reported sensitivity of $\sim$ 300 nm/RIU [50],the reported sensitivity of SWG rings have gone as high as 500 nm/RIU with minimum detection limit of $10^{-}7$ RIU. Recently, the birefringence of MMI coupler was engineered using SWG to demonstrate polarization beam splitters which had a compact device length of 100 μm [114]. In short, SWG waveguide is emerging as an important building block for developing components for many next generation silicon photonics applications specifically for optical communication and bio-sensing applications. Here we briefly review some important device designs that

have been demonstrated specifically in these areas.

1.1.1 Optical Interconnect Components/Devices

SWG waveguides in SOI platform are attracting strong research interest in the field of optical communication, specifically in realizing optical filters, delay lines and dispersion compensators. A majority of the filters implemented using SWG waveguide components are based on ring resonators [103, 97, 98] and Bragg gratings [103, 115, 116, 117] which operate for a narrow band of wavelengths. Figure 1.9(a) shows the

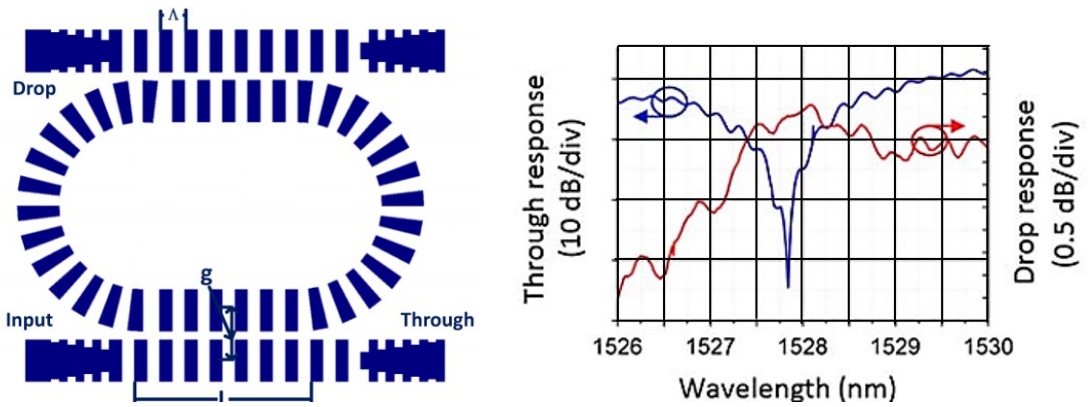

(a) (b)

Figure 1.9: (a) Schematic of SWG racetrack ring resonator and (b) measured through and drop port response [103].

schematic of SWG based racetrack ring resonator in add-drop configuration. The measured through and drop response at λ = 1527.85 nm are shown in Figure 1.9(b) with extinction ratio of 33 dB and 3 dB bandwidth of 1 nm. However, the maximum Q value and extinction ratio reported till now in SWG based ring resonators is only around 6000 and 35 dB, respectively. SWG based Bragg gratings have also been explored for narrow band filtering applications. Figure 1.10(a) shows the schematic of a conventional SWG waveguide and SWG based Bragg gratings. The Bragg grating is formed by interleaving two SWG waveguides with different duty cycles such that one is used to form the SWG waveguide and the second is set to operate in the Bragg regime. Figure 1.10(b) shows the transmission characteristics of the SWG waveguide and the SWG Bragg filter/reflector. The latter one has a dip at 1547 nm with a 3 dB stop-bandwidth of 0.5 nm due to Bragg reflection. As far as the wideband filters are concerned, few

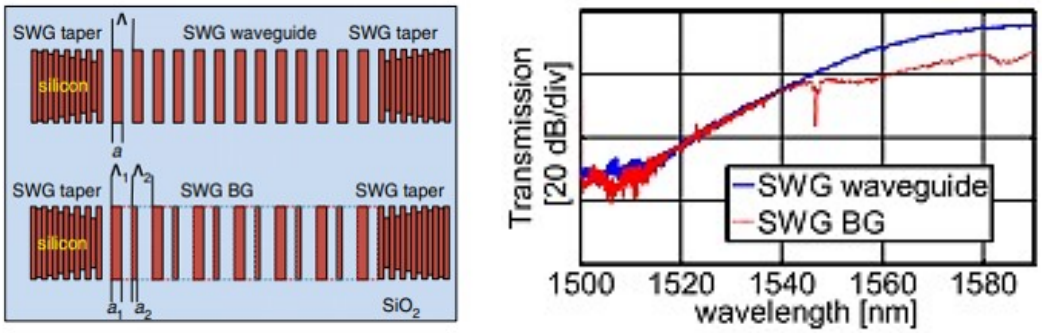

(a) (b)

Figure 1.10: (a) Schematic of the SWG based Bragg grating with interleaved SWG and SWG tapers, and (b) Spectral response of a SWG Bragg grating waveguide and a conventional SWG waveguide [103].

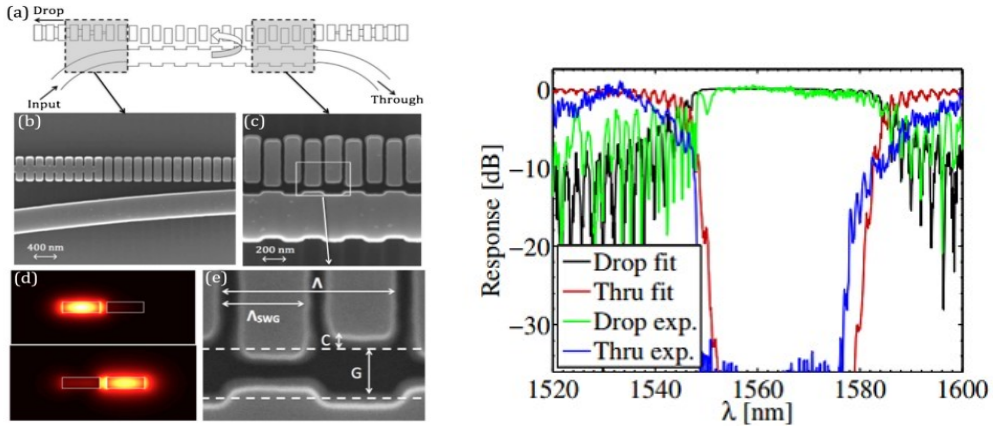

(a) (b)

Figure 1.11: (a) Schematic illustration of the SWG contra-directional coupler device with zoomed SEM images of the coupling region and (b) Simulated and experimental response of the broadband filter at the thru port and drop port. The measured filter bandwidth is around 33.4 nm [118].

studies have been carried out employing grating assisted contra-directional couplers [119, 120, 121, 118]. Figure 1.11(a) shows the SEM images of the fabricated broadband add-drop filter using sub-wavelength grating assisted contra-directional couplers. A 3-dB bandwidth of 33.4 nm is reported from experimental results (see Figure 1.11(b)). Its bandwidth and filter response can be tailored by suitably engineering the SWG waveguide parameters. However, it is very challenging to fabricate contra-directional couplers with the gratings spaced with close proximity to one another.

Recently, SWG waveguides have been used to demonstrate optical true time delay-line (OTTD) which is a basic building block for microwave photonic and optical pro-

cessing systems [116, 71]. An OTTD performs important functions like phase shift controlling, optical buffering, microwave filtering etc. to process broadband RF signals in microwave and radar systems. Optical delay lines are generally implemented in two ways to generate time delay between optical pulses: length variable delay line wherein the propagation length is varied and wavelength variable delay line wherein the propagation group velocity is varied. The dispersion engineering flexibility of SWG waveguide can be used to create group velocity variation for different wavelengths. Apart from that, SWG waveguides provide compact devices that support broader RF bandwidth. [116]. Figure 1.12(a) shows the schematic of a wavelength tunable time

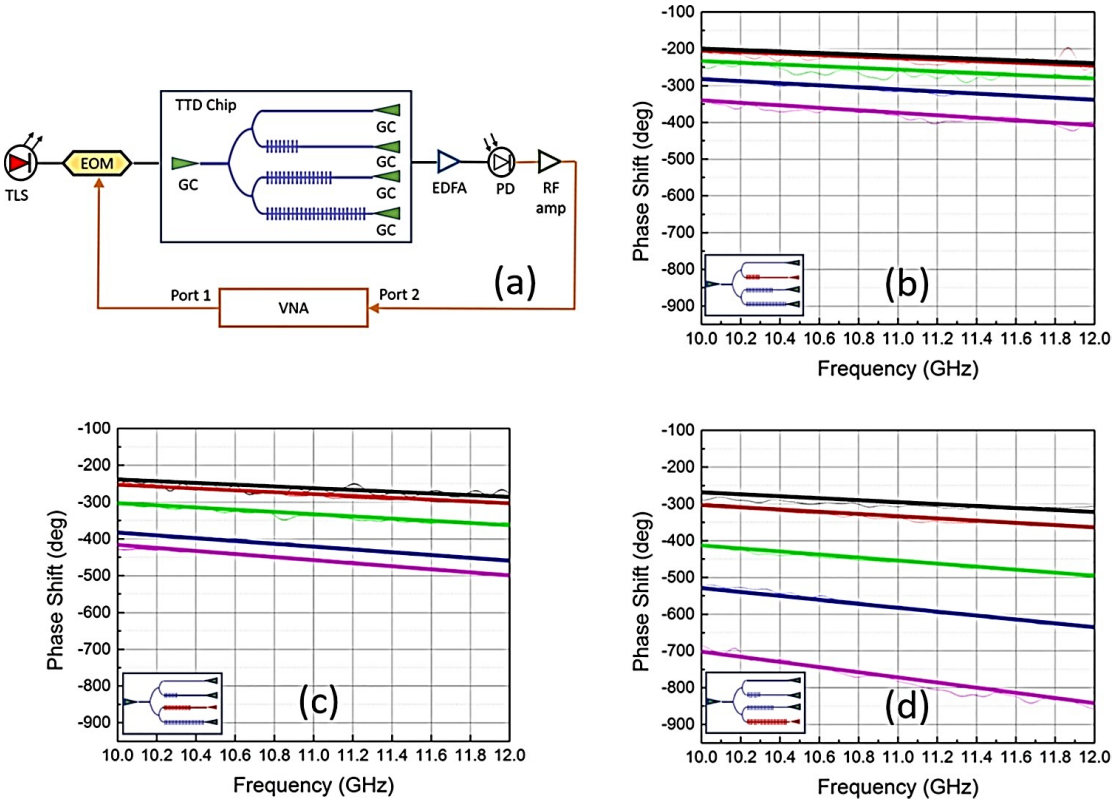

Figure 1.12: (a) Wavelength tunable OTTD measurement set up; Phase frequency curves for (b) Channel 2, (c) Channel 3 and (d) Channel 4 [71].

delay measurement setup which employs an on-chip 4 channel SWG waveguide with different lengths for achieving different delays. The corresponding phase frequency curves for each channel are shown in Figures 1.12(b)-(d). The time delays obtained for Channel-2 (2-mm silicon strip waveguide with 1-mm SWG), Channel-3 (1-mm silicon strip waveguide with 2mm SWG) and Channel-4 (3-mm SWG) are 94.43 ps, 115.63 ps, and 194.9 ps, respectively. Further delay can be achieved by just increasing the length

of the SWG waveguide region.

Thus there is a huge room for potential device demonstrations using SWG waveguides that allow for demonstrating complex systems that can provide increased functionality and performance in the field of RF/optical communication systems.

1.1.2 Sensing Devices

SWG waveguides are also emerging as potential candidates for sensing applications because of their unique ability to guide weekly confined modes with larger mode field area compared to conventional waveguides. This is possible due to the fact that the effective refractive index of SWG waveguides is much smaller compared to the conventional silicon wire waveguide. Figure 1.13(a) shows the 3D schematic of a SWG waveguide with top cladding comprising of a lower index material such as oxide, water or SU-8 [33]. Top-view and cross-sectional view of the electric field intensity distri-

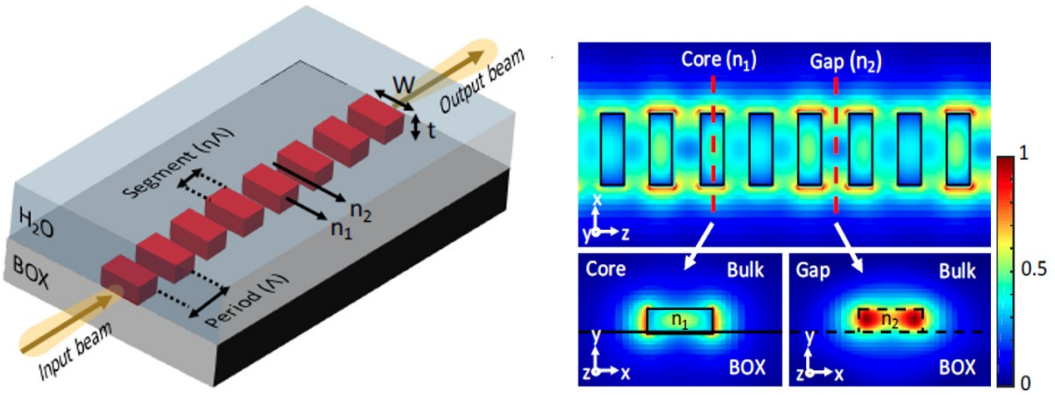

(a) (b)

Figure 1.13: (a) 3D scheme of SWG waveguide : W - waveguide width, t - device layer thickness, Λ - grating period, n_1 and n_2 - high and low refractive indices. (b) Top view and cross-sectional view of the electric field intensity distribution of an SWG waveguide [33].

bution in an SWG waveguide is shown in Figure 1.13(b). It can be observed that the optical mode for an SWG waveguide is mostly concentrated in the lower index regions which in turn enhances the cladding analyte and guided mode interactions. Thus, compared to conventional waveguide geometries (interacts only with evanescent fields), SWG waveguide based biosensors will exhibit superior sensing performance. The potential of SWG waveguides for bio-sensing applications was first explored by Perez et

al. in 2014 [122]. They employed full vectorial 3D FDTD simulations to analyze the sensing performance and achieved theoretical sensitivity values of 0.83 RIU/RIU and 1.5×10^{-3} RIU/nm for bulk and surface sensing, respectively. This was followed by a series of experimental demonstrations towards the development of SWG waveguide based various biosensors in SOI platform [97, 100, 101, 102, 98, 123]. Among these structures, SWG based integrated microring resonators are the most commonly used devices for sensing with reported sensitivity as high as 383 nm/RIU with water cladding and 270 nm with air cladding [97]. However, one major shortcoming was the relatively low Q-value of SWG based microring resonators ($\sim$ 6000), as mentioned earlier. Wang et al. tried to solve this issue by using trapezoidal silicon gratings which can reduce the bend induced loss by creating an asymmetric refractive index profile and thereby achieving a higher Q value of 11,500 [100]. By utilizing this trapezoidal SWG based MRR, a bulk sensitivity of 440.5 nm/RIU and a surface sensitivity of 1 nm/nm was reported [101]. Recently, SWG based multi-box waveguide biosensors have been developed by merging slot and SWG waveguide as shown in Figure 1.14(a) [123]. Low

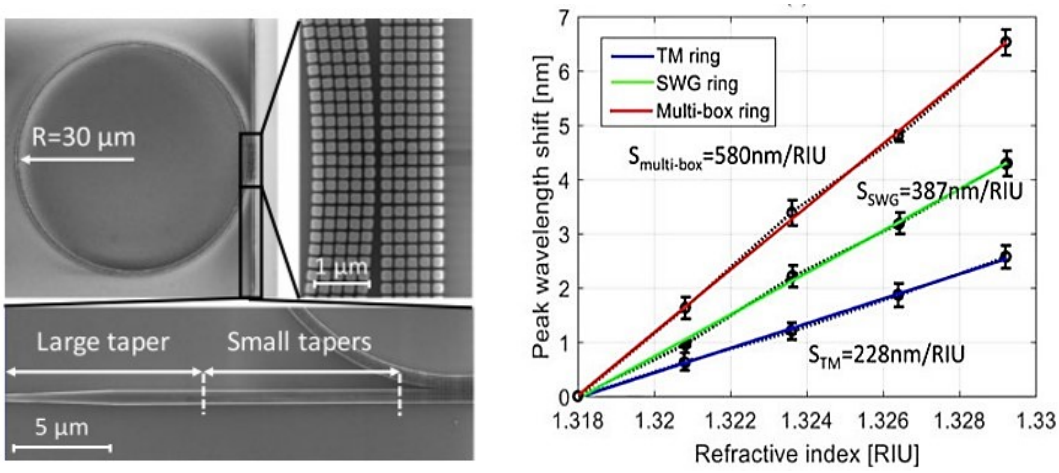

(a) (b)

Figure 1.14: (a) SEM image of a multi-box MRR; (b) Bulk sensitivities calculated for three resonators at 25 °C: the TM mode microring, conventional SWG microring and 5-row multi-box microring in the TE mode [123].

optical mode confinement is achieved by introducing gaps in between the silicon elements in the propagation as well as transverse direction thereby significantly reducing the effective refractive index of the confined mode. The multi-box structure facilitates more surface area for the analytes to attach to the silicon segments. This results in a bulk

sensitivity of 580 nm/RIU (Figure 1.14(b)) which is higher compared to conventional SWG waveguides (387 nm/RIU) and straight waveguides (228 nm/RIU).

Thus it is evident from the literature that a good number of SWG based devices have been already demonstrated in the past decade utilizing the flexibility offered by this technique of refractive index engineering in the silicon photonics platform. Their unique potential to control light propagation opens up a lot of research prospects to realize complex integrated circuits with increased performance or completely novel functionalities. For example, most of the SWG based filters demonstrated till date have limited spectral bandwidth and are suitable for narrow wavelength band add drop multiplexing. If SWG waveguides can be designed to function as broad wavelength band filter, it can be used to switch, route or duplex large band of optical signal in optical communication systems. For sensing applications, all the SWG based integrated photonic sensors reported so far are based on wavelength interrogation mechanism which requires expensive equipment like spectrum analyzers. Integrated Mach-Zehnder interferometer is a less expensive alternative for sensing via intensity dependent interrogation. However, MZI configuration needs to isolate the reference arm which adds to a critical lithography step. Also, enhanced sensitivity is obtained for large footprint usually in the order of millimeters. MZI structure integrated with SWG waveguides in its arms pose a promising and compact solution to realize highly sensitive refractive index sensors. Additionally, the reconfigurability aspect of SWG waveguide has not been explored till date. The flexibility in effective index tailoring of SWG waveguides and high thermo-optic coefficient of silicon ($\sim 1.8 \times 10^{-4} K^{-1}$ at λ = 1550 nm) can be combined to demonstrate highly efficient thermally tunable SWG waveguides. In an attempt to address the above issues, we set forth the research objectives for this PhD thesis as given in the next section.

1.2 Research Objective

The major objective of this thesis work was to explore and extend the prospects of integrated SWG waveguides in SOI focusing primarily on sensing and filtering applications. It was broadly aimed to come up with potential device demonstrations that

could address the pitfalls in the existing state of the art and specifically cater to the recent advancements in this field. The first objective was to study in detail the critical design parameters that are instrumental for the design of integrated SWG waveguides in SOI platform for various applications. Thereby, to optimize design parameters of SWG waveguides such that they could be adiabatically integrated with standard single-mode photonic wire access waveguides for novel silicon photonics device demonstrations (fabrication and characterizations) using CMOS compatible fabrication processes. Once the critical grating design parameters are identified for stand-alone SWG waveguides, our next objective was to design and experimentally demonstrate reconfigurable broadband and high extinction demultiplexers by integrating SWG waveguides into the arms of a Mach Zehnder interferometer (MZI). It was also planned to demonstrate on-chip broadband filters with linear and smooth edge roll-off which are useful for single side-band suppression in microwave photonics phase shifters. We also wanted to explore the possiblity of using SWG waveguide devices as a cost-effective refractive index sensor platform by utilizing their tailorable dispersion characteristics and their unique ability to guide weekly confined modes with larger mode field area. All the SWG waveguide devices were planned to demonstrate using SOI substrate with device layer thickness of 220 nm, buried oxide (BOX) layer thickness of 2 μm, and handle wafer thickness of 500 μm; which is commonly used in silicon photonics foundries. It was also kept in mind to design all the devices for broadband operation covering C+L bands (1500 nm-1620 nm); equipment/components needed for device characterizations are easily available.

1.3 Thesis Organization

The rest of this thesis is structured as following:

Chapter-2 deals with the design aspects of SWG gratings in 220-nm silicon-on-insulator platform. The working principle and theory of sub-wavelength gratings are presented first. This is followed by the rigorous simulation study of the critical parameters that are instrumental in designing of SWG waveguides in SOI platform. Finally, the integration aspects of SWG waveguide on SOI platform is studied by investigating optimal taper designs for integrating SWG waveguides with access silicon waveguides.

Chapter-3 discusses the design and demonstration of an ultra broadband add-drop filter/switch circuit by integrating a pair of SWG waveguides in a 2×2 Mach-Zehnder interferometer configuration. The SWG waveguide is designed to act as a C/L wavelength band filter. The device description and design principle of SWG waveguide are discussed in detail first. This is followed by the fabrication and experimental demonstration which include passive as well as thermo-optic detuning. The chapter is concluded by summarizing the figures of merit of the demonstrated device as a add-drop filter circuit/switch.

Chapter-4 is reserved for the design and demonstration of an integrated optical apodized SWG waveguide exhibiting high extinction edge-filter characteristics with linear roll-off in dB scale. The design aspects of the proposed device along with the critical parameters that decide the filter characteristics are discussed with the help of a semi-analytical model as well as simulations. The experimental demonstration and theoretical validation are presented.

Chapter-5 discusses the design and experimental demonstration of an integrated optical Mach-Zehnder interferometer comprised of a sensing arm of SWG waveguide and a reference waveguide arm insensitive to cladding refractive index change in silicon-on-insulator platform for lab-on-chip sensing applications. Wavelength interrogation as well as intensity interrogation aspects of the device are discussed in detail.

Chapter-6 marks the conclusion of the thesis with a brief summary of the research work carried out and discussions about possible future research directions.

CHAPTER 2

SWG Waveguide : Theory and Design

This chapter aims to carry out a general study of the design aspects along with the challenges involved in integrating a SWG waveguide with single-mode access waveguides. The discussions intend to serve as a reference for designing the SWG waveguides for specific applications in the succeeding chapters. Figure 2.1 shows the 3-D schematic illustration of a typical SWG waveguide integrated with input/output photonic wire waveguides via. adiabatic mode converters in SOI. A conventional photonic wire waveguide of same length is also shown alongside for reference. The access

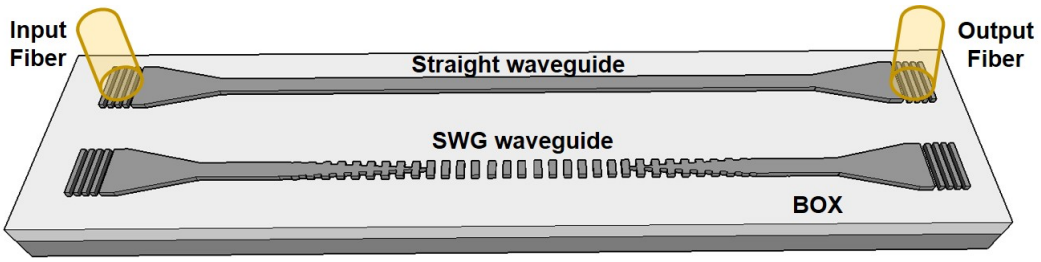

Figure 2.1: 3-D scheme of an integrated SWG waveguide along with a typical photonic wire waveguide in SOI; top cladding is assumed to be air. Vertical input/output grating couplers are used for device characterization through standard single-mode fiber interfacings. BOX - buried oxide

waveguide width W and the SWG waveguide width W_g are assumed to be identical and the waveguides are terminated on either sides with grating couplers (GC) for efficient coupling of light into and out of the devices via standard single-mode optical fibers operating at $\lambda \sim 1550$ nm. The design of an integrated SWG waveguide thus includes the design of SWG waveguide parameters along with adiabatic tapers, access photonic wire waveguides to ensure single mode guidance and grating couplers for efficient light coupling. The input/output single-mode photonic wire waveguides help to excite/filter fundamental mode into/out of the SWG waveguide efficiently. Thus one can be relaxed in SWG waveguide design for its single-mode guidance. An extensive study on the optimal design parameters for single mode silicon waveguides and GCs in SOI has already been carried out in our group [124, 125, 126]. The GC design has been

optimized to give broadband response in the wavelength range centering around $\lambda \sim$ 1550 nm with minimum back reflections [124]. Therefore, only a brief description on the working principle and optimized design parameters have been given in Appendix-A for completeness. The cross-section scheme of a generic SOI waveguide with design parameters (waveguide width W, device layer height H and slab-height h) is shown in Figure 2.2(a). As mentioned earlier, the access waveguide geometry is in general designed to be single mode guidance within given wavelength range of operation. However, the polarization of the guided mode is highly sensitive to waveguide dimensions. While the device layer thickness is fixed (H = 220 nm), W and h are the two parameters that can be varied to obtain single-mode guidance over a desired wavelength range ($\lambda \sim$ 1550 nm) for TE-like (dominant component of electric field along x-direction) and TM-like polarization (dominant component of electric field along y-direction). Figure

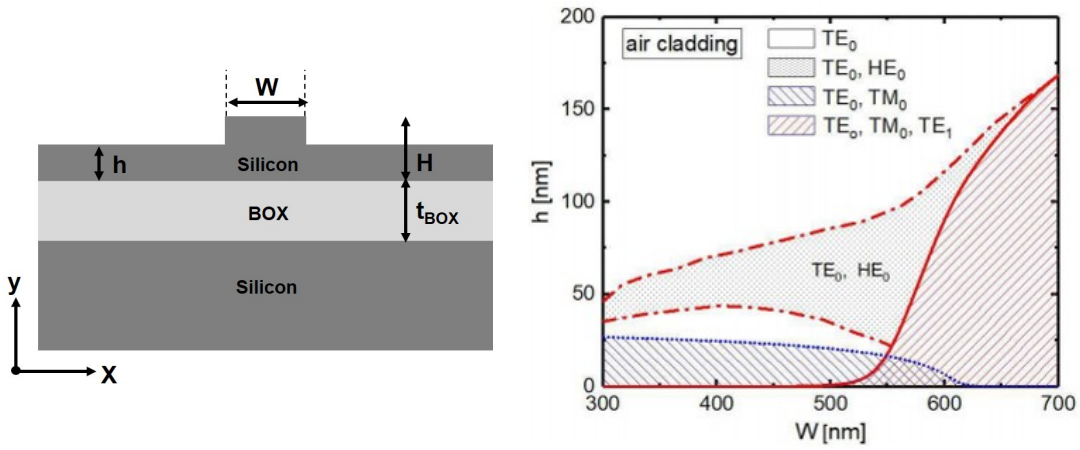

(a) (b)

Figure 2.2: (a) Generic scheme of a silicon waveguide cross-section in SOI platform (not to scale); the top cladding can be air/siO_2/Si_3N_4, etc. W: Waveguide width; h: slab layer thickness, H: device layer thickness, t_{BOX}: BOX layer thickness and (b) Allowed guided modes in W-h plane for H = 220 nm, t_{BOX} = 2 μm and λ = 1550 nm [126].

2.2(b) shows the supporting modes of a rib waveguide with air as top cladding calculated for waveguide width 300 nm $\leq W \leq$ 700 nm and slab height 0 nm $\leq h \leq$ 200 nm at an operating wavelength $\lambda \sim$ 1550 nm [126]. The number of guided modes and the polarization of the m^{th} order (m = 0,1,2..) guided modes are calculated using commercial 'Finite Difference Eigen mode solver (FDE)' of Lumerical MODE Solutions. We observe that for $W <$ 500 nm, the waveguide supports fundamental TE_0 mode for

any value of slab-height. However, as W increases beyond 500 nm, the slab-height cut-off value increases steadily for maintaining single mode condition. The look-up graph shown in Figure 2.2(b) has been used in the rest of the thesis to decide on the optimal waveguide dimensions to be considered for various applications. Only the SWG waveguide design is discussed here in details for its effective integration to realize functional integrated optical devices in the light of various silicon photonics applications.

In the following sections, the dispersion characteristics of an infinitely extended 1-D periodic layered structure are discussed followed by the detailed analysis of the critical parameters that are instrumental for the design of SWG waveguides in SOI platform. Finally, optimal design solutions for overcoming the challenge of integrating SWG waveguides with access photonic waveguides via. efficient mode-size converters is addressed.

2.1 Wave Propagation in Periodic Layered Media

As discussed in Chapter 1, sub-wavelength grating is a structure with periodic modulation of effective refractive index in one-dimension with the periodicity much small compared to the wavelength of lightwave to be propagated. The lightwave in this periodic structure can be described well using Bloch theorem which was developed similar to electron wave propagation in crystals [56]. Before discussing the numerical techniques used to design sub-wavelength grating waveguides with finite dimensions, we consider the case of a simple periodic structure with alternating layers of refractive indices n_1 and n_2 having thickness a and b respectively as shown in Figure 2.3. For simplicity, we assume the materials that constitute the periodic layers to be isotropic and non-magnetic. The refractive index profile of such a periodic medium is given by:

$$n_z = \begin{cases} n_2, & 0 < z < b \\ n_1, & b < z < \Lambda \end{cases} \tag{2.1}$$

where

$$n(z) = n(z + \Lambda) \tag{2.2}$$

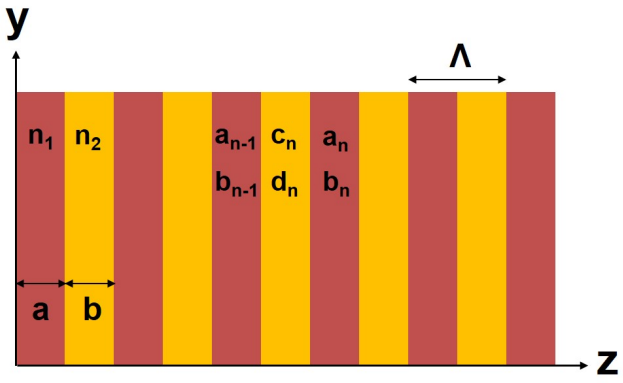

Figure 2.3: Schematic of a 1-D periodic layered media when lightwave propagates along the grating vector (z-axis); Λ: Grating period, n_1: high refractive index, n_2: low refractive index, a, b: thickness of layers having refractive indices n_1 and n_2.

and a and b are the thickness of the layers with refractive indices n_1 and n_2 respectively such that $a + b = \Lambda$. The z-axis is considered along the direction of periodicity.

Electric field vector of a wave propagating in such a periodic medium can be described using Bloch theorem which is given by

$$\mathbf{E} = \mathbf{E}_K(z)e^{-iKz}e^{i(\omega t - k_y y)} \tag{2.3}$$

where $\mathbf{E}_K(z)$ is a periodic function with period Λ, i.e.,

$$\mathbf{E}_K(z) = \mathbf{E}_K(z + \Lambda) \tag{2.4}$$

and k_y is the wavevector component along y-direction, ω is the angular frequency and and K is the Bloch wavenumber. The dispersion relationship between ω and K can be obtained by combining the Bloch wave theorem and transfer matrix method described in [127]. The analytical equations of dispersion relation for TE and TM polarization are given by

$$cosK\Lambda = \begin{cases} cos\ k_{1z}a\ cos\ k_{2z}b - \frac{1}{2}\left(\frac{k_{2z}}{k_{1z}} + \frac{k_{1z}}{k_{2z}}\right) sin\ k_{1z}a\ sin\ k_{2z}b, & (TE) \\ cos\ k_{1z}a\ cos\ k_{2z}b - \frac{1}{2}\left(\frac{n_2^2 k_{1z}}{n_1^2 k_{2z}} + \frac{n_1^2 k_{2z}}{n_2^2 k_{1z}}\right) sin\ k_{1z}a\ sin\ k_{2z}b, & (TM) \end{cases} \tag{2.5}$$

where

$$k_{1z} = \sqrt{\left(\frac{n_1\omega}{c}\right)^2 - k_y^2} \tag{2.6}$$

$$k_{2z} = \sqrt{\left(\frac{n_2\omega}{c}\right)^2 - k_y^2} \tag{2.7}$$

The range of frequencies for which $\left|\cos(K\Lambda)\right| < 1$ correspond to real value of K (propagating Bloch waves in the periodic structure) and $\left|\cos(K\Lambda)\right| > 1$ correspond to imaginary K (evanescent Bloch waves) which are called the photonic band gaps of the periodic medium. The photonic band-edges are regions where $\left|\cos(K\Lambda)\right| = 1$. The disper-

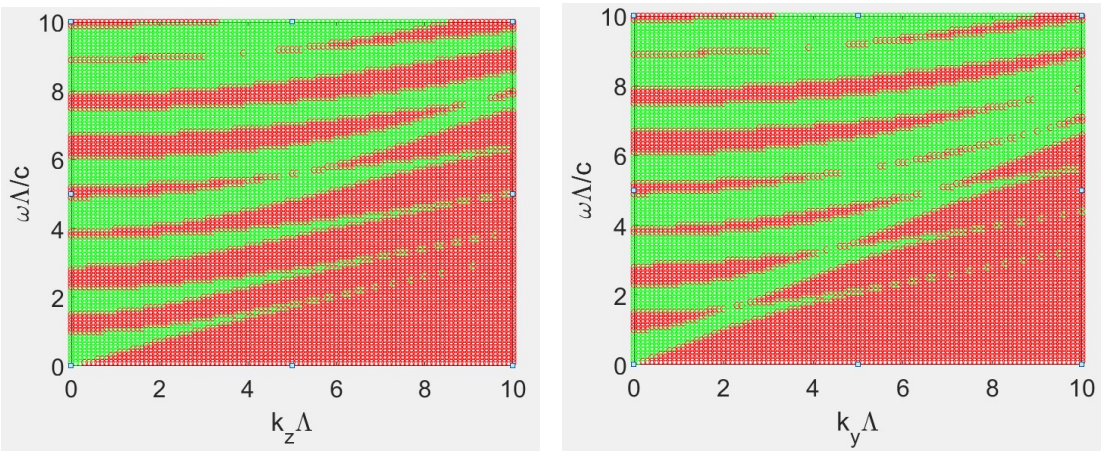

(a) (b)

Figure 2.4: Calculated photonic band structures for (a) TE and (b) TM waves propagating in a 1-D periodic medium. The blue colored zones are photonic bandgap regions and the green colored zones are allowed photonic bands; (n_1 = 3.477, n_2 = 1.45, λ_0 = 1.55 μm, $a = b$ = 0.15 μm).

sion curves calculated for TE and TM waves using Equation 2.5 are shown in Figure 2.4(a) and 2.4(b) respectively. We have considered n_1 = 3.477, n_2 = 1.45, λ_0 = 1.55 μm, $a = b$ = 0.15 μm for the calculations. The blue colored zones are the photonic bandgap regions where $\left|\cos(K\Lambda)\right| > 1$ and the green colored zones are the allowed photonic bands where $\left|\cos(K\Lambda)\right| < 1$. Thus we can conclude that the dispersion curve and hence the stop-band frequency range is different for TE and TM polarization. However, when the light is incident at normal angle, i.e. along the length of the grating, then k_y = 0 and we observe that the dispersion is polarization independent. The dispersion relation between ω and K can be then written as

$$cosK\Lambda = cos\ k_1 a\ cos\ k_2 b - \frac{1}{2}\left(\frac{n_2}{n_1} + \frac{n_1}{n_2}\right) sin\ k_1 a\ sin\ k_2 b \tag{2.8}$$

where $k_1 = (\omega/c)n_1$ and $k_2 = (\omega/c)n_2$. Figure 2.5 shows the dispersion relationship plotted for normal incidence considering n_1 = 1.45 and n_2 = 3.4777 using equation 2.8. The blue curves denote the real K values and the red curves denote imaginary K values.

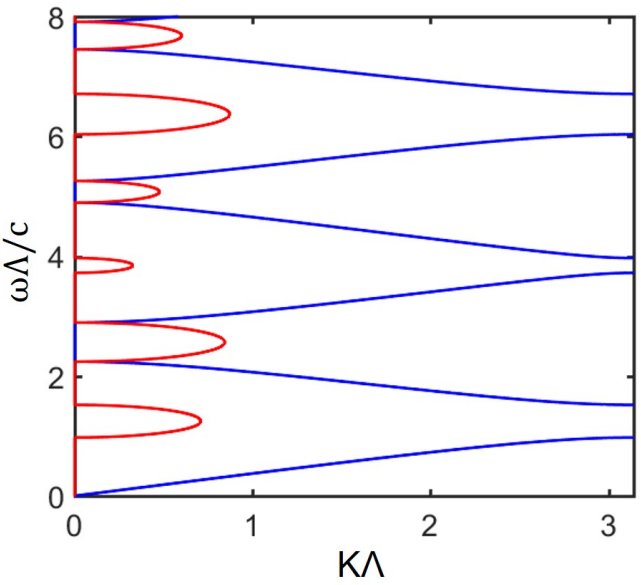

Figure 2.5: Dispersion relation of a 1-D periodic medium at normal incidence. The blue curves denote the allowed Bloch solutions and the red curves denote the evanescent Bloch wave solutions.

When K is real, the intensities of the Bloch wave will be a periodic function of position in the medium and propagate without loss (sub-wavelength range). Bloch wave becomes evanescent when the K values are imaginary. All the mathematical formulations developed for periodic layered structure holds for SWG waveguide as well except for the fact that the SWG waveguides have vertical as well as lateral mode confinement. For a periodic layered medium with uniform material properties, analytical solutions exists as discussed above, but not for the case of SWG waveguides which has index guided modes and hence numerical tools should be utilized.

In the next section, we will analyze the bandstructure properties and transmission characteristics of integrated SWG waveguides in SOI, which are confined to finite dimensions in all the three directions.

2.2 SWG Waveguide Design

In this section, we will discuss the design aspects of uniform sub-wavelength gratings in silicon waveguides. SWG is characteristically different from a conventional grating integrated along waveguide for distributed Bragg reflector (DBR). While DBR structures have weak periodic perturbations in the waveguide leading to narrow-band notch filter characteristics around Bragg wavelength, a typical SWG waveguide of finite width and height has relatively stronger refractive index modulation resulting into guided modes only above a cut-off wavelength. In this thesis, we focus on both the guided SWG pass-band as well as the Bragg reflection region. The cross-sectional schematic of a typical SWG structure in SOI is shown in Figure 2.6(a). The gratings are formed by alternating

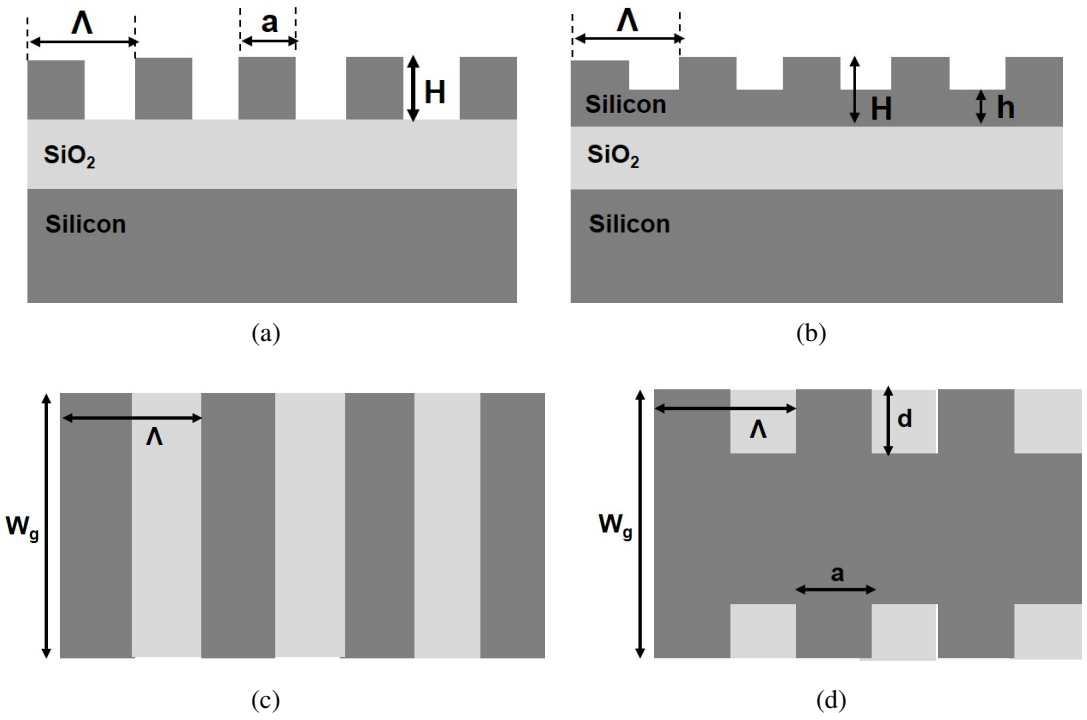

Figure 2.6: Cross-sectional and top-view schematic of a periodic grating structure in SOI (not to scale) for (a) h = 0 (b) $h \neq 0$ (c) $d = W_g/2$ and (d) $d < W_g/2$. Λ: Grating period, $\delta = a/\Lambda$: duty cycle W_g: Grating width, d: corrugation width, h: slab height, H: device layer thickness, t_{BOX}: BOX layer thickness

layers of high refractive index silicon ($n = 3.477$) and low refractive index cladding, air ($n = 1$) in this case. The duty cycle of this structure is defined as $\delta = a/\Lambda$, where Λ is the period of the grating. The grating thickness is defined by $H - h$ which can

be down till the BOX layer (h = 0 nm) as shown in Figure 2.6(a) or a smaller value retaining a finite value of slab region (h $\neq$ 0) as shown in Figure 2.6(b). A finite value of slab height is often advantageous for SWG waveguides as it aids in fabricating slab integrated microheaters which have relatively less thermal response time compared to oxide integrated microheaters. Figure 2.6(c) and 2.6(d) show the top-view schematic of two commonly used grating structures: ON-OFF grating with corrugation width d = W_g/2 and side-wall grating with $d < W_g$/2, respectively. The grating width is denoted by W_g.

We start the design by choosing W_g = 500 nm since a photonic waveguide of the same width satisfies the single-mode condition for an operating wavelength around λ = 1550 nm (see Figure 2.2(b)). For a simple DBR grating structure with weak perturbations, Couple Mode Theory (CMT) is sufficient to design the grating parameters [128]. The grating period can be estimated using the phase matching Bragg condition given by

$$\lambda_B = 2n_{eff}\Lambda \tag{2.9}$$

where λ_B is the phase matched Bragg wavelength and n_{eff} is the effective index of the fundamental guided TE mode for W = 500 nm which can be calculated using Lumerical MODE Solutions. The incoming light-wave is strongly reflected around the Bragg wavelength. The wavelengths that fall outside the Bragg region interfere destructively and hence are allowed to propagate in the grating. The peak reflectivity of DBR at λ_B and stop-band width around λ_B can be expressed as

$$R = tanh^2(\kappa L) \tag{2.10}$$

and

$$\Delta\lambda = \frac{\lambda_B^2}{n_{eff}L}\left\{1 + \left(\frac{\kappa L}{\pi}\right)^2\right\} \tag{2.11}$$

where κ is the backward coupling coefficient of the guided fundamental mode. For a rectangular grating modulation, κ is expressed as

$$\kappa = \frac{n_{Si}^2 - n_{air}^2}{n_{eff}}\left(\frac{2}{\lambda}\right)\int_{x_1}^{x_2}\int_{y_1}^{y_2}|\mathcal{E}(x,y,z,\lambda)|^2 dxdy \tag{2.12}$$

where $x_1 = W_g - d$; $x_2 = W_g$; $y_1 = h$; $y_2 = H$; $\mathcal{E}(x, y, z, \lambda)$ is the normalized transverse field distribution of the mode and the integration limits denote the waveguide rib height and modulation depth. κ can be improved by engineering the effective refractive index contrast or the width of the grating. Thus the peak reflectivity at λ_B depends on coupling coefficient, κ and length of the grating L, whereas the stop-bandwidth of the reflected mode at λ_B depends primarily on κ. The stop-band edge of the grating waveguide, λ_{edge}, which demarcates the sub-wavelength transmission regime and the reflection regime can be approximated as

$$\lambda_{edge} \sim \lambda_B + \frac{\Delta\lambda}{2} \tag{2.13}$$

Thus we observe that engineering the effective refractive index n_{eff} of the guided mode has significant impact on the deciding the Bragg wavelength, reflectivity and bandwidth of the grating structure. n_{eff} in turn depends on various geometrical parameters such as corrugation width, grating width and etch depth, duty cycle etc.

However, one thing to be noted here is that the CMT holds true only for weak grating perturbations [129]. In the cases of SWG waveguides, where the gratings operate in a strong coupling regime, they no longer satisfy the slowly varying envelope approximation used in CMT. As a result, the analytic expressions of CMT which are derived for weak coupling regime will not be valid for SWG waveguides. Thus although CMT can be used to gain intuitive insights about the influence of each grating parameter on the SWG waveguide response, we need to perform rigorous numerical simulations to precisely study their characteristics. In the following sections, we will discuss the effect of variations in these design parameters that are instrumental in deciding the transfer function of a uniform grating structure using Lumerical 3D-FDTD Solver.

2.2.1 Grating Period (Λ) and Duty Cycle (δ)

As given in Equation 2.9, the centre stop-band wavelength of the grating shifts towards longer wavelengths with increase in either the grating period Λ or the duty-cycle δ. In this sub-section, we investigate on the band-structure diagrams and transmission responses of the SWG waveguides, both for TE and TM polarized modes, calculated as

a function of Λ and δ to study the range of wavelengths for which the grating acts as SWG waveguide. The simulations are carried out by using Lumerical 3D-FDTD simulator tool. For band-structure calculations, a single unit cell of the grating is considered.

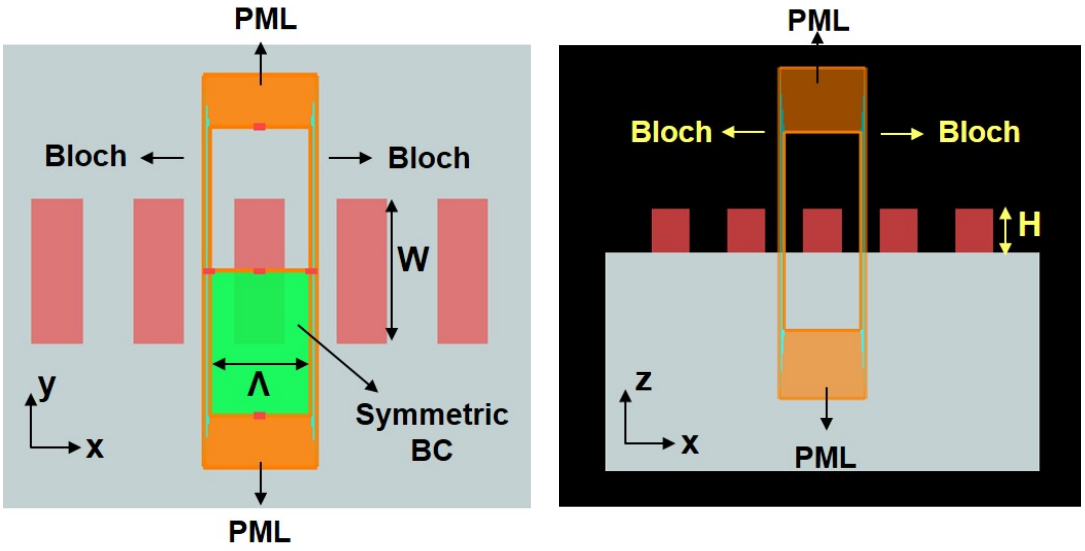

(a) (b)

Figure 2.7: (a) Top-view and (b) cross-sectional view of the unit cell of sub-wavelength grating structure (red-silicon, grey-oxide, black-air) with suitable boundary conditions used for band structure calculation in Lumerical FDTD simulation. Bloch boundary condition is used along x-direction (direction of periodicity) and PML boundary condition is used along y- and z- directions

The top-view and the cross-sectional view of the simulation set-up is shown in Figure 2.7(a) and 2.7(b) respectively. Bloch boundary condition is used in the direction of periodicity (x-direction in this case) while symmetry boundary condition is used through the middle of the grating and PML boundary condition is used in y- and z-directions. The size of the simulation window is kept x$\times$y$\times$z = $\Lambda \times 2\ \mu$m $\times 2\ \mu$m and the mesh resolution used is 20 nm $\times$ 20 nm $\times$ 20 nm. Periodic plane wave source is used to excite TE/TM polarized modes. A bandstructure analysis group that consists of randomly placed time monitors collect the field distribution over time. Most of the fields decay quickly due to destructive interference and the allowed modes of the structure continue to propagate indefinitely. The resonance frequencies are obtained from summation of Fourier transforms of the time domain fields from multiple monitors. The bandstructure plot is obtained by plotting the resonant frequencies for Bloch wave-vectors k ranging from $0.25*\frac{2\pi}{\Lambda}$ to $\frac{\pi}{\Lambda}$. Figure 2.8(a) and 2.8(b) show the band-structures calculated for TE

and TM polarized modes respectively, assuming Λ = 300 nm, W_g = 500 nm, δ = 0.5 and h = 0 nm. The x-axis is the normalized Bloch wave-vector $\frac{k\Lambda}{2\pi}$ and y-axis is the fre-

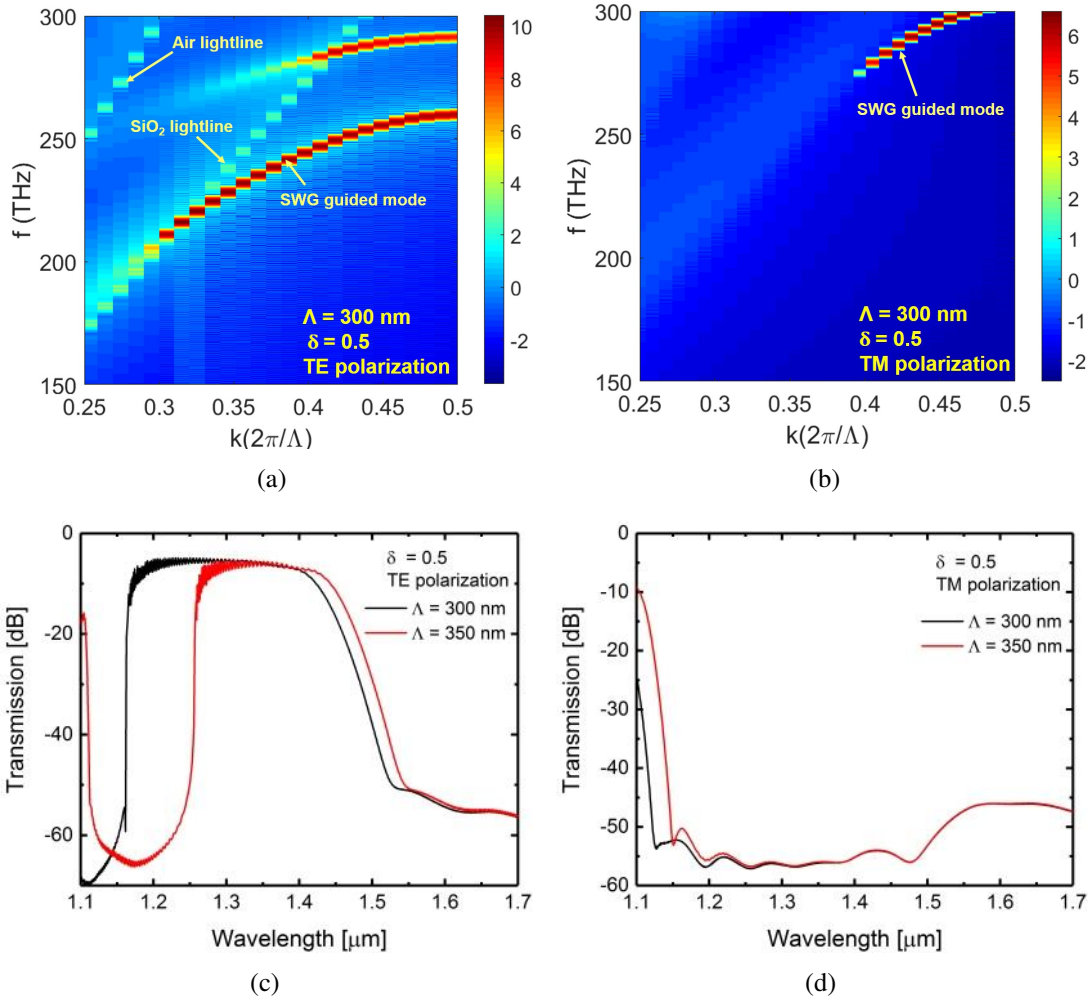

Figure 2.8: Band-structure diagrams of SWG waveguide calculated for (a) TE polarization and (b) TM polarization on 220 nm SOI platform with air and SiO_2 as top and bottom cladding respectively. Calculations are carried out using Lumerical 3D-FDTD for period Λ = 300 nm, grating width W_g = 500 nm; slab-height h = 0 nm and duty-cycle δ = 0.5; (c) and (d) Corresponding transmission responses of the SWG waveguides as a function of Λ calculated using Lumerical 3D-FDTD.

quency in THz. The dashed lines in the band-structure calculations are the dispersion curves of the air and oxide cladding which are called the air light-line and the oxide light-line respectively. Modes with frequencies that fall above the light-line will radiate its energy to the respective cladding, as discussed in Chapter-1. Thus a mode is said to be truly guided only when it is below the lowest light-line, oxide light-line in this case. The SWG guided mode is marked for both TE and TM cases in the dispersion diagrams

given in the Figures 2.8(a) and 2.8(b). The corresponding wavelength dependent transmission characteristics calculated as a function of Λ using Lumerical 3-D FDTD solver are shown in Figure 2.8(c) for TE polarization and 2.8(d) for TM polarization. From the band diagrams and the transmission responses, we observe that for the given set of grating parameters, the SWG waveguide does not support TM-polarized mode in the entire wavelength band. Even though the SWG waveguide supports TE polarized mode,

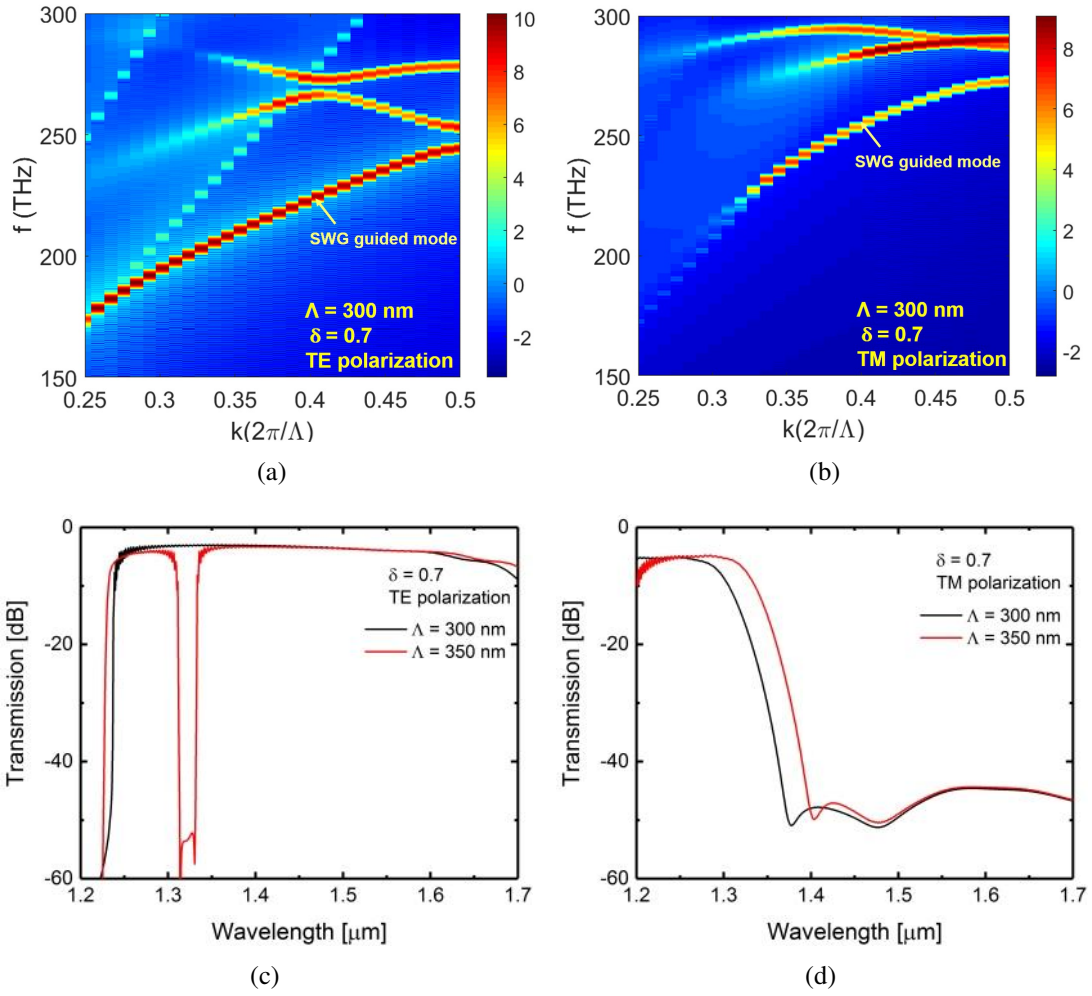

Figure 2.9: Band-structure diagrams of SWG waveguide calculated for (a) TE polarization and (b) TM polarization on 220 nm SOI platform with air and SiO_2 as top and bottom cladding respectively. Calculations are carried out using Lumerical 3D-FDTD for period Λ = 300 nm, grating width W_g = 500 nm; slab-height h = 0 nm and duty-cycle δ = 0.7; (c) and (d) Corresponding transmission responses of the SWG waveguides as a function of Λ calculated using Lumerical 3D-FDTD.

it can be observed that around λ = 1550 nm, the waveguide mode is a leaky mode and is no longer supported in the waveguide. Upon increasing Λ from 300 nm to 350 nm,

the left band-edge of the TE polarized SWG guided mode shifted to longer wavelengths by $\sim$ 100 nm in the transmission spectra as predicted from Equation. 2.9. However, there is no much change in the cut-off wavelength (right-side of the band) with increase in the grating period. Next, we increased the duty-cycle δ from 0.5 to 0.7 and calculated the corresponding band-structure and transmission responses as shown in Figure 2.9. All the other parameters were kept unchanged. It is interesting to note that when δ is increased to 0.7, TE polarized SWG guided mode is very well supported for wavelengths $\lambda \geq 1.23$ μm. When Λ is increased to 350 nm, the band-edge shifts towards longer wavelength ($\sim$ 100 nm) resulting in a narrow-stop band ($\Delta\lambda \sim 22$ nm) around $\lambda \sim 1.33$ μm. In this case also, we observe that there is no TM polarized SWG mode guidance around $\lambda \sim 1550$ nm. Thus we observe that the transmission band-edge shifts towards longer wavelengths with increase in the grating period or duty-cycle. This is more evident from Figure 2.10(a) which shows the transmission response of the SWG waveguide as a function of duty-cycle by keeping other parameters same. We also see that the stop-band width $\Delta\lambda$ decreases steadily with increase in δ as shown in Figure 2.10(b). This is because, for a rectangular grating teeth, the coupling strength κ after inserting the Fourier coefficient leads to [130, 127]

$$\kappa = \frac{n_{Si}^2 - n_{air}^2}{n_{eff}\lambda} sin(\pi\delta) \frac{\int\int_{corr.} |\mathcal{E}(x,y,z,\lambda)|^2 dxdy}{\int\int |\mathcal{E}(x,y,z,\lambda)|^2 dxdy} \tag{2.14}$$

Thus the influence of the duty cycle δ on the coupling coefficient κ is decided by the term sin($\pi\delta$) in Eq.(2.14), according to which κ will be maximum when δ = 0.5 and decreases with increase in δ from 0.5 to 1 as the gratings begin to disappear. The decrease in κ will in turn result in the shrinking of $\Delta\lambda$ as given in Eq. 2.11. and as shown in Figure 2.10(b).

For the rest of the chapter, we will be considering only TE polarized SWG guided mode considering the grating parameters Λ = 300 nm and δ = 0.7 since it supports TE mode around $\lambda \sim 1550$ nm.

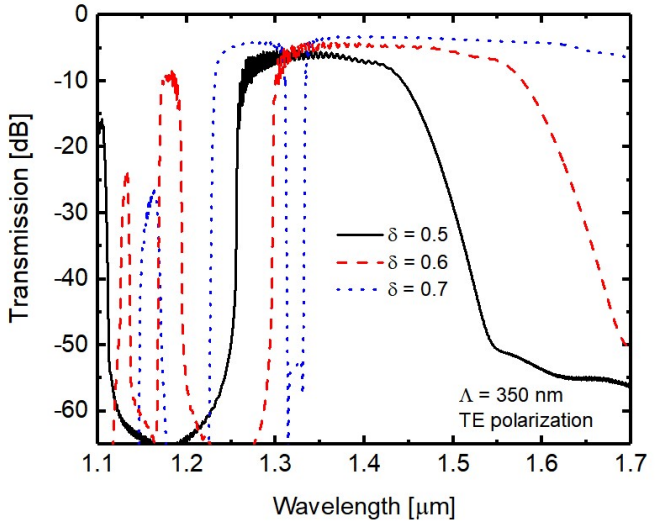

(a)

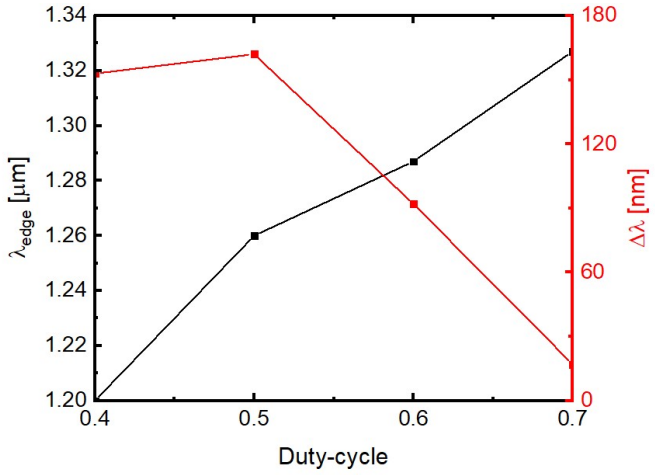

(b)

Figure 2.10: (a) Transmission responses of the SWG waveguides as a function of δ for TE polarization on 220 nm SOI platform with air and SiO_2 as top and bottom cladding respectively and (b) λ_edge and $\Delta\lambda$ dependence on duty-cycle. Calculations are carried out using Lumerical 3D-FDTD for period Λ = 350 nm, grating width W_g = 500 nm; slab-height h = 0 nm.

2.2.2 Corrugation width (d)

The next parameter to be considered is the corrugation width d which determines the coupling constant of the grating and thereby the bandwidth as given in Equation 2.11. The value of d can vary from 0 (no modulation) to $W_g/2$ (fully on-off grating) (see Figure 2.6(d)). Assuming Λ = 300 nm, W_g = 500 nm, and δ = 0.7, the impact of corrugation width on center Bragg wavelength and bandwidth is illustrated in Figure 2.11(a) and 2.11(b) respectively. It is calculated using Lumerical 3-D FDTD simulation of a

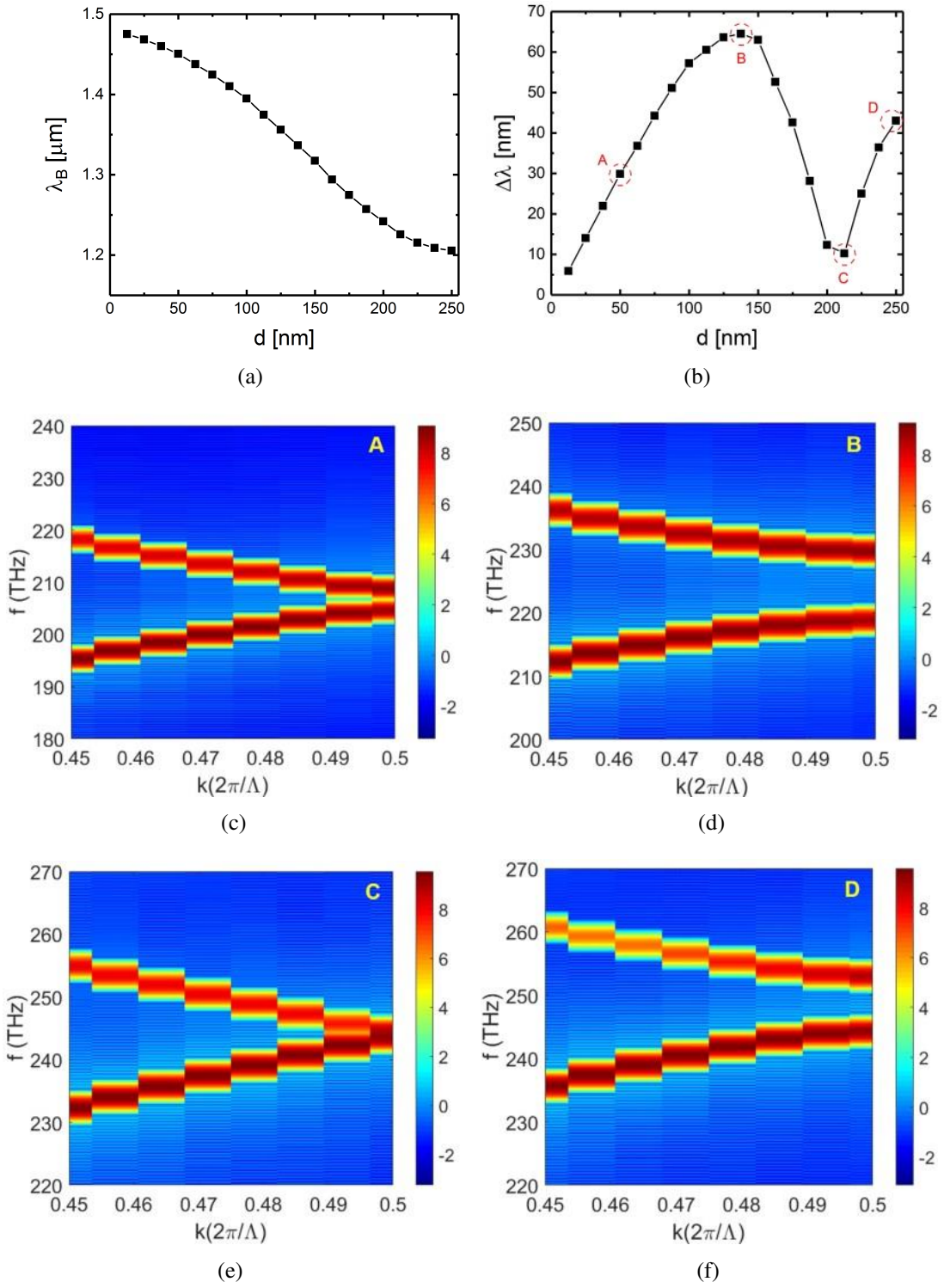

Figure 2.11: The dependence of (a) λ_B and (b) $\Delta\lambda$ of 1-D periodic gratings on sidewall corrugation considering Λ = 300 nm; W_g = 500 nm; h = 0 nm and δ = 0.7 on 220 nm SOI platform with air and SiO_2 as top and bottom cladding respectively. (c)-(f) are the corresponding bandstructure diagrams calculated for 4 different points: A (d = 50 nm), B (d = 135 nm), C (d = 200 nm) and D (d = 250 nm).

single grating unit cell of an infinitely periodic device as discussed in the previous section. In this simulation, we are interested in the band-structure relationship towards the stop-band edge, i.e. at wave vector $k = \frac{\pi}{\Lambda}$ which gives us the location of center Bragg wavelength and the size of the bandgap. As shown in Figure 2.11(a), the center Bragg wavelength shifts towards shorter wavelengths with increase in modulation depth which is a consequence of reduction in effective index as given in Equation 2.9. However, if we observe the behaviour of stop-band width, $\Delta\lambda$ as a function of d in Figure 2.11(b), it can be seen that the $\Delta\lambda$ initially increases with increase in d up-to a point 'B' and beyond that, the gratings exhibit an unusual reduction in band-width over a certain range of dimensions. According to couple mode theory, with increase in d, the coupling constant κ increases which in turn results in the increase of $\Delta\lambda$ as per Equation 2.11. This intriguing phenomenon is depicted more clearly in Figures 2.11(c) - 2.11(f) where the bandstructure diagrams are plotted at 4 different points in Figure 2.11(b). We see that, initially as d increases, $\Delta\lambda$ increases (points A and B) and reaches a maximum at point B (d = 135 nm). Beyond that, $\Delta\lambda$ begins to shrink and reaches a minimum value at point C (d = 220 nm). On further increasing the corrugation width, the stop-band width continues to increase again as shown as point D (d = 250 nm). In [131], Gnan $et\ al.$ developed an in-depth theoretical analysis of this phenomenon and came up with a model that could explain the reason for this bandgap closure. The "stop-band disappearance" could be attributed to the combined occurrence of Bragg reflection and Brewster angle. In other words, when the field which satisfies the Bragg reflection condition is incident at the planar discontinuities at the Brewster angle, their reflectivity gets cancelled out in spite of the strong refractive index contrast. This effect could be suitably used to design integrated optical sensing devices.

2.2.3 Grating etch depth ($H - h$)

Grating etch depth plays a crucial role in deciding the transmission response characteristics like center Bragg wavelength, stop-bandwidth etc. Increasing the grating etch depth means decreasing the slab height thickness, h. We first studied the impact of slab height thickness on the dispersion relation of the SWG waveguide. Figures 2.12(a) and 2.12(b) show the bandstructure calculations of a grating unit cell (Λ = 300 nm, δ = 0.7

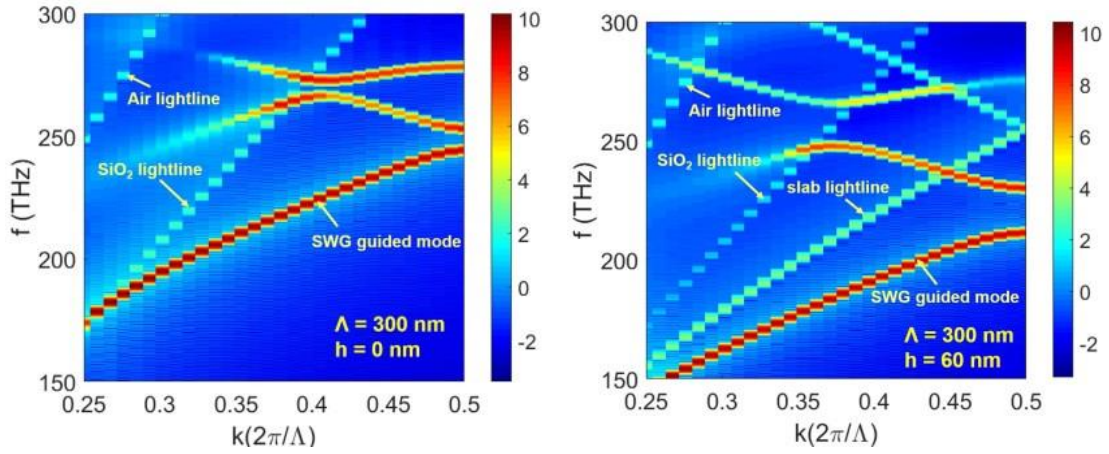

(a) (b)

Figure 2.12: Band-structure diagrams calculated for sub-wavelength gratings with slab-height (a) h = 0 nm and (b) h = 60 nm on 220 nm SOI platform with air and SiO_2 as top and bottom cladding respectively. Calculations are carried out using Lumerical 3-D FDTD for grating width W = 500 nm; grating period Λ = 300 nm and duty-cycle δ = 0.7.

and H = 220 nm) with slab-height h = 0 nm (as shown in Figure 2.6(a)) and 60 nm (as shown in Figure 2.6(b)) respectively. First thing to notice here is that when the slab-height is increased, an additional light-line comes into picture (shown in Figure 2.12(b)) apart from the air and the oxide light-line. This lightline indicates that the frequencies of the mode lying above this light-line will be leaked to the slab as slab modes and will become lossy. Also, we observe that the allowed mode gets lowered in frequency with increase in slab-height. This is expected since the effective refractive index of the mode is increased now as a fraction of mode is now propagating through the slab region. Figure 2.13 shows the transmission spectra calculated for the SWG waveguide h = 0 nm, 30 nm and 60 nm keeping all the other parameters same. It can be observed that with increase in the value of h from 0 nm to 60 nm, there is a huge red shift of 180 nm in the first order band-edge λ_{edge} and a broad stop-band ($\Delta\lambda \sim$ 120 nm) is formed around λ_B = 1.35 μm. This is due to the significant increase in the effective index value (Equation 2.9 and Equation 2.13). Since there is an additional slab region for the guided mode to propagate, we observe that the SWG mode has significantly lesser insertion loss (IL $\sim$ 1.5 dB) compared to the fully etched case (IL $\sim$ 5 dB).

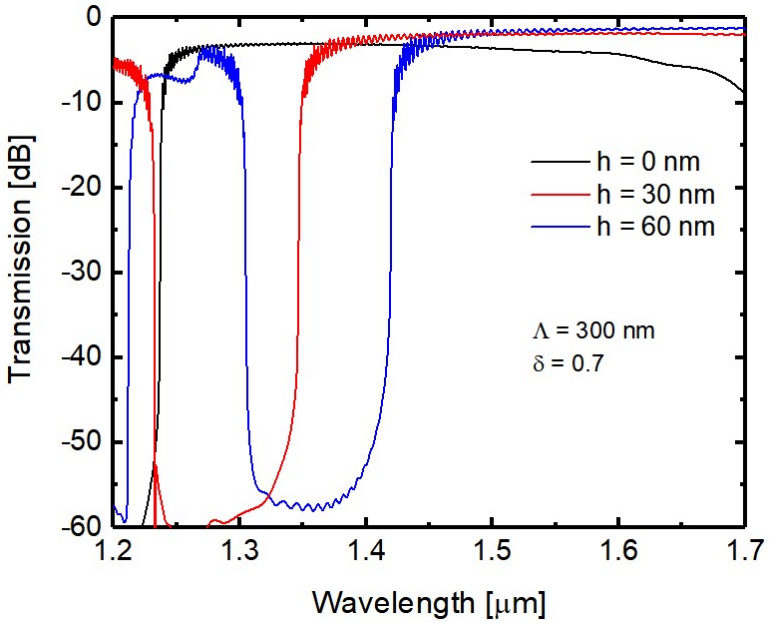

Figure 2.13: Transmission characteristics of the SWG waveguide calculated for h = 0 nm, h = 30 nm
and h = 60 nm. Calculations are done using Lumerical 3D-FDTD assuming Λ = 300 nm, δ = 0.7 and W_g = 500 nm on a 220 nm SOI platform with air and oxide as top and bottom cladding respectively.

2.2.4 Grating width (W_g)

In order to analyze the effect of width variation in grating response, we chose a uniform grating waveguide with Λ = 300 nm, δ = 0.7, h = 0 nm and H = 220 nm and used Lumerical 3D-FDTD to simulate the transmission response for grating width W_g = 500 nm, 600 nm, 700 nm and 800 nm as shown in Figure 2.14(a).

The access waveguide width was designed to be 500 nm to ensure single mode TE guidance and no taper was used in the waveguide-grating interface region. From Figure 2.14(a), it can be observed that the transmission band-edge shifts towards longer wavelength with increase in grating width. This is expected since the effective refractive index of the guided mode increases with increase in waveguide width. Also, the red shift in wavelength slows down for larger values of grating width since the n_{eff} increase is initially large and saturates gradually for larger values of W_g, as shown in Figure 2.14(b). Another thing to note in Figure 2.14(b) is that the stop bandwidth also increases with increase in grating width. This is due to the fact that increase in W_g leads to increased optical confinement in the grating region and hence the average refractive

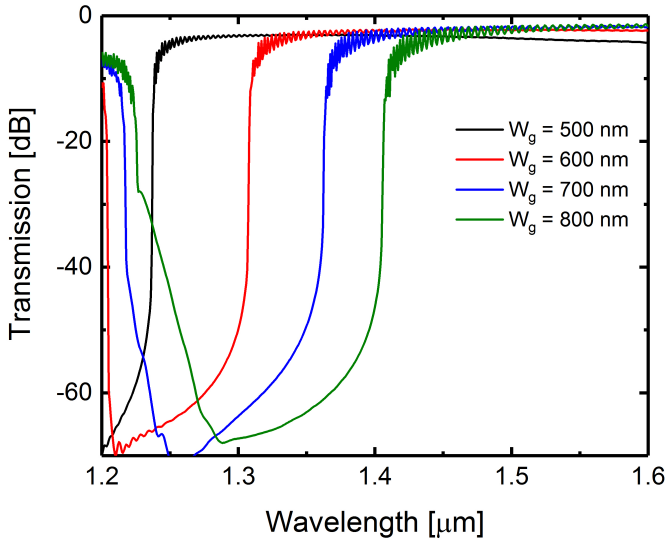

(a)

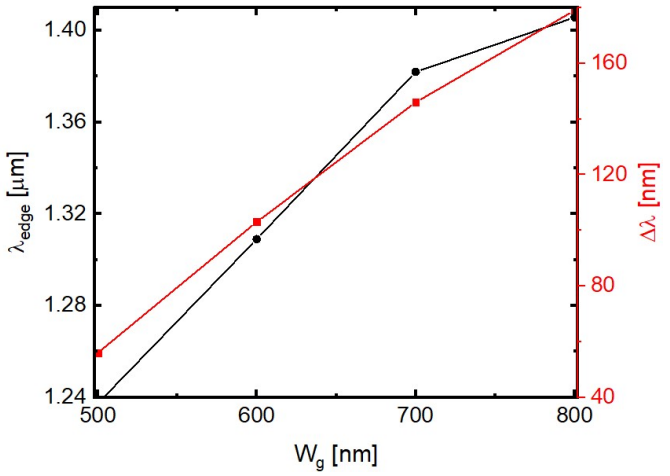

(b)

Figure 2.14: (a) Wavelength dependent transmission response of a uniform SWG waveguide as a function of grating width and (b) λ_{edge} and $\Delta\lambda$ dependence on W_g. Calculations are done using Lumerical 3D-FDTD assuming Λ = 300 nm, δ = 0.7 and h = 0 nm on a 220 nm SOI platform with air and oxide as top and bottom cladding respectively.

index seen by the optical mode in the grating region increases. This leads to increase in κ and thereby increase in $\Delta\lambda$ (as per Eq.2.11 and Eq.2.12). There is significant mode-mismatch loss ($\sim$ 5 dB) as well as ripples in the transmitted wavelength band due to abrupt transition between the access waveguide and the SWG waveguide. This can be taken care by designing suitable spot-size converters that provide adiabatic and smooth transition of the guided mode as discussed in the next section.

2.3 Taper design

Widespread use of SWG waveguides in integrated optics is possible only with efficient tapers that ensure smooth and adiabatic transition of guided mode from the access waveguide to SWG waveguide and vice-versa. This is because the guided mode in the input/output waveguide is significantly different compared to that of the Floquet- Bloch mode in the SWG waveguide. As such, cascading them without any intermediate taper will result in significant mode-mismatch loss. Designing of efficient SWG tapers is however challenging and not straight-forward as the taper design itself can result in local Bragg reflection zones thus resulting in back-reflections. To minimize these back-reflections due to the intermediate taper, the design must ensure an adiabatic transition, while at the same time avoiding the Bragg regime at any point of the taper. All the wavelength dependent transmission response studies carried out in this chapter till now were without any intermediate tapers. Now for designing efficient tapers/spot-size

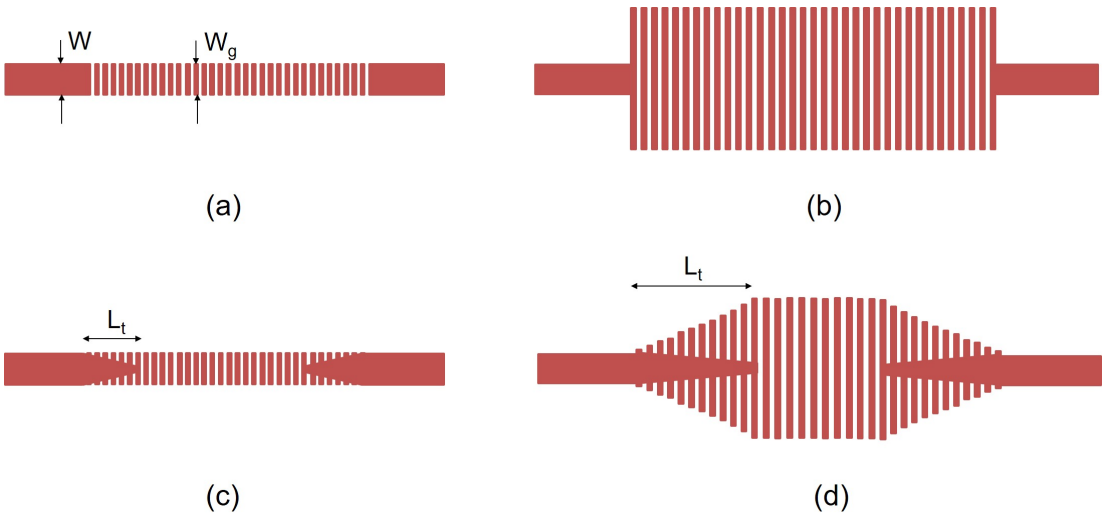

Figure 2.15: Schematic illustration of abrupt interface at the SWG-access waveguide interfaces when (a) $W_g = W$; (b) $W_g > W$; and (c) and (d) the corresponding taper profiles.

converters, we consider two possible scenarios: (i) when the access waveguide and the SWG waveguide are of the same width ($W_g = W$), as shown in Figure 2.15(a) and (ii) when the grating width is larger than the access waveguide width ($W_g > W$), shown in Figure 2.15(b). In case (i), the abrupt transition can be circumvented by using a taper profile wherein the width of the access waveguide decreases towards the center and vice-versa as shown in Figure 2.15(c). This kind of taper acts as silicon bridge elements

inserted between the gratings, so that the effective refractive index is adiabatically converted from waveguide mode to match SWG mode and vice-versa. However, the period of the gratings in the taper region, Λ_t should be carefully chosen so that the taper does not add to any additional Bragg reflection zones. Figure 2.16 shows the wavelength dependent transmission response of the SWG waveguide with $W_g = W$, calculated for three different taper grating periods, Λ_t = 300 nm, 250 nm and 200 nm and L_t = 30 μm. The taper width at the SWG end has been kept W_g = 100 nm keeping in mind the lithographic limitations. The transmission charcateristics of SWG waveguide without any input-output taper has also been included (dashed line) for comparison. As expected,

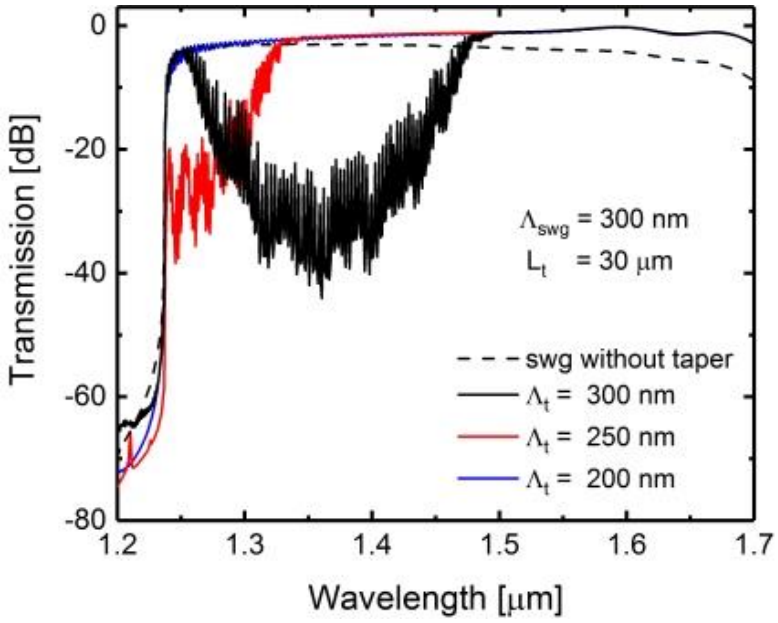

Figure 2.16: Wavelength dependent transmission response of a uniform SWG waveguide with $W_g = W$ for different values of grating period in the taper region. Calculations are carried out using Lumerical 3D-FDTD for grating width W_g = 500 nm; slab-height h = 0 nm and duty-cycle δ = 0.7

SWG waveguide without taper is significantly lossy ($\sim$ 4 dB) arising from the mode-mismatch at the two interfaces. Now, when a linear taper with $\Lambda_t = \Lambda_{swg}$ = 300 nm is inserted between the access waveguide and SWG waveguide at the two interfaces, we observe lot of oscillations and a lossy transmission response. This is because the tapers at both the ends have higher effective refractive index compared to the SWG waveguide at the center due to the additional silicon bridge elements. This results in the formation of localized Bragg zones in the taper region which makes the SWG waveguide act like a cavity with the taper regions acting as mirrors thereby resulting in Fabry-Perot

response. This can be resolved by reducing the grating period in the taper region which will in turn reduce the n_{eff} value. As seen in the Figure 2.16, when Λ_t = 250 nm, the Fabry-Perot oscillations have relatively reduced, and when Λ_t = 200 nm, we get the desired smooth transmission response in the wavelength range of interest with insertion loss IL $<$ 1 dB. Thus we can conclude that when $W_g = W$, the grating period in the taper region should be significantly less than the grating period in the SWG region, i.e. $\Lambda_t < \Lambda_{swg}$ to enable smooth and adiabatic transition of the guided mode.

Next, when the grating width W_g is considerably higher than the input/output waveguide (case ii), a linear or quadratic taper profile can be used for mode matching [132]. In this case, we have used a linear taper profile by linearly decreasing the access waveguide width and linearly increasing the SWG waveguide width towards the center and vice-versa as shown in Figure 2.15(d). Here also, we considered different grating periods in the taper region for reasons already discussed above. Figure 2.17 shows the

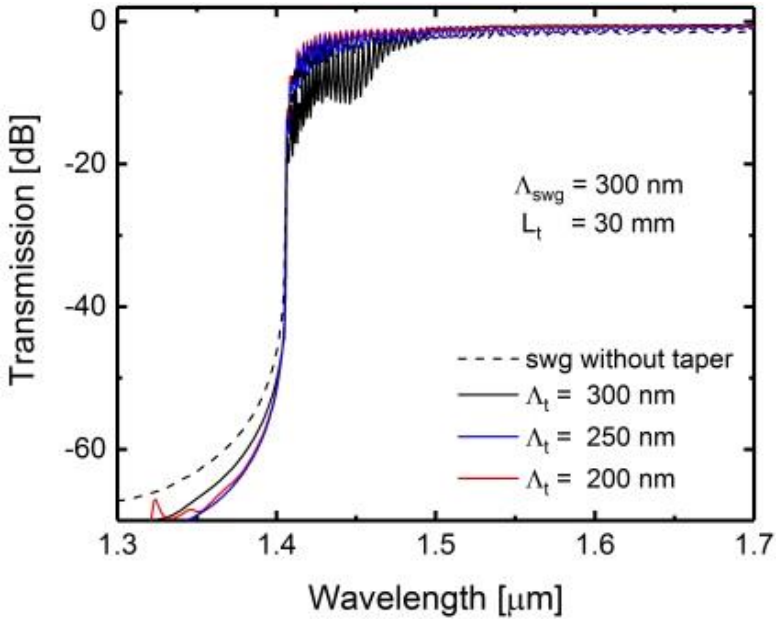

Figure 2.17: Wavelength dependent transmission response of a uniform SWG waveguide with $W_g > W$ for different values of grating period in the taper region. Calculations are carried out using Lumerical 3D-FDTD for Λ = 300 nm, grating width W_g = 800 nm; slab-height h = 0 nm and duty-cycle δ = 0.7.

transmission response simulated using Lumerical 3-D FDTD for SWG waveguide with Λ_{swg} = 300 nm, W_g = 800 nm, W = 500 nm and Λ_t as a variable parameter. We observe that the increase in SWG grating width has shifted the transmission band-edge (λ_{edge}) towards longer wavelengths. Also, for lower values of Λ_t, the transmitted wavelengths

falling in the SWG regime ($\lambda > 1600$ nm) are nearly ripple-free and the insertion loss is very less (< 0.2 dB). However, there are still significant ripples in the transmission/reflection band-edge which can be smoothened by suitable apodization technique which is discussed in Chapter-4. It should be noted that a taper with linear grating width profile is not always an appropriate solution and one can go for alternate taper geometries which can effectively avoid the Bragg zones, at the same time provide adiabatic mode transition [132].

2.4 Summary

In this chapter, we have discussed the theory of sub-wavelength gratings and carried out a detailed study of different geometry parameters that are instrumental in designing a sub-wavelength grating waveguide in a 220 nm SOI platform. This was followed by the investigation of critical design parameters that influence the grating response such as grating period (Λ), duty-cycle (δ), corrugation width (d), slab-height (h) and grating width (W_g), which are summarized in Table 2.1. With the help of simulations, it

Table 2.1: Influence of different geometrical parameters on grating response when other parameters are kept constant

Parameters	λ_{edge}	$\Delta\lambda$	ER
Grating period (Λ)	✓		
Duty-cycle (δ)	✓	✓	✓
Corrugation width (d)	✓	✓	✓
Grating etch depth (H-h)	✓	✓	✓
Grating width (W_g)	✓	✓	

has been established that the first order band-edge wavelength λ_{edge} will be affected no matter which grating parameter is being changed. At the same time, the stop-band width and extinction ratio (ER) of the grating response is primarily decided by the d, δ and etch depth of the grating. For a shallow etch depth and fixed d, the stop-bandwidth can be increased by increasing the value of W_g. Finally, we have investigated the integration of SWG waveguides with the input/output photonic wire waveguides using efficient spot size converters that ensure adiabatic mode transition. Thus we can suitably design the grating parameters depending on the specific applications as discussed in the following

chapters.

CHAPTER 3

Broadband Add-Drop Filter/Switch

Optical add-drop filter is a key component for wavelength division (de-)multiplexing and switching systems for high density data communications. For silicon photonics, most of the optical filters demonstrated till date are based on microring resonators [25, 133], arrayed waveguide gratings [134], photonic crystal cavities [135], distributed Bragg reflectors [136] etc. These filters are suitable for single channel (or a comb of narrowband frequencies) add-drop multiplexing. However, it is also desirable to have on-chip tunable optical flat-top filters which can either switch, route or diplex a large bandwidth of optical signals and/or channels. Optical add-drop filters with flat top response have been explored before using contra-directional couplers [137], wideband CROW filetrs [110, 138], 2D PhC waveguides [139] and MZI designed with SWG and/or DBR structures [140, 141]. However, these devices have limited optical bandwidth (BW $\sim$ 10 nm) but with a reasonable sideband suppression ($\sim$ 35 dB).

In this chapter, we have proposed and demonstrated an integrated optical ultra wideband add-drop filter/switch circuit in SOI platform by integrating SWG waveguides in two arms of a 2 $\times$ 2 MZI, which is designed by cascading two wavelength independent directional couplers (WIDCs) [142] acting as 3-dB power splitters. The circuit is designed to act as a C and L wavelength band splitter, i.e., the entire C band and L band can be separated into the drop port and cross/bar port of the MZI, respectively. The specially designed SWG structures and WIDCs are the key for the MZI to act as an ultra-broadband wavelength de-multiplexer. Moreover, five different slab integrated microheaters are used for thermo-optic tuning and/or switching. In the following sections, we will initially discuss about detail device description and design principle of add-drop filter circuit along with functioning of each microheater. This will be followed by the fabrication and experimental results.

3.1 Device Description and Design

The proposed device has been designed to be fabricated in a SOI substrate with device layer thickness of 220 nm, BOX layer thickness of 2 μm and substrate handling wafer thickness of 500 μm. A topological optical circuit layout of the device has been shown schematically in Figure 3.1. A balanced 2×2 MZI is formed by cascading two

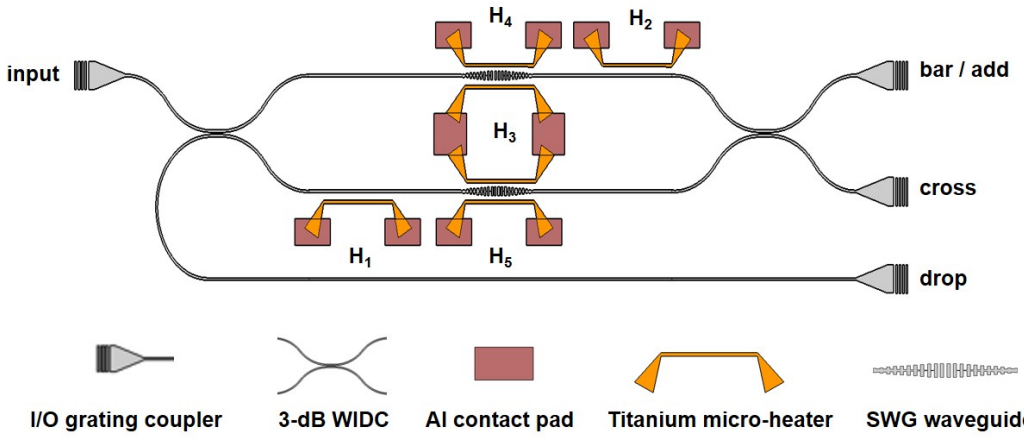

Figure 3.1: Schematic illustration of the proposed 2×2 MZI based ultra-broadband add-drop filter device integrated with five microheaters (H_1-H_5) at different locations.

WIDC 3-dB power splitters which offer uniform power splitting over a broad wavelength span of $\sim$ 100 nm at operating wavelengths centering at $\lambda \sim 1550$ nm. The design of the WIDC is taken directly from Ref.[142] and only a brief description of the same is given in the Appendix A for completeness. The WIDC waveguides as well as the access waveguides are of same cross-sectional geometry (as shown schematically in Figs. 3.2(a) and 3.2(b)), designed for single-mode guidance for TE-polarization over a broad wavelength band centering at $\lambda \sim 1550$ nm (W = 350 nm, G_{WIDC} = 150 nm, H = 220 nm, h = 160 nm). Two identical SWG waveguides are adiabatically integrated in two arms of the MZI. Following the working principle of a balanced MZI, the input light signal power is divided equally into two MZI arms and travel same optical path length to reach SWG waveguides in both arms. The stop-band of SWG waveguide is reflected back into the drop port whereas the cross port will have the same spectral response as that of a transmission characteristics of a single SWG waveguide. Since the MZI is formed by cascading two WIDCs (acting as 3-dB power splitters), flat-top spectral responses are expected at both drop- and cross ports. As mentioned

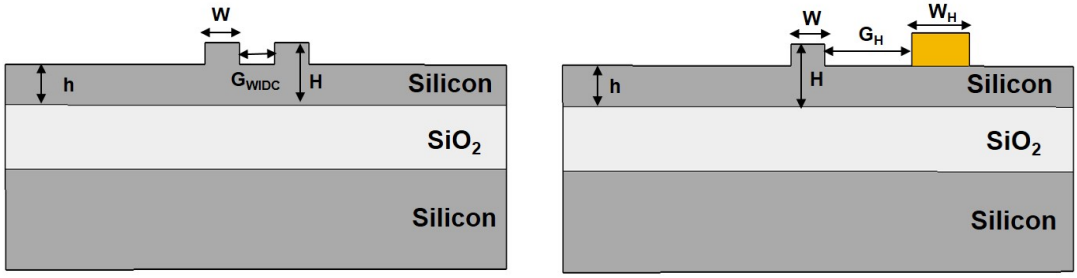

(a) (b)

Figure 3.2: Cross-sectional schematic of the (a) WIDC rib waveguide with typical parameters W = 350 nm; h = 160 nm; H = 220 nm; G_{WIDC} = 150 nm; (b) rib waveguide with integrated microheater in the slab region with typical parameter values: G_H = 3 μm, W_H = 1.5 μm, t_H = 100 nm.

earlier, five different slab integrated Ti strip microheaters (H_1-H_5) are placed at different locations as shown in Figure 3.1 to actively tune the device characteristics. The slab integrated configuration is chosen for thermo-optic phase shifting, in contrast to the conventional microheater integrated over the top cladding oxide, due to its lower switching time [126]. Figure 3.2(b) shows the cross-sectional scheme of a microheater of $\sim$ 100 nm thickness integrated with the rib waveguide (W_H = 1.5 μm, G_H = 3 μm). H_1 microheater is capable of controlling transmission at all the three output ports via corresponding phase detuning: switching passband output power from cross port to bar port or vice-versa as well as maximizing the drop port response. H_2 microheater plays a vital role in tuning the power output at the bar port as well as cross port without affecting the drop port power. H_3 is a pair of micro-heaters placed adjacent to the two identical SWG waveguides which are probed together to tune the band-edge to the desired wavelength. H_4 and H_5 are auxiliary microheaters to tune the transmission response of the two SWG waveguides individually. Since the WIDC and microheater designs are detailed elsewhere [142, 143, 144], we will focus only on the design of SWG waveguides to be integrated with the MZI arms and thermo-optic tuning of SWG waveguide in the following subsections.

3.1.1 SWG waveguide design: C/L band splitter

The proposed SWG waveguide design is intended to have the transmission band-edge around $\lambda_{edge} \sim$ 1565 nm such that the entire L band (1565 nm - 1625 nm) is transmitted through the waveguide and the C band (1530 nm - 1565 nm) is reflected back to the input. We have chosen the SWG design parameters such that the entire MZI structure including input/output grating couplers can be defined by a single-step lithography and subsequent single-step dry etching process. Since the WIDCs were being used as broadband 3-dB power splitters in the MZI circuit, the slab height of the SWG waveguides were also kept same as that of the WIDCs, i.e. h = 160 nm. The next task was to fix the SWG waveguide width W_{swg} and grating period Λ so as to have the λ_{edge} around 1550 nm and $\Delta\lambda$ around 50 nm. Taking insights from Chapter-2, the bandstructure calculations were carried out for different combinations of W_{swg} and Λ keeping the duty-cycle δ constant (0.5), as shown in Table 3.1. Since the SWG waveguides are shallow etched, a larger width is required to obtain stronger effective index contrast in the grating region to achieve broadband reflection as given in Equation 2.11. It was observed that

Table 3.1: SWG waveguide design parameters

Λ	W_{swg}	λ_{edge}	$\Delta\lambda$
300 nm	1 μm	1600 nm	46 nm
	2 μm	1639 nm	80 nm
285 nm	1 μm	1546 nm	1492 nm
	2 μm	1565nm	65 nm

SWG waveguide with W_{swg} = 2 μm and period Λ = 285 nm with duty cycle δ = 0.5 had transmission band-edge around λ = 1565 nm with $\Delta\lambda > 50$ nm. At the same time, the SWG waveguide should be designed to be integrated adiabatically in the balanced MZI arms constructed using WIDC based 3-dB power splitters. For this, we included 10-μm long tapered waveguides between WIDC access waveguides and SWGs by linearly decreasing/increasing the rib waveguide width and linearly increasing/decreasing the SWG waveguide width; such a taper design offers low loss as discussed in Section 2.3 of Chapter-2. The width of WIDC access waveguides (W = 350 nm) are adiabatically converted into SWG waveguides. The 3D view of the proposed SWG waveguide with input out tapers is shown in Figure 3.4. Longer the taper length, smaller would be the insertion loss for the SWG waveguides as well as reduction in unwanted lobes at

the band-edges. Again for a given W_{swg}, longer the SWG length higher is the stopband

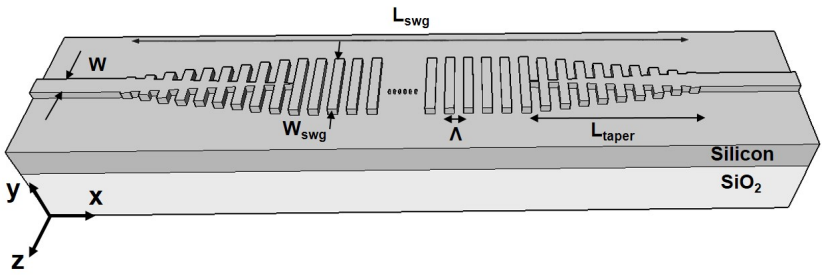

Figure 3.4: 3-D schematic view of the SWG waveguide with the input/output tapered access waveguides.

extinction. However, shorter length of SWG (45-μm) is used for simulation to reduce computational budget. Table 3.2 lists the summary of the design parameters chosen for demonstrating SWG waveguide as a C/L band splitter. Figure 3.5(a) shows the simulated (Lumerical 3D-FDTD) transmission and reflection characteristics of a SWG waveguide with design parameters given in Table 3.2. It clearly exhibits a passband or

Table 3.2: Optimized SWG waveguide design parameters

Choice of parameters	Value	Remarks
d	60 nm	Allows single step lithography for device fabrication including grating couplers and access waveguides for TE-mode guidance
W_{swg}	2 μm	Broadband reflection (exceeding 50 nm)
Λ, δ	285 nm, 0.5	Transmission band-edge around 1565 nm with stronger extinction
L_{swg}+2L_t	45 μm	Decides the filter extinction ratio

fundamental stopband edge at $\lambda_{edge} \sim$ 1565 nm (separating C and L bands). A broad stopband (1500 nm $\lesssim \lambda \lesssim$ 1565 nm) is reflected back into the input side whereas an ultra-broadband ($\lambda \gtrsim$ 1565 nm) is transmitted with a nearly flat-top response. However,

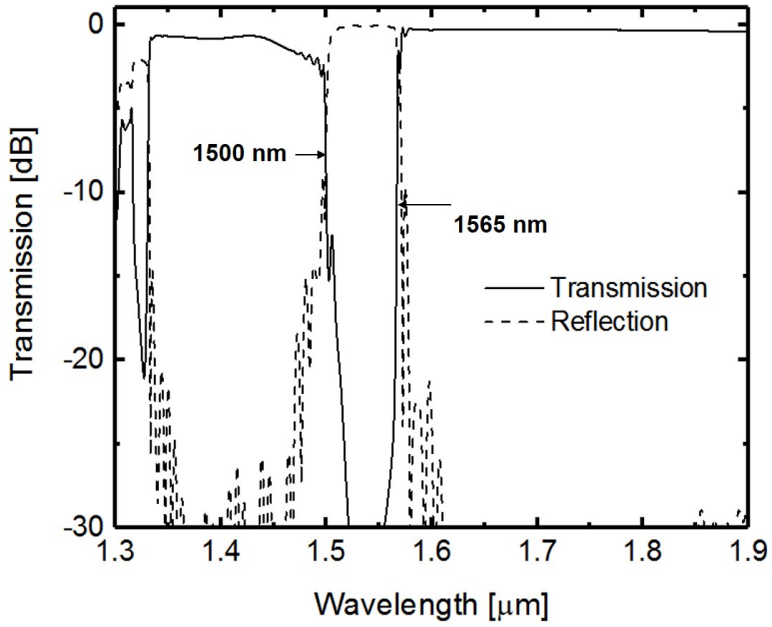

(a)

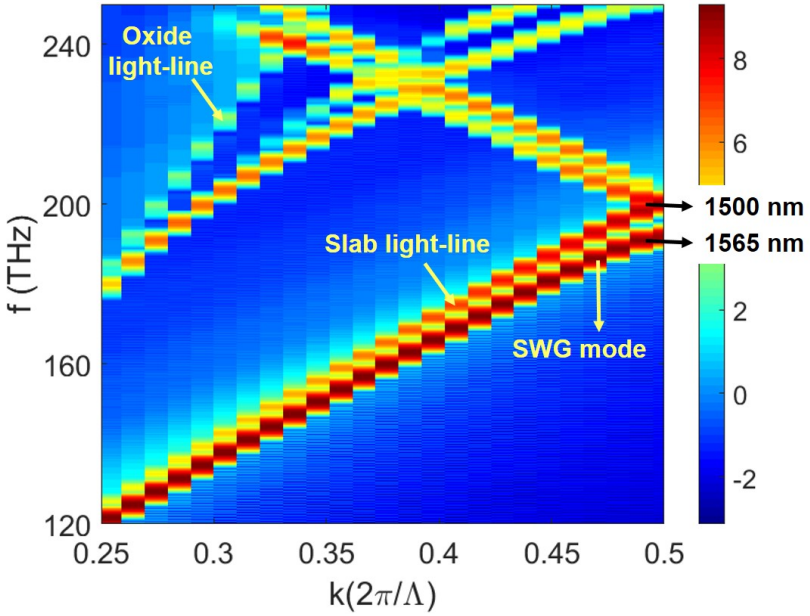

(b)

Figure 3.5: (a) Simulated transmission characteristics (Lumerical 3D FDTD Solutions) of a 45-μm-long SWG waveguide (including 10-μm tapers at both ends) for TE-polarized guided modes and (b) the corresponding band-structure calculation. See text for design parameters.

stopband is reflected with a relatively higher amplitude than that of transmission band. This is expected as the field amplitude within stopband decays as soon as it starts propagating through the SWG waveguide, whereas the field amplitude in transmission band will experience diffraction limited losses through the entire SWG waveguide length.

However, this loss is found to be < 0.2 dB. The higher order transmission band at $\lambda < 1500$ nm experiences even higher loss because of coupling to substrate modes. This is clarified by simulating the corresponding bandstructure diagram for the SWG waveguide as shown in Figure 3.5(b). Due to a finite slab height of 160 nm, there is a slab-lightline in addition to the cladding lightline as discussed Section 2.2.3 in Chapter-2. Since the higher order transmission band ($\lambda < 1500$ nm) lies above the slab lightline, it is being coupled to substrate modes. Figure 3.6 shows the electric field distribution of the guided SWG mode for λ = 1575 nm lying in the pass-band (top) and for λ = 1550 nm lying in the reflection band (bottom). At λ = 1575 nm, the fundamental TE polar-

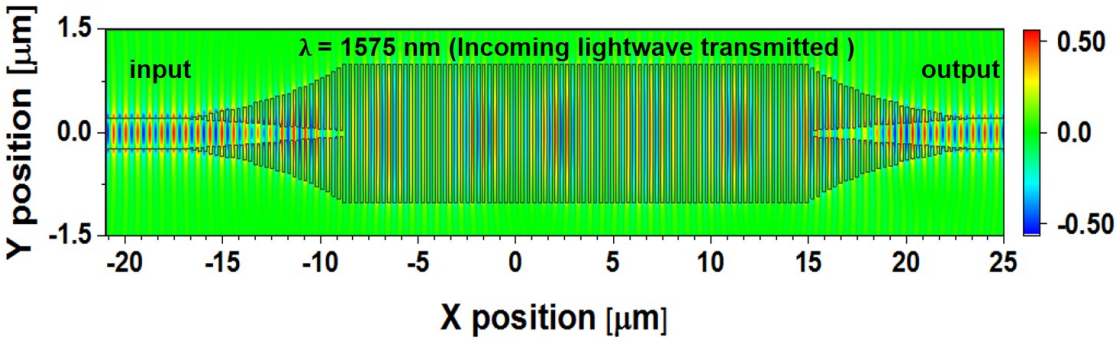

(a)

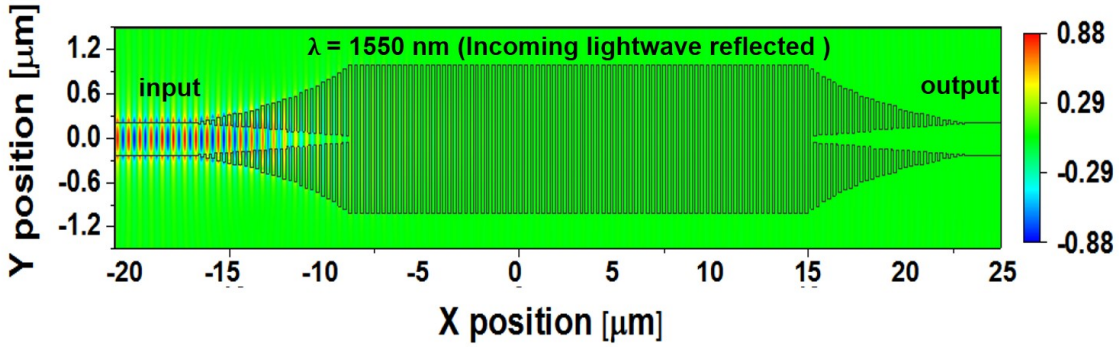

(b)

Figure 3.6: Electric field distribution of the guided SWG mode for (a) λ = 1575 nm lying in the pass-band and (b) for λ = 1550 nm lying in the reflection band.

ized index guided mode from the input access waveguide gets adiabatically expanded via the SWG waveguide taper lies, propagates through the periodic medium as Bloch modes and gets converted back to the index-guided mode at the output waveguide via the output SWG waveguide taper (see Figure 3.6(a)). On the other hand, when λ = 1550 nm, the incoming lightwave undergoes destructive interference in the forward direction

and gets completely reflected back into the input waveguide (see Figure 3.6(b)). Next, we analyze the sensitivity of the SWG waveguide to different grating parameters. As discussed in Chapter-2, the dependence of λ_{edge} with Λ and effective index (n_{eff}) of a guided mode at $\lambda \sim \lambda_{edge}$ can be approximately modeled from the knowledge of 1^{st} order Bragg condition ($\lambda_B = 2n_{eff}\Lambda$) for a given set of design parameters (W_{swg}, H, h):

$$\Delta\lambda_{edge} \approxeq 2(n_{eff}\Delta\Lambda + \Lambda\Delta n_{eff}) \tag{3.1}$$

where,

$$n_{eff} \equiv n_{eff}(\Lambda, \delta, \lambda, T) \tag{3.2}$$

and

$$\Delta n_{eff} \equiv \frac{\partial n_{eff}}{\partial \Lambda}\Delta\Lambda + \frac{\partial n_{eff}}{\partial \delta}\Delta\delta + \frac{\partial n_{eff}}{\partial \lambda}\Delta\lambda + \frac{\partial n_{eff}}{\partial T}\Delta T \tag{3.3}$$

using first order approximation in Taylor's series. In the above equation, the last term $\frac{\partial n_{eff}}{\partial T}$ is the thermo-optic co-efficient for SWG waveguide at a given operating temperature T. It has been shown earlier that the value of $\frac{\partial n_{eff}}{\partial T}$ for a conventional single-mode photonic wire/rib waveguide with top air cladding is slightly lower ($1.79 \times 10^{-4}K^{-1}$) than that of bulk Si ($1.86 \times 10^{-4}K^{-1}$) [145]. Since the proposed SWG waveguide is shallow etched and width W_{swg} is relatively large (2 μm), its thermo-optic coefficient is found to be nearly same as that of bulk silicon. Figure 3.7(a) shows the 3D FDTD simulated transmission characteristics for two different values of Λ (275 nm and 285 nm) keeping δ = 0.5 and h = 160 nm. It can be observed that for grating period detuning of $\Delta\Lambda$ = 10 nm, there is a significant shift in band edge, $\Delta\lambda_{edge} \sim$ 38 nm. We also studied the sensitivity of SWG waveguide to small variations in δ, W_g and h. Figure 3.7(b), 3.7(c) and 3.7(d) show the same for two different values of δ (0.5 and 0.6), W_g (2 μm and 2.1 μm) and h (160 nm and 170 nm) respectively, keeping Λ = 285 nm. There is no much significant change in band-edge position ($\sim$ 1 nm) when W_g is increased by 100 nm. However, when δ and h are increased, the effective index of the SWG waveguide increases and the transmission band-edge (λ_{edge}) red shifts by 10 nm. Also, small variations in slab height significantly affect the coupling coefficient thereby changing the stopband width. This shows that the SWG waveguide response is very sensitive to even small variations in grating parameters. Though the grating period can be defined accurately in mask design, the accuracy in duty cycle and slab height is highly depen-

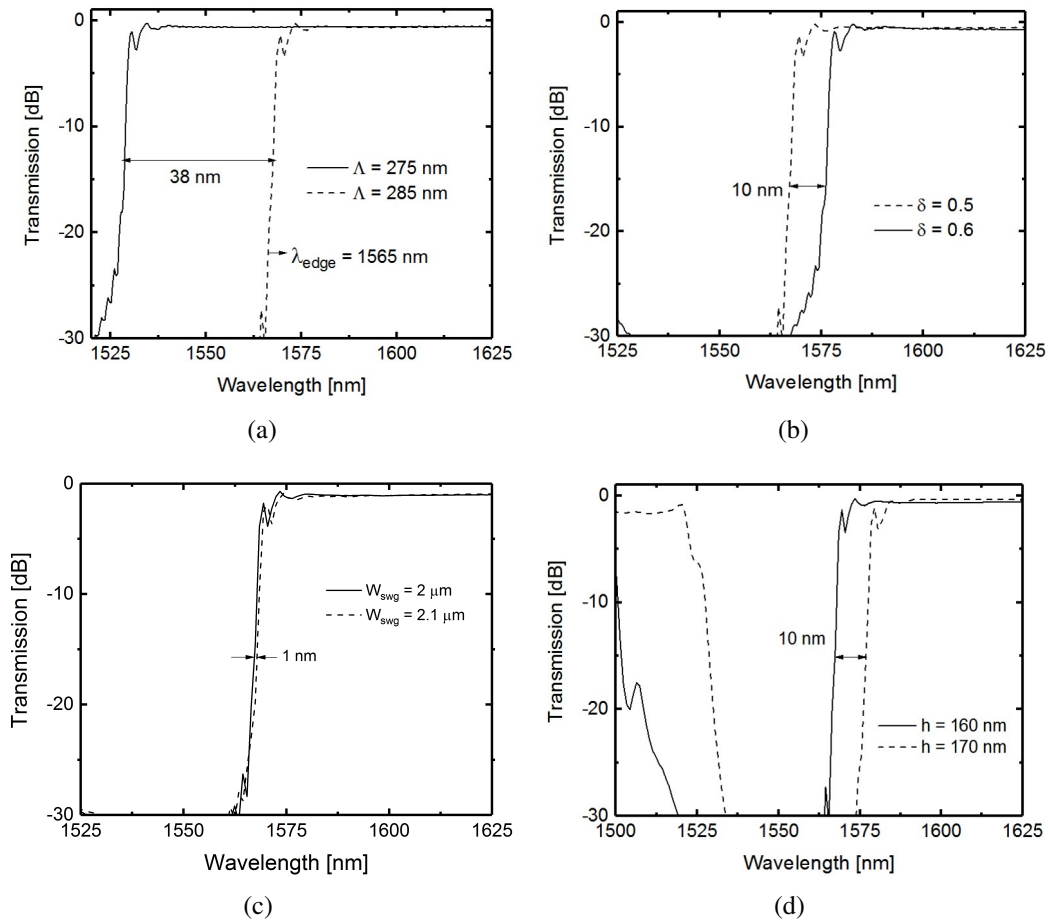

Figure 3.7: Simulated transmission characteristics (Lumerical 3D FDTD Solutions) for TE-polarized guided mode: (a) λ = 275 nm and 285 nm for δ = 0.5, W_{swg} = 2 μm and h = 160 nm, (b) δ = 0.5 and 0.6 for Λ = 285 nm, W_{swg} = 2 μm and h = 160 nm, (c) W_{swg} = 2 μm and 2.1 μm for λ = 285 nm, δ = 0.5 and h = 160 nm and (d) h = 160 nm and 170 nm for λ = 285 nm, δ = 0.5 and W_{swg} = 2 μm.

dent on fabrication related process controls. Nevertheless, the band-edge λ_{edge} of any fabricated device can be red-shifted actively to a desired value via thermo-optic effect. By integrating microheaters in the proposed integrated optical circuit, one can not only detune λ_{edge}, but also detune/compensate for the phases of MZI arms for switching applications.

3.1.2 Design of Thermo-Optic Phase-Shifter

As discussed earlier, the integrated optical MZI is designed with shallow-etched waveguide with slab thickness of h = 160 nm. This in fact enables us to integrate resistive

metal microheater (e.g. Ti strip of width $\sim$ 1.5 μm, thickness $\sim$ 100 nm) of length L_H, directly on the slab and parallel to waveguide axis but at a safe distance so as to avoid unwanted absorption of the guided mode through evanescent field [143]. Typi-

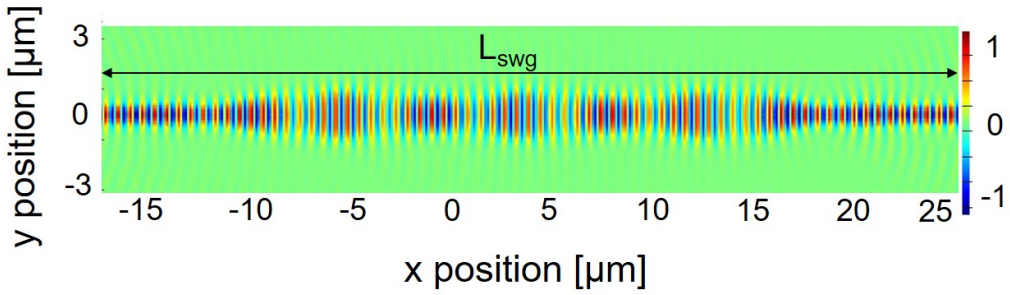

Figure 3.8: The fundamental mode propagation profile (TE-polarized) in the proposed SWG waveguide of length 45-μm (including input/output tapers of length 10-μm each); the simulation results are obtained using Lumerical 2.5D FDTD simulation tool.

cally, $\sim$3$\pm$0.5 μm separation between microheater and waveguide axis is considered to be a safe distance [126]. This is reconfirmed by visualizing the lateral field distribution of the guided fundamental mode (TE-polarized) in the SWG waveguide as shown in Figure 3.8; the evanescent field is insignificant beyond 3-μm from the SWG waveguide edge. This result was obtained using Lumerical 2.5D FDTD simulation of the proposed SWG waveguide of length 45-μm including input/output tapers of length 10-μm each. The planar temperature profile (120 nm above Si-SiO_2 interface) of a microheater dissipating an electrical power of P_E = 15 mW has been shown in Figure 3.9. This planar

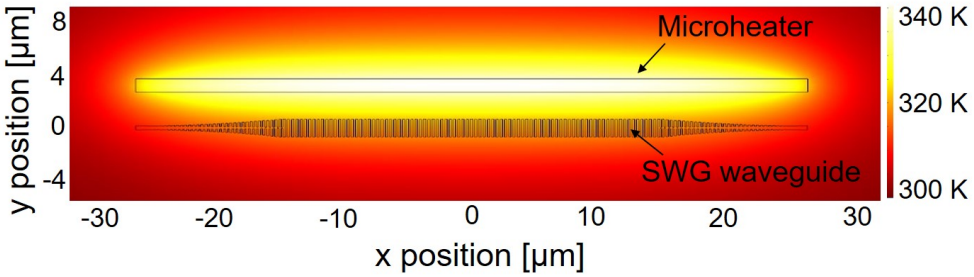

Figure 3.9: 2D temperature profile of the proposed SWG waveguide microheater (L_H = 45 μm) at 120 nm above the Si-SiO_2 interface. This profile was extracted by 3D computation using COMSOL Multiphysics Simulator in which 15 mW of electrical power was assumed to be dissipated as heat uniformly along the waveguide

temperature profile was extracted from a 3-D temperature profile of the microheater of length L_H = 45 μm (same as that SWG waveguide length) computed by COMSOL Multiphysics. The estimated temperature rise is ~ 18.5K (ΔT) above room temperature along SWG waveguide axis (and nearly uniform). However, for microheater waveguide phase-shifters (H_1 and H_2) of same length ($L_H = 45$ μm) and same electrical power consumption (P_E = 15 mW), the value of ΔT is found to be relatively higher ($\sim$ 22K). This is expected due to their closer proximity to waveguide axis as shown in Figure 3.10. Even though G_H is same in both the cases, the effective heat experienced by

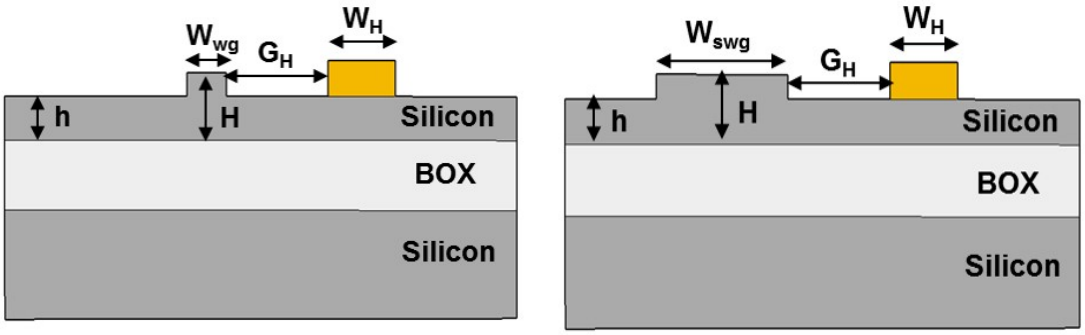

(a) (b)

Figure 3.10: Cross-sectional schematic of metal microheaters integrated adjacent to (a) rib waveguide and (b) SWG waveguide.

the center region of SWG waveguide (Figure 3.10(b)) is less compared to that of the access rib waveguide (Figure 3.10(a)) due to its higher width and hence lesser proximity. Figure 3.11 shows the calculated ΔT as a function of distributed electrical power consumption p_H (mW/μm), for a SWG waveguide and a phase-shifter rib waveguide. Their linear characteristics can be defined as:

$$\Delta T = S_H \cdot p_H \tag{3.4}$$

where S_H measures the waveguide microheater sensitivity which may be expressed in K-μm/mW. Thus for the given microheater design, we obtain the S_H values for SWG waveguide (S_H^{swg}) and rib waveguide (S_H^{rib}) as $\sim$ 56K-μm/mW and $\sim$ 65 K-μm/mW, respectively. The resulting phase change (at an operating wavelength λ) in a rib waveguide phase-shifter integrated with a microheater of length of L_H can be expressed using

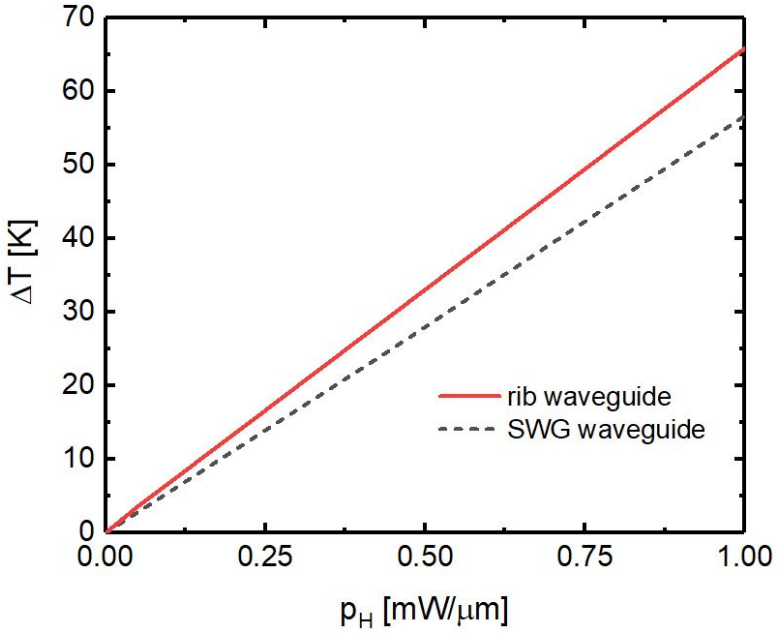

Figure 3.11: Calculated ΔT as a function of p_H (mW/μm) for a SWG waveguide and a rib waveguide used in the proposed MZI based add-drop filter.

Equation 3.3 (ignoring thermal expansion):

$$\Delta\Phi \approx S_H^{rib} \cdot \left(\frac{2\pi}{\lambda} \cdot \frac{\partial n_{eff}}{\partial T}\right) \cdot P_E \tag{3.5}$$

where $P_E = p_H \cdot L_H$. Similarly, for a designed value of Λ, the band-edge of the SWG waveguide can be detuned as a function of P_E and is derived from Equation 3.1 as:

$$\Delta\lambda_{edge} \approx S_H^{swg} \cdot \left(\frac{2\Lambda}{L_H} \cdot \frac{\partial n_{eff}}{\partial T}\right) \cdot P_E \tag{3.6}$$

It must be noted that this band-edge detuning is directly proportional to the differential change in SWG waveguide temperature. However, we need to ensure uniform heating along the SWG waveguide to maintain thermo-optically tuned band-edge profile intact. Thus if identical SWG waveguide microheaters are integrated in both arms of the MZI, there won't be any phase imbalance between them at any operating wavelength; passband transmission at both bar- and cross ports remain unaltered for equal electrical power consumption by both microheaters. All other microheaters (except the microheaters adjacent to SWG waveguides which are of same length as SWG waveguides) can be as long as possible so that desired thermo-optic phase change can be achieved at lower operating temperatures. For example, only a temperature rise of $\sim$

45 K is required for π phase-shift in a 100-μm-long waveguide microheater (L_H = 100 μm). For all our fabricated devices to be discussed in next section, the SWG waveguide length is 90 μm to obtain sharper band-edge and to integrate longer microheater (L_H = 100 μm) for its thermo-optic tuning at low temperatures.

3.2 Experimental Results and Discussion

All the devices were fabricated using the in-house facilities available in IIT Madras. The devices were fabricated in a commercially available 220 nm thick SOI substrate (2-μm BOX (SiO_2) layer thickness and 500-μm handle wafer thickness) using electron beam lithography (RAITH 150 TWO) and inductively coupled plasma reactive ion etching (OXFORD PlasmaLab System 100). The detailed fabrication process flow and experimental measurements are described in the following sections:

3.2.1 Device fabrication

Two samples S_1 and S_2 were fabricated; Sample S_1 was fabricated to demonstrate the broadband wavelength filtering characteristics of SWG waveguide as well as the add-drop filtering characteristics of the MZI circuit. S_2 was customized for carrying out thermo-optic tuning and switching studies. The details regarding the list of devices in each sample and the respective design considerations are listed in Table 3.3. The

Table 3.3: List of fabricated devices for active and passive characterization

Sample	Devices in each set	Design parameters	Remarks
S_1	$D_{\#1}$: Ref. rib waveguide	L_{swg} = 90 μm, W_{swg} = 2 μm	
	$D_{\#2}$: Ref. SWG waveguide	Λ = 285 nm, 275 nm, δ = 0.5	Passive
12 sets	$D_{\#3}$: Ref. MZI device	L_{DC} = 4 μm, 4.5 μm, 5 μm	characteristics
	$D_{\#4}$: Add-drop filter	G_{DC} = 150 nm	
S_2	$D_{H\#1}$: Ref. rib waveguide	L_{swg} = 90 μm, W_{swg} = 2 μm	
	$D_{H\#2}$: Ref. SWG waveguide	Λ = 285 nm, δ = 0.5	
12 sets		L_{DC} = 4.5 μm, G_{DC} = 150 nm	
	$D_{H\#3}$: Add-drop filter	L_H = 100 μm (SWG)	Active
	(with microheaters)	L_H = 400 μm (waveguide)	characteristics
		W_H = 1.5 μm, $t_H \sim$ 100 nm	
		G_H = 3 μm	

subscripts of $D_{\#\#}$ means the set number and the device number in that particular set respectively, i.e. D_{12} means the device 2 in set-1. In sample S_2 which is used for thermo-optic characterization, the devices are labelled as $D_{H\#\#}$ which in order denote the heater sample, set number and device number. All the devices in S_1 and S_2 were integrated with rib waveguides (W = 350 nm, H = 220 nm, and h = 160 nm) and terminated on either sides with grating couplers for efficient coupling of light. Figure 3.12(a) shows the mask layout of a typical set of devices in sample S_1 designed using Raith Nanosuite software. It consists of the reference rib waveguide ($D_{\#1}$), reference

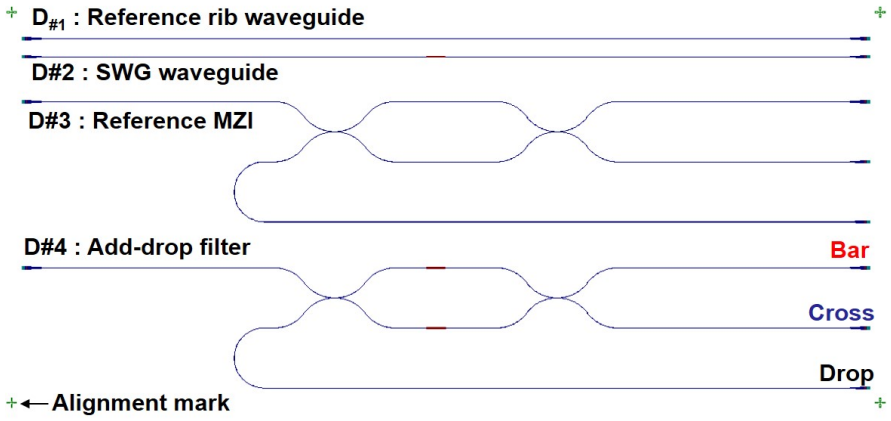

(a)

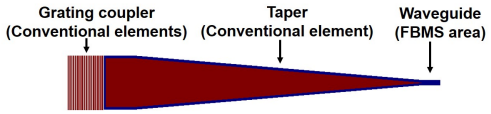

(b)

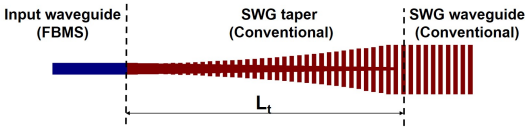

(c)

Figure 3.12: (a) Typical mask layout of a set of devices to be fabricated along with the alignment marks; A zoomed-in view of (b) the grating coupler region and (c) SWG spot-size converter integrating the photonic wire waveguide and the SWG waveguide.

SWG waveguide ($D_{\#2}$), a balanced MZI device ($D_{\#3}$) and the proposed add-drop filter circuit ($D_{\#4}$). The masks were designed in GDS II format using RAITH Nanosuite software. The grating coupler is designed (period - 610 nm, duty-cycle - 0.5) for the fiber-to-chip light coupling over a broad wavelength range (3-dB bandwidth $\sim$ 70 nm) centering at λ = 1550 nm. Figure 3.12(b) shows the zoomed-in view of the grating coupler region defined in the mask file. The gratings are gradually tapered towards the access waveguides via a 12 μm $\times$ 12 μm taper structure over a length of 100 μm

to match the fiber mode with the waveguide mode. The overall length (input grating coupler to output grating coupler) of all fabricated devices (including reference waveguides) is kept fixed at 5 mm. Further details regarding the design parameters of grating couplers are given in Appendix A. The length of all the fabricated SWG waveguides is kept same L_{swg} = 90 μm, which include input/output tapers of length 10 μm each. Lateral distance between the grating couplers of successive devices were kept 300 μm. The maximum radius of the access bend waveguides is kept 180 μm to avoid the bent induced coupling loss [126]. The grating couplers, taper region and sub-wavelength gratings were defined as conventional elements where the electron beam expose over the pattern within a write-field. However, for stitch free patterning, the photonic rib waveguides including directional couplers are defined using fixed beam moving stage (FBMS) exposure scheme. A brief description on FBMS and conventional patterning strategies is described in Appendix-C. A zoomed view of the SWG waveguide region integrated with the input waveguide via. an adiabatic mode converter is shown in Figure 3.12(c).

The passive device structures were defined using single step electron beam lithography (EBL) and subsequent inductively coupled plasma reactive ion etching process. A summary of the fabrication process steps in electron beam lithography using HSQ as resist mask is given in Figure 3.13. The SOI sample was initially cleaned to remove the

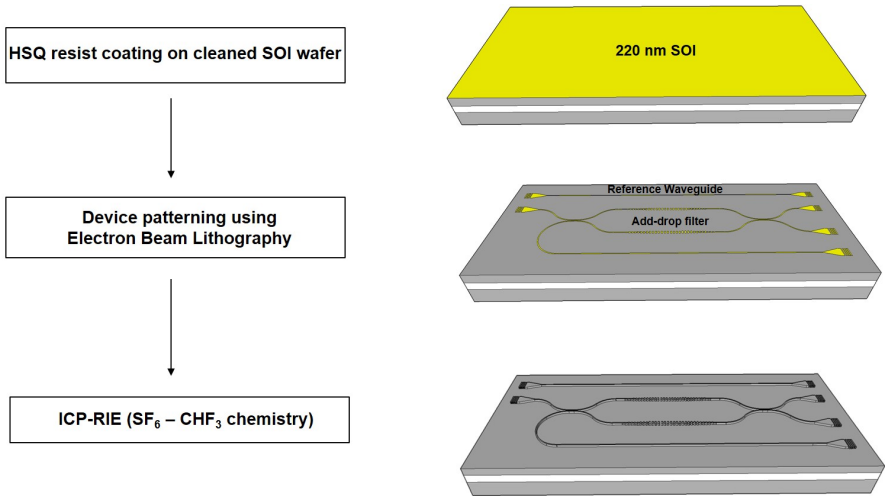

Figure 3.13: Schematic illustration of the process steps used for fabricating the device structures

traces of any organic and inorganic impurities. The detailed cleaning procedure is out-

lined in Appendix C. The cleaned sample was then dehydrated at 180^0C for 10 minutes

Table 3.4: Optimized spin coating parameters for obtaining $\sim$ 100 nm thick HSQ resist on SOI.

Spin parameters	Thickness
Step-1 (spread) Speed : 100 rpm Acceleration : 100 rpm/s Time : 10 s **Step-2 (coat)** Speed : 3000 rpm Acceleration : 1500 rpm/s Time : 30 s	100 nm

on a hot plate. It was then coated with negative tone e-beam resist (HSQ -Hydrogen silsesquioxane) with the spin parameters listed in Table 3.4. The spin coating procedure is detailed in Appendix C. The resist coated sample was then post-baked at 180^0C for 2 minutes. This was followed by the patterning of the devices using EBL system (Raith 150 TWO) with the optimized patterning parameters as given in Table 3.5. Post

Table 3.5: EBL system parameters and patterning parameters optimized for conventional and FBMS patterning on HSQ resist.

Column parameters	Patterning parameters
Acceleration voltage : 20 kV Aperture : 20 μm Working distance : 10 mm Write field : 100 μm $\times$ 100 μm	Area dose : 300 μC/cm^2 FBMS dose : 400 μC/cm^2 Area step size : 9.4 nm

lithography, the samples were developed using commercially available developer solution (MF-319) for 7 minutes and then post-baked at 300°C. This was followed by etching (etch depth $\sim$ 60 nm) of the patterns using optimized ICP-RIE recipe (Fluorine chemistry) given in Table 3.6. SF_6 was used as the silicon etchant and CHF_3 was used for passivation of sidewalls during the etching process. The gas phase and the surface reactions that happen using plasma etching process is given below:

Gas phase reaction:

$$SF_6 + e^- \rightarrow SF_5 + F + e^- \tag{3.7}$$

Surface reaction:

$$F + Si \rightarrow SiF_4 \tag{3.8}$$

The sample was etched for 8 seconds to obtain the desired etch depth of $\sim$ 60 nm. Figure 3.14(a) shows the SEM image of a set of fabricated devices (D_1 - reference rib

Table 3.6: Optimized ICP-RIE recipe for silicon etching

Parameter	Value
Gas flow rate	SF_6:CHF_3 :: 5:18 sccm
RF power	30 W
ICP power	1000 W
Pressure	15 mTorr
Temperature	20°C

waveguide, D_2 - reference rib waveguide integrated with SWG waveguide, D_3 - reference MZI device and D_4 - proposed add-drop filter). A zoomed SEM image of a rib waveguide to SWG waveguide transition taper region, directional coupler region and grating coupler are shown in Figures 3.14(b), 3.14(c) and 3.14(d) respectively. Table 3.7 compares the experimentally obtained parameters with the design parameters obtained using simulation. It can be seen that the SWG waveguides and the add-drop filter circuit is very much fabrication tolerant. Sample S_2 was fabricated to carry out

Table 3.7: Comparison of the designed and experimentally obtained device dimensions.

Parameter	Designed	Measured
SWG period (Λ)	285 nm	285 nm
SWG duty cycle (δ)	0.5	0.5 $\pm$ 0.1
Grating width (W_g)	2 μm	2 μm
Rib width (W)	360 nm	370 $\pm$ 10 nm
Slab height (h)	160 nm	160 nm $\pm$ 10 nm
DC gap (G_{DC})	150 nm	150 nm $\pm$ 20 nm
GC period (Λ_{DC})	610 nm	610 nm
GC duty cycle	0.5	0.5 $\pm$ 0.1

the thermo-optic switching and tuning studies. It consists of 12 sets of devices, each set consisting of D_{H1} - reference rib waveguide, D_{H2} - reference SWG waveguide and D_{H3} - add-drop filter /switch circuit along with the microheaters and contact pads. The mask layout of 1 set of devices is shown in Figure 3.15. The length of the MZI arms were kept longer in this sample (5 mm) to accommodate for the micro-heaters. The length of microheaters used for SWG tuning is 100 μm which is longer than the length of SWG waveguides (L_{swg} = 90 μm), whereas length of other microheaters used for phase tuning is 400 μm. The overall length of the devices were kept same, i.e. 5 mm. The

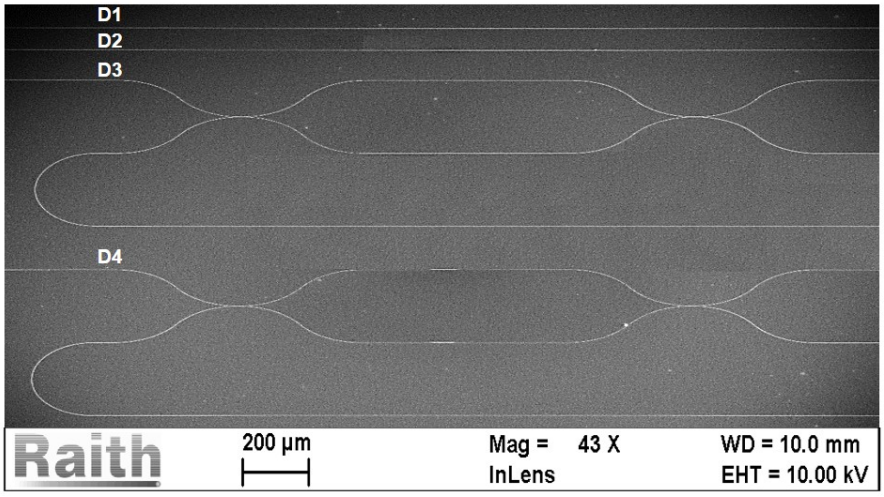

(a)

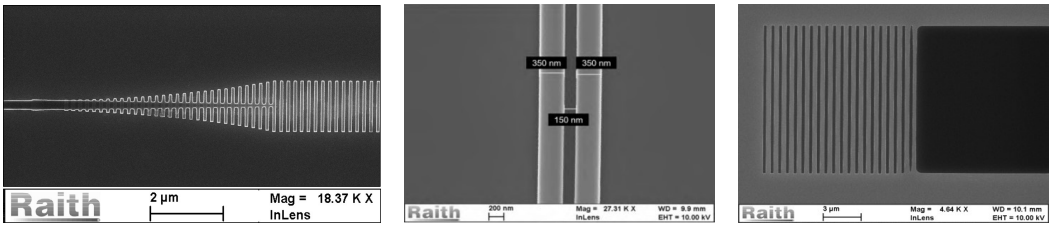

(b) (c) (d)

Figure 3.14: (a) SEM image of a set of fabricated devices : D_1 - reference rib waveguide, D_2 - reference rib waveguide integrated with SWG waveguide, D_3 - reference MZI device, D_4 - proposed add-drop filter device; zoomed SEM image of (b) an adiabatic spot-size converter between rib waveguide and SWG waveguide; (c) directional coupler region and (d) grating coupler region.

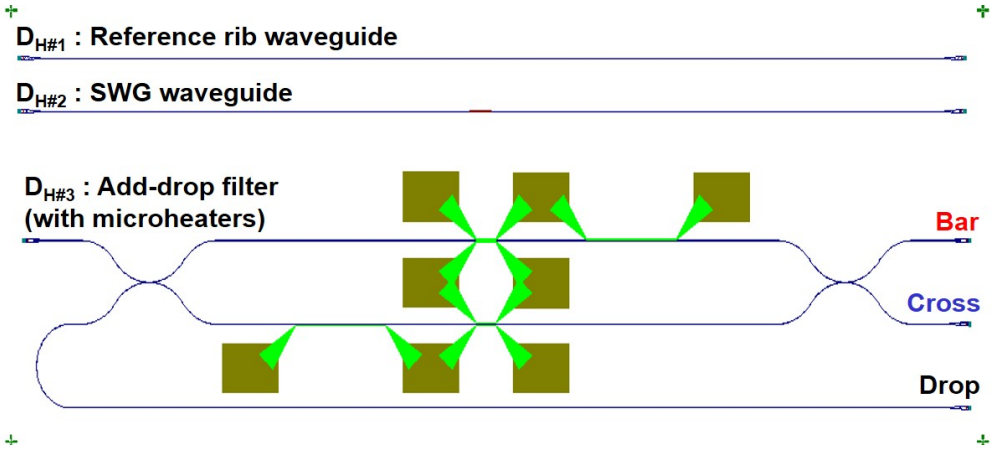

Figure 3.15: Mask-layout of one set of devices to be fabricated for carrying out thermo-optic measurements.

passive device structures were initially defined using EBL and ICP-RIE as discussed for sample S_1. The microheaters were defined in two cycles of metalization followed

by lift off processes: aluminum for the contact pads and titanium for the heaters [126]. Titanium microheaters were used for thermo-optic phase shifting and band-edge detuning because of its high melting point, high resistivity and absence of electro-migration at elevated temperatures when compared to other metals like gold, aluminium etc. The schematic flow charts describing the process steps for aluminium contact pads and titanium microheaters are illustrated in Figure 3.16 and detailed in the PhD thesis of Ramesh [126]. The windows for the contact pads and microheaters were defined us-

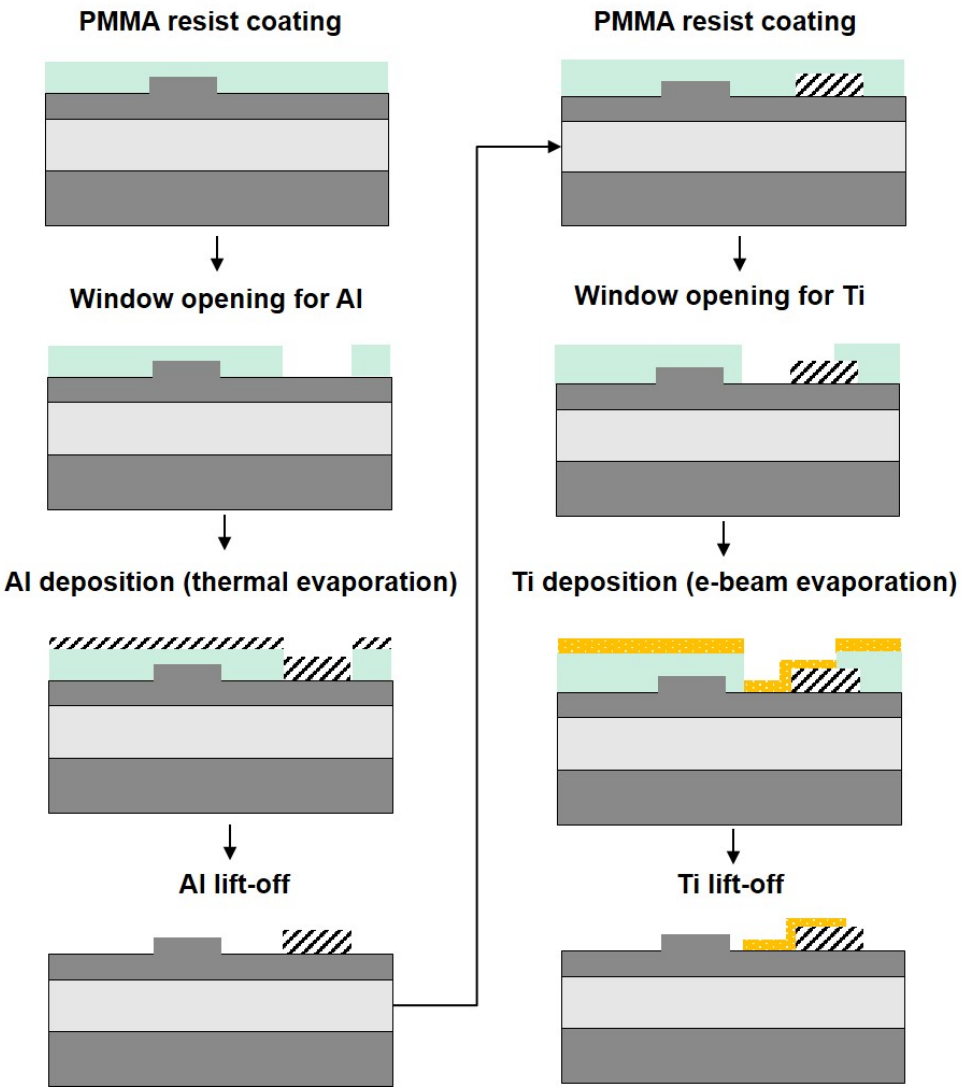

Figure 3.16: Schematic of the fabrication process flow for Aluminium contact pad and Titanium microheater integration

ing EBL using PMMA A8 resist with thickness $\sim$ 300 nm (thrice the thickness of the metal to be deposited). Aluminum was deposited using thermal evaporation technique (HPVT-305G) for a thickness of 100 nm whereas titanium was deposited by electron

beam evaporation technique (Hind Hi Vac BC-300T) for a thickness of 80 nm. The spin coat parameters and the optimized EBL parameters for patterning the windows for contact pads and microheaters are described in Appendix C. Figure 3.17(a) shows the zoomed SEM image of the fabricated device along with all the microheaters (H_1 - H_5). A zoomed SEM image of the SWG waveguide region with Titanium microheaters on

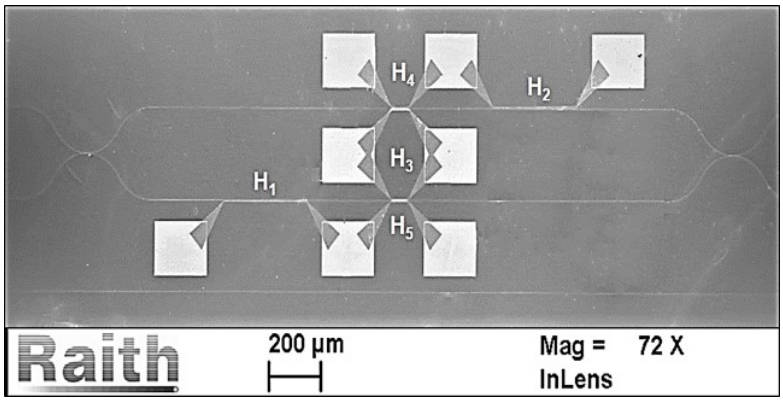

(a)

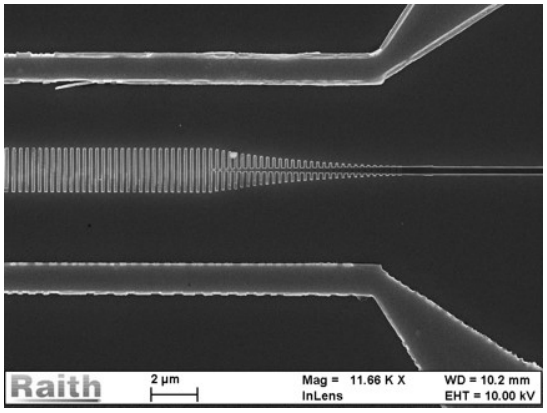

(b)

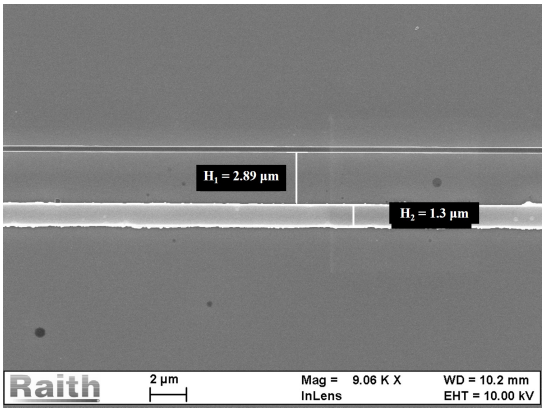

(c)

Figure 3.17: Zoomed SEM image of the (a) MZI region along with the fabricated microheaters, (b) SWG waveguide region with metal microheaters on either sides and (c) rib waveguide with the adjacent metal microheater.

either sides is shown in Figure 3.17(b). Zoomed-in view of the rib waveguide with the adjacent metal microheater is shown in Figure 3.17(c). The measured gap between the microheater and the rib waveguide is approximately 2.9 μm. Table 3.8 draws a comparison between the designed and experimentally obtained microheater parameters.

The average line resistance of fabricated microheaters is measured as $r_H \sim 27$ Ω/μm and the total resistance in both side flaring regions is $R_{FH} \sim 1.3$ kΩ (including probe contact resistance); these values are highly sensitive to thickness and quality

Table 3.8: Comparison of fabricated and designed device dimensions

Parameter	Designed	Measured
W_H	1.5 μm	1.4 $\pm$ 0.2 μm
t_H	100 nm	80-90 nm
G_H	3 μm	2.9 $\pm$ 0.1 μm

of deposited Ti thin film. For thermo-optic tuning, individual microheaters are probed with a current source meter unit (SMU). Since our microheaters are long (H_1, H_2 = 400 μm and H_3, H_4, H_5 = 100 μm), the differential temperature required for π phase-shift does not exceed 11K (44K) for L_H = 400 μm (100 μm). The electrical power consumption by a microheater (P_E) can be estimated for a current I_H flowing through it is: $P_E = I_H^2(r_H L_H + R_{FH})$.

3.2.2 Thermo-optic characterization set-up

A schematic illustration of the thermo-optic characterization set-up used to do the passive as well as active device characterization is shown in Figure 3.18(a). A four probe set-up was used: two fiber optic probes for input to output light coupling via grating couplers; and two electrical probes for driving the microheaters. x-y-z micropositioners are used for traversing and precisely positioning the fiber and electrical probes over the sample. The experimental set-up is equipped with a high resolution APEX 2043-B optical spectrum analyzer (OSA) with a minimum resolution bandwidth of 0.04 pm and in-built broadband tunable laser source with a power of 125 μW over wavelength range 1520 nm $\leq \lambda \leq$ 1630 nm. The device is held firmly on a sample holder using a vacuum pump. Fiber-optic output from the laser source excites TE-polarized guided mode at the input of the device under test via grating couplers. Transmitted output is collected again with a standard single-mode fiber via output grating couplers. The input and output single mode fibers are aligned at 10° vertically to the GCs for maximum coupling efficiency [124]. The electrical probes from the contact pads are connected to a source measure unit (Keithly). For transient characteristics measurement, a square wave signal from a function generator is used to modulate the output of the SMU. The optical output is then detected using a photodetector (Thorlabs, PDA10CS InGaAs) and sent to a digital storage oscilloscope (Keysight-DS). The entire

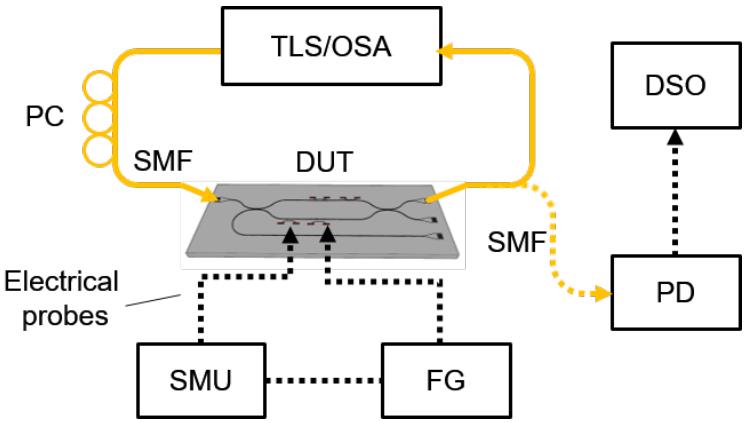

(a)

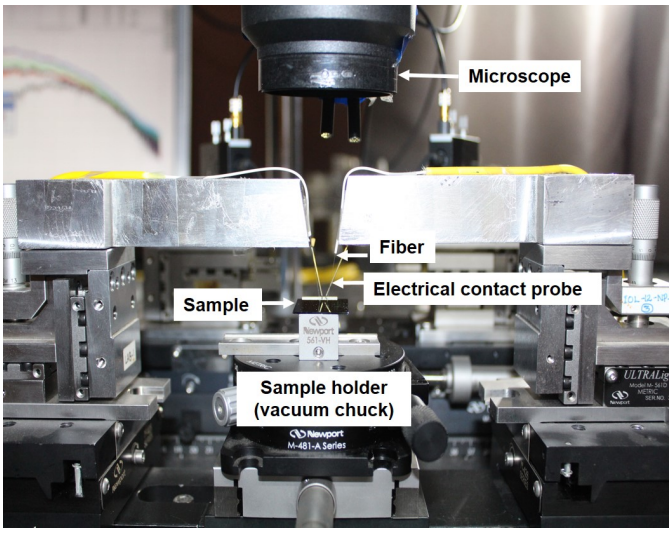

(b)

Figure 3.18: (a) A schematic illustration of the experimental set-up used for device characterizations: TLS -Tunable Laser Source, OSA - Optical Spectrum Analyzer, SMF - Single Mode Fiber, PC - Polarization Controller, DUT - Device Under Test, SMU - Source Measurement Unit, FG - Function Generator, PD - Photodetector, DSO - Digital storage oscilloscope); and (b) photograph of the electrical and fiber-optic probe station used for device characterizations.

set-up is controlled using LabVIEW programs. A photograph of electrical-cum fiber-optic probe station used for device characterizations is shown in Figure 3.18(b). The characterization results of the fabricated devices S_1 and S_2 have been discussed below in two sub-sections.

3.2.3 Passive Filter Characteristics

The passive characteristics were studied using sample S_1 which consisted of the set of devices listed in Table 3.3. Only 6 sets out of the 12 sets ($D_{1\#}$ - $D_{6\#}$) were having less insertion loss as the remaining 6 sets ($D_{7\#}$ - $D_{12\#}$) were very lossy due to over-dose issues while patterning. In this section, we will discuss the experimental results of some of the best devices we had obtained. The measured transmission response of a fabricated reference rib waveguide (D_{11}) along with a reference SWG waveguide of Λ = 285 nm adiabatically integrated with rib waveguide of same length (D_{12}) is shown in Figure 3.19. Since the rib waveguides were designed for single-mode guidance (TE-

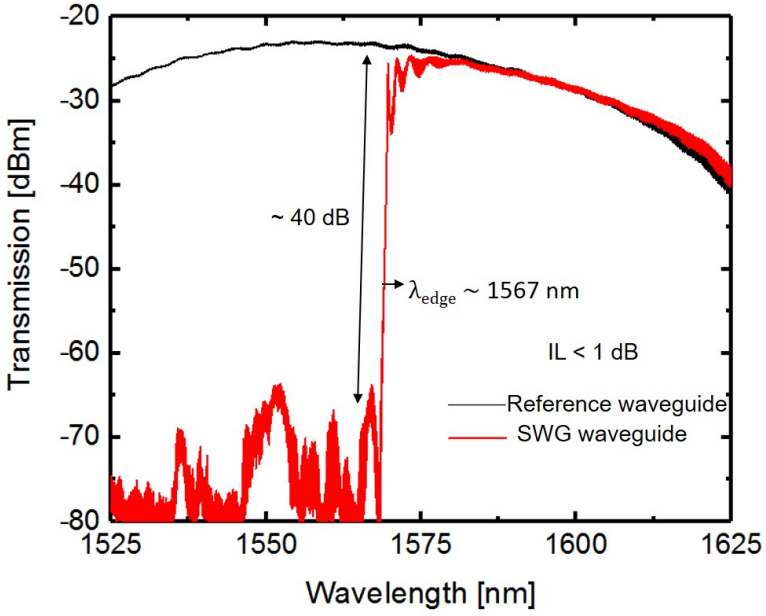

Figure 3.19: Passband transmission characteristics of SWG waveguide (Λ = 285 nm) (D_{12}) along with transmission of a reference rib waveguide (D_{11}).

polarization) for entire S+C+L bands and beyond, the observed wavelength dependent transmission characteristics for reference rib waveguide is due to the bandwidth limitation of input/output grating couplers [145]. The grating couplers were characterized with an average coupling loss of $\sim$ 6 dB (coupling loss/facet). The red curve shows the passband of SWG integrated waveguide which is exactly following the grating coupler transmission characteristics. The stop-band and pass-band of SWG waveguide is clearly evident in D_{12} with a sharp band-edge at $\lambda \sim$ 1567 nm. As expected, the extinction exceeds well above 35-dB. It must be noted that there is no significant excess loss for the pass-band of SWG waveguide when compared with the transmission of ref-

erence rib waveguide, < 1 dB. The measured edge roll-off for D_{12} is > 70 dB/nm. For

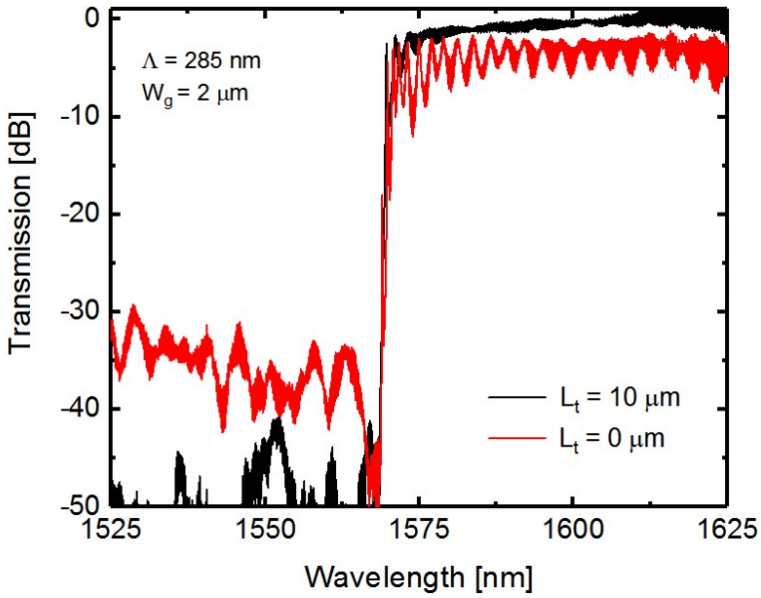

Figure 3.20: Passband transmission characteristics of SWG waveguide (Λ = 285 nm) (D_{12}) with and without adiabatic tapers at the SWG waveguide interfaces.

comparing the efficiency of the adiabatic taper used in the SWG waveguide, we had also fabricated a SWG waveguide with abrupt termination at either sides. Figure 3.20 shows the passband transmission characteristics of both the cases. It can be clearly seen that the SWG waveguide without any spot-size converter (red curve) suffers from significant mode mismatch loss ($\sim$ 5 dB insertion loss) and ripples in the passband ($\sim$ 8 dB). Also, there is a 20 dB improvement in the stopband suppression of SWG waveguide integrated with adiabatic tapers. The robustness and fabrication tolerance of the fabricated SWG waveguides were evaluated by measuring the transmission characteristics of SWG waveguides of five sets (D_{12}-D_{52}) with same design parameters and integrated with rib waveguides of same length as shown in Figure 3.21. The stopband extinction at the output of all SWG waveguides are found to be exceeding 35 dB. As expected from the simulation results, the experimental values obtained for λ_{edge} are 1569 $\pm$1 nm (see inset of Figure 3.21). This variation is mainly due to the variation in δ from device to device, which was around 0.5 $\pm$ 0.03. The normalized transmission characteristics (with respect to rib waveguide transmission) of a fabricated SWG waveguide with Λ = 275 nm has been compared with one of the above mentioned SWG waveguides with Λ = 285 nm as shown in Figure 3.22. The observed band-edge shift of $\Delta\lambda_{edge} \sim 37$ nm is again closely agreeing to simulation results ($\sim$38 nm) discussed earlier corre-

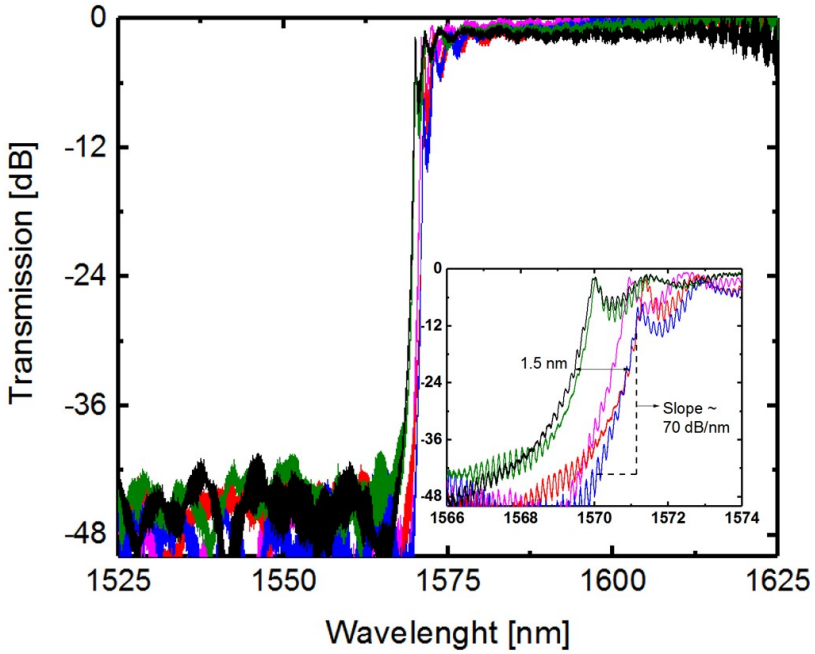

Figure 3.21: Normalized passband transmission characteristics of SWG waveguides from five different sets (D_{12} - D_{52}) with same design parameters (Λ = 285 nm). Inset shows the variation in the band-edge wavelength from device to device. The measured edge roll-off is $>$ 70 dB/nm.

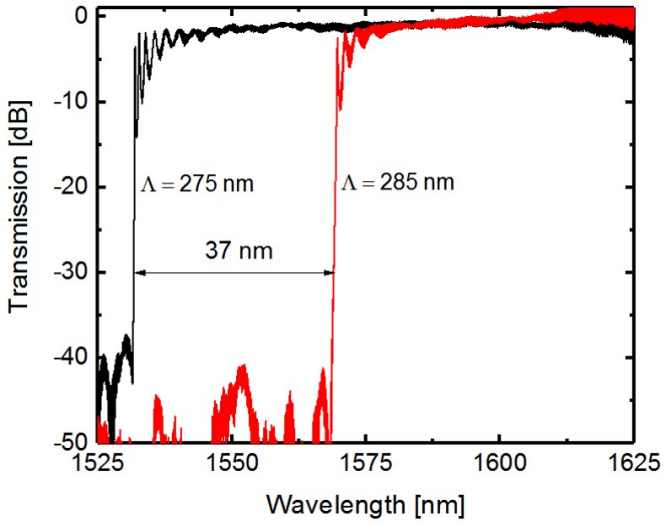

Figure 3.22: Measured wavelength dependent transmission characteristics of two SWG waveguides with Λ = 275 nm and 285 nm, respectively.

sponding to same differential periodicity of $\Delta\Lambda$ = 10 nm. The wavelength independent transfer function of the reference MZI device (D_{33}) has been shown in Figure 3.23 for both bar and cross ports. The result ensures the wavelength independent 3-dB power splitting of fabricated directional couplers. The measured excess loss is typically $<$ 2.4 dB. Finally, the normalized transmission characteristics of the proposed add-drop

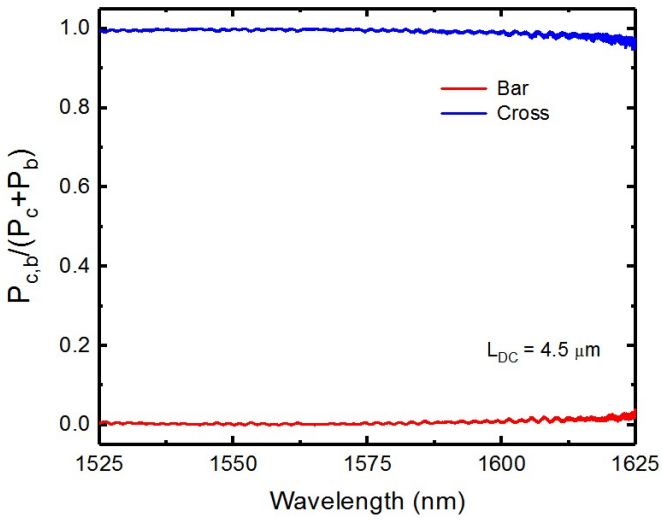

Figure 3.23: Normalized transmission characteristics of a reference wavelength independent MZI with balanced arm (D_{33}).

filter (D_{34}) is shown in Figure 3.24. All the add-drop filter devices were fabricated with SWG waveguides parameters as Λ = 285 nm, $\delta \sim 0.5$ and L_{swg} = 90 μm. The input

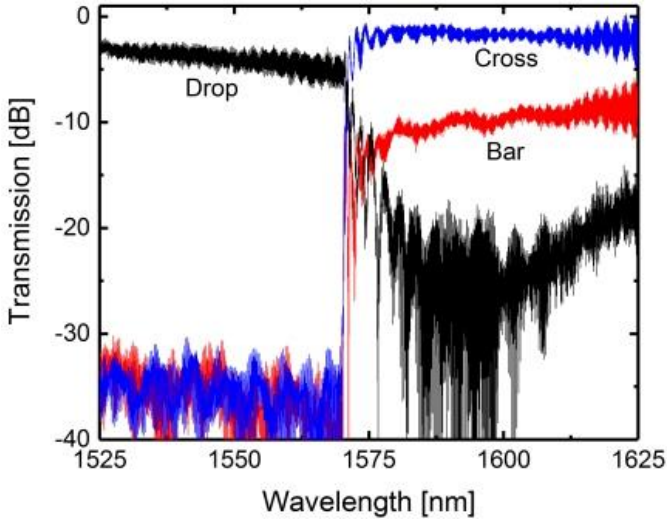

Figure 3.24: Transmission characteristics of fabricated add-drop filter (D_{34}) at cross port, bar port and drop port, respectively; each transmission is normalized with the transmission characteristics of straight reference waveguides.

laser light of $\lambda \gtrsim 1565$ nm appears at the cross port and $\lambda \lesssim 1565$ nm appears at the drop port with nearly flat-top responses. The normalized pass-band transmission in bar port exhibits $>$ 7 dB extinction as compared to cross port transmission. The insertion loss in the cross port is about 1.5 dB which is nearly uniform over the entire passband, whereas the insertion loss at the drop port is exceeding 3-dB which can be attributed to additional 180^o bend waveguide loss. Nevertheless, the 3-dB bandwidths of the spec-

tral responses in the stopband and passband exceeds 40 nm. While we observe all the fabricated filter devices to exhibit $\lambda_{edge} \sim 1565$ nm and stopband extinction exceeding 35 dB (same as SWG waveguides discussed earlier), the band extinction in any of the output ports is highly sensitive to undesirable phase mismatch between two arms of the MZI. The filter characteristics of some of the fabricated devices shown in the Figure

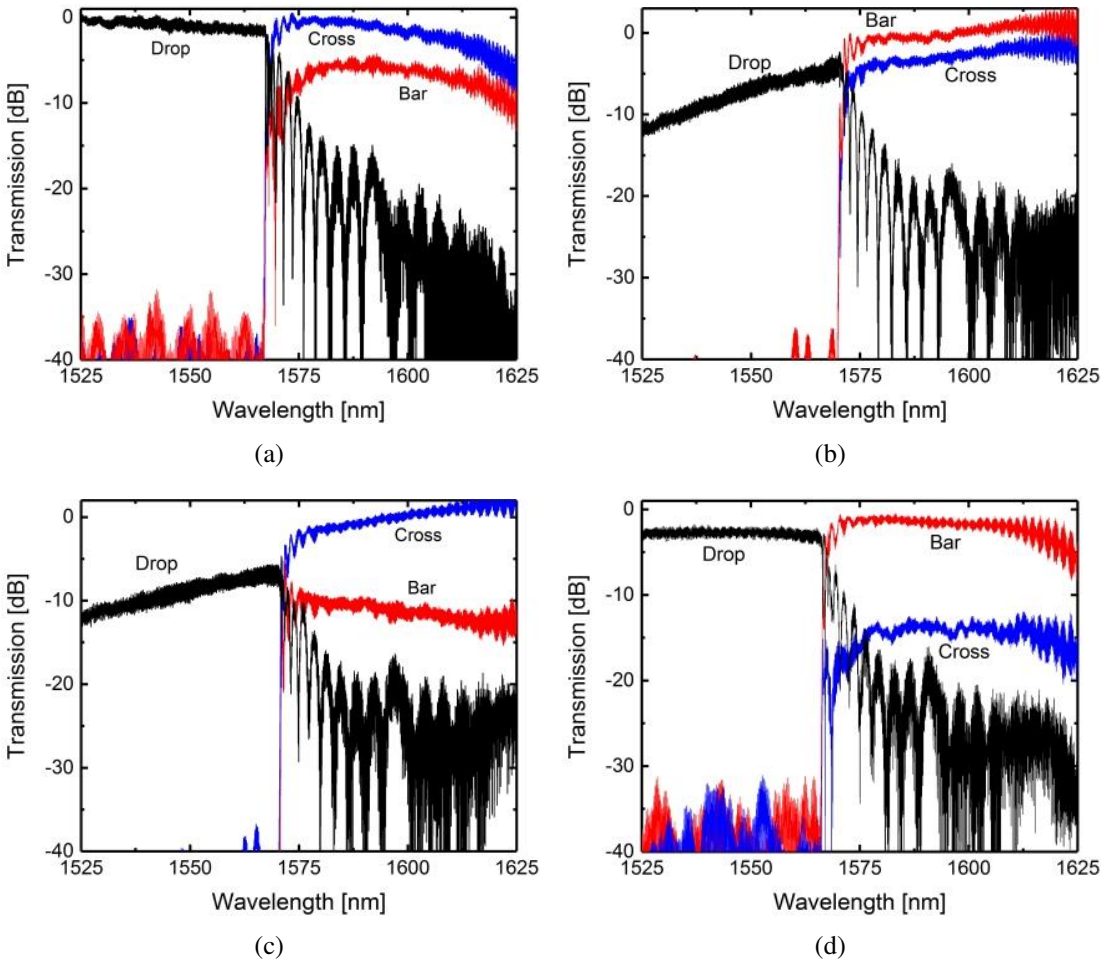

Figure 3.25: Transmission characteristics of the add-drop filters at cross port, bar port and drop port respectively with phase mismatch in the MZI arms; (a) Device D_{24}, (b) D_{44}, (c) D_{54} and (d) D_{64}. Each transmission is normalized with the transmission characteristics of a straight reference waveguide.

3.25 prove that the insertion losses at the cross port, the bar port and the drop ports vary significantly from device to device. For example, while the power appearing at the cross-port is more than that in the bar port for devices D_{24} (Figure 3.25(a)) and D_{54} (Figure 3.25(c)), the bar port sees higher power output for the devices D_{44} (Figure 3.25(b)) and D_{64} (Figure 3.25(d)). The SWG passband in the device D_{64} (Figure 3.25(d)) eventually appears at the bar port with more than 12 dB extinction at the cross

port. At the same time, we see that SWG stopband reflected back into drop port with uniform insertion loss $\sim$ 2.5 dB (nearly same as WIDC losses for two passings). These results clearly indicate that there is a phase mismatch of about π between the MZI arms only for passband (i.e.,$\sim$ π phase difference due to the asymmetry in waveguides on the right side of SWGs in MZI arms). Apart from the insertion loss difference in all the output ports, the filter responses shown in Figure 3.25(a) and 3.25(b) are highly wavelength dependent. This indicates that the WIDCs acting as 3-dB power splitters are not exactly wavelength independent. All these errors are introduced due to fabrication

Table 3.9: Deviation in the experimentally measured results from device to device

Parameter	Value
Band-edge position (λ_{edge})	1565 nm $\pm$ 2 nm
Band-edge extinction (ER)	35 $\pm$ 5 dB
Cross port to bar port (vice-versa) extinction (ER_{bc})	0 dB - 15 dB

process uncertainties. Table 3.9 gives an overview on the deviations in the experimentally measured results from device to device. The phase-mismatch issues in the MZI can be mitigated by integrating microheaters at different locations in the MZI arms as discussed in the next section.

3.2.4 Thermo-Optic Tuning/Switching

For thermo-optic tuning and/or switching experiments, sample S_2 was fabricated wherein the add-drop filter devices were integrated with microheaters at different locations as shown in Figure 3.1. We had fabricated a set of 12 devices with each set containing the devices listed in Table 3.3. We had observed that the λ_{edge} values of the SWG waveguides in S_2 were matching with that of the ones in S_2 (1569 $\pm$ 2 nm). For the detailed discussions on how different microheaters impact the filter response, we will be taking forward only one of the devices (D_{H33}) for which the normalized passive filter characteristics at cross-, bar- and drop ports are as given in Figure 3.26. In this particular device, it can be seen that the bar port as well as the cross port have same extend of passband power level with insertion loss of about 4-dB each. The SWG stopband at the drop port is about 10-dB down from the bar/cross port response level in the passband. Since the SWG and WIDC designs are relatively robust and fabrication tolerant, it is

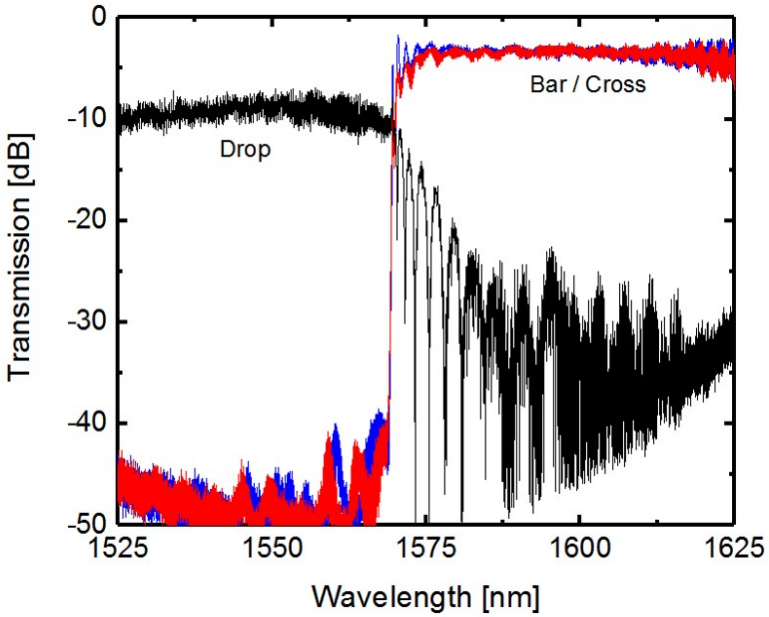

Figure 3.26: Passive transmission characteristics of D_{H33} (normalized to the transmission of a reference straight waveguide) at cross-, bar- and drop ports

highly possible that the undesirable power levels in all three output ports are most likely due to phase mismatch between MZI arms. In the rest of this section, we will discuss how each microheater aids in tuning/switching the add-drop filter response.

H_1 microheater

We carried out a thermo-optic tuning by the microheater H_1 (see Figure 3.1) which can simultaneously influence transmission at all the three output ports. Figs. 3.27(a) and 3.27(b) are the transmissions at three output ports corresponding to two different optimum switching states, respectively. The passband transmission is maximized at bar port and stopband is maximized at the drop port simultaneously for an electrical power consumption (by H_1) of P_{H1} = 18 mW (as in Figure 3.27(a)). By further increasing the electrical power dissipation to $\sim$ 72 mW at the same microheater H_1, the passband transmission is maximized at cross port and stopband is maximized again at the drop port simultaneously (as in Figure 3.27(b). This observation is due to the position of microheater H_1 in the MZI circuit; the power required for one cycle of stopband switching between drop port and input port is same as that of half-cycle switching of passband between bar port and cross port. Thus the estimated switching power (for π phase-shift) for microheater H_1 is $\sim$ 54 mW. This has been reconfirmed by recording transmissions at three different outputs as a function of electrical power dissipated by H_1 (see Figure

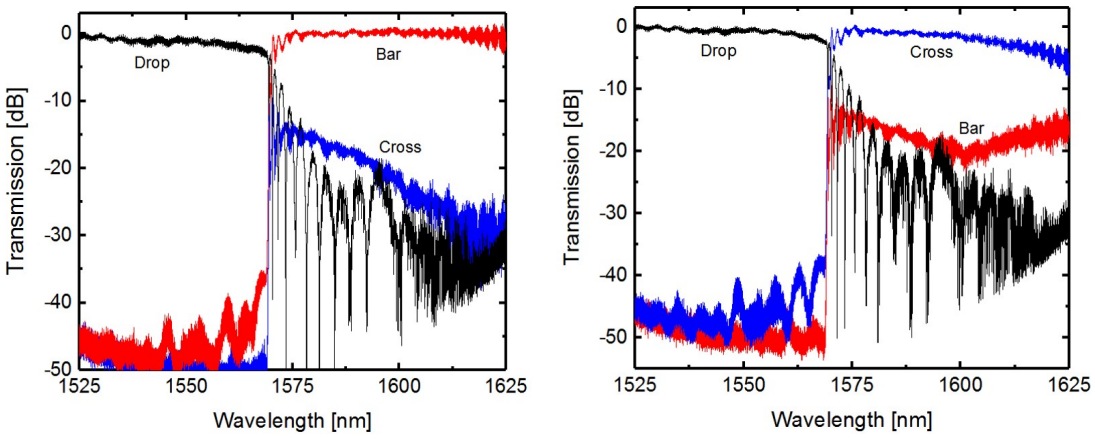

Figure 3.27: Thermo-optic switching characteristics of a fabricated device D_{H33}: (a) passband transmission maximized at the bar port and simultaneously stopband transmission maximized at the drop port using microheater H_1; and (b) passband transmission maximized at the cross port and simultaneously stopband transmission maximized at the drop port using microheater H_1.

3.28). The dotted lines show the corresponding theoretical fit of the transmissions (in

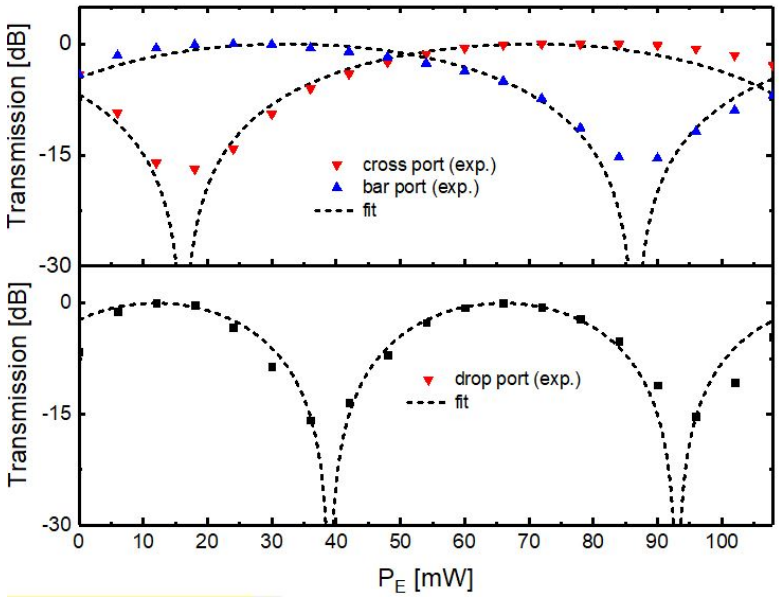

Figure 3.28: Transmission at bar/cross ports (at λ = 1572 nm) and drop port (at λ = 1550 nm) of device D_{H33} as a function of electrical power dissipated by the microheater H_1 (P_E). Dotted lines correspond to the theoretical fit using Eqns.3.9, 3.10, 3.11 and 3.5.

dB scale) at bar-, cross-, and drop ports of the MZI as given by following expressions:

$$P_{bar} = P_b.sin^2(\Delta\Phi/2 + \zeta_1) \tag{3.9}$$

$$P_{cross} = P_c.cos^2(\Delta\Phi/2 + \zeta_1) \tag{3.10}$$

$$P_{drop} = P_d.cos^2(\Delta\Phi + \zeta_2) \tag{3.11}$$

where $P_{b,c,d}$ are normalized peak transmission (with respect to a reference waveguide) at bar-, cross-, and drop ports, respectively; and fitting parameters $\zeta_{1,2}$ are accounted for the phase-mismatches between interfering waves at bar-/cross-ports and drop-port, respectively, which may occur due to fabrication imperfections. The experimental results are fitted with the theoretical expressions given by Eqns. 3.9, 3.10, 3.11 and 3.5. Thus the sensitivity of the fabricated waveguide microheater is extracted as S_H^{rib} = 79K-μm/mW (along with $\zeta_1 = 0.33\pi$ rads and $\zeta_2 = 0.75\pi$ rads). This value is slightly higher than that of COMSOL Multiphysics calculations ($\sim$ 65K-μm/mW), which may be attributed to the change in microheater proximity to the rib waveguide of our fabricated devices.

H_2 microheater

The passband switching between cross- and bar ports without affecting the drop port transmission is carried out by thermo-optic tuning of microheater H_2; corresponding transmission characteristics at different electrical power levels at H_2 have been shown in Figures 3.29(a) and 3.29(b), respectively. The results indicate a switching power of $P_\pi \sim$ 54 mW the power required to switch the pass-band maxima from bar port to cross-port or vice-versa), same as that of microheater H_1 which is expected because of their identical lengths L_H = 400 μm. These results have been replotted in Figure 3.30 to better understand the change in P_{bar} and P_{cross} with respect to P_E. When P_E = 0 mW, both P_{bar} and P_{cross} are at the same power level. When P_E is increased to 20 mW, P_{cross} becomes maximum while P_{bar} becomes minimum. On further increasing P_E, P_{cross} (P_{bar}) starts to decrease (increase) sinusoidally and reaches a minima (maximum) at P_E = 75 mW. The maximum extinction ratio measured for the demonstrated devices is limited to 20 dB due to unequal splitting ratio of directional couplers. Also, the cross/bar port transmission characteristics exhibit ripples of about $\pm$ 0.5 dB, whereas for drop port it is about $\pm$ 1 dB. Such ripples may be attributed to power fluctuations in the light source as well as the detection sensitivity of the optical spectrum analyzer used in experimental setup.

H_3 microheater

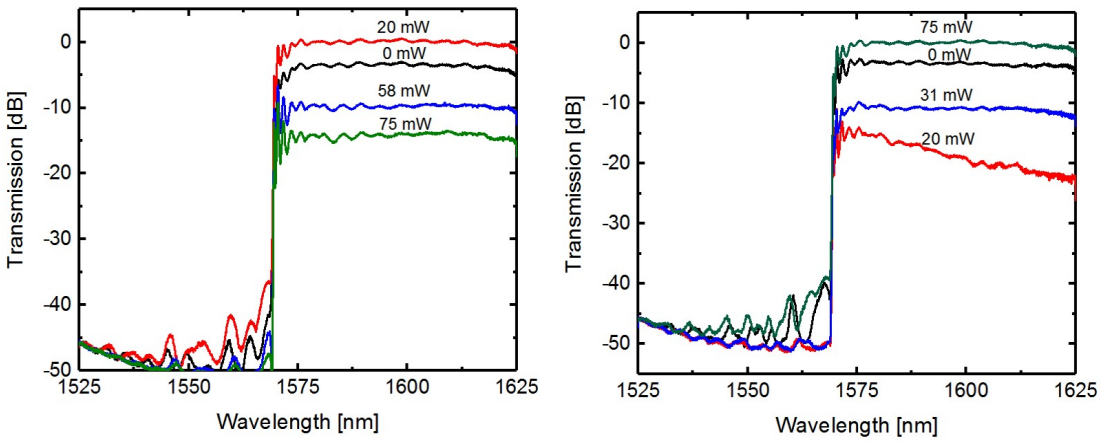

(a) (b)

Figure 3.29: Thermo-optic switching of the passband between the cross port and the bar port without affecting the drop-port: (a) passband transmissions at the cross port for different electrical power levels consumed by microheater H_2; and (b) passband transmissions at the bar port for different electrical power levels consumed by microheater H_2 (Device : D_{H33}).

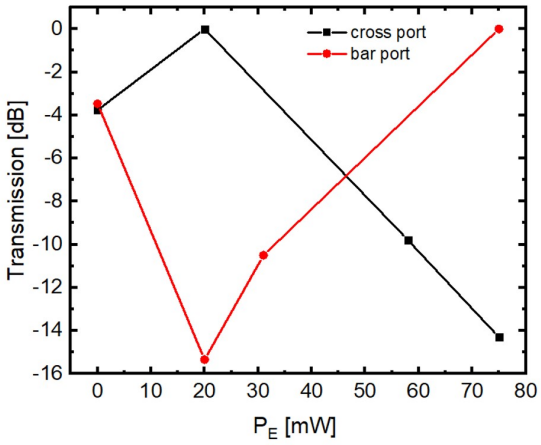

Figure 3.30: Transmission at bar/cross ports (at λ = 1572 nm) of device D_{H33} as a function of electrical power dissipated by the microheater H_2 (P_E).

Finally, the microheater H_3 (L_H = 100 μm) is used for thermo-optic tuning of band-edge λ_{edge}. Fig 3.31(a) shows the band edge detuned transmission characteristics at the cross port for different power levels in H_3. We could red-shift the band-edge up to $\sim$2.5 nm for an applied power of $\sim$ 112 mW. Thus we observe a thermo-optic tuning efficiency of $\sim$ 22 pm/mW. It is interesting to note that there is no much variation in the insertion loss and the flat-top pass-band is well preserved. Figure 3.31(b) shows the band edge shift ($\Delta\lambda$) as a function of applied electrical power. It can be observed that the wavelength shift is linear to the power consumed by microheater H_3. The only

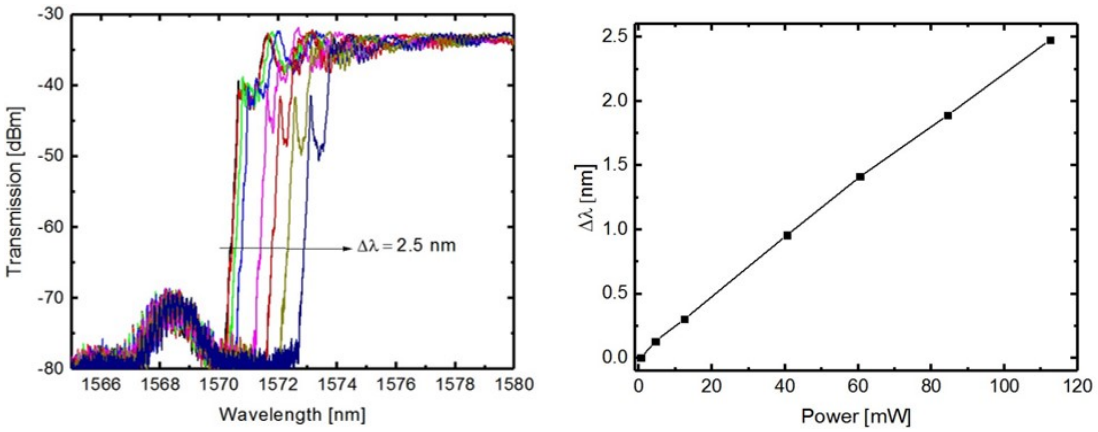

(a) (b)

Figure 3.31: (a) Transmission spectra showing the band-edge tuning of the device with respect to dissipated power in microheater H_3; (b) band-edge detuning as a function of dissipated power in microheater H_3 (Device : D_{H33}).

limitation to the tunability of the band-edge is the breakdown current of the microheater H_3. Figure 3.32 shows the SEM image of a microheater adjacent to the SWG waveguide which was heated beyond its breakdown limit thus resulting in the malfunctioning of the microheater.

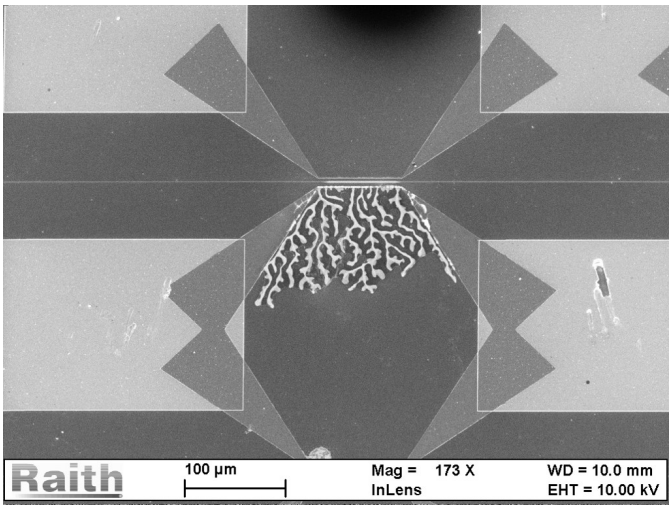

Figure 3.32: SEM image of a burnt metal microheater which was driven beyond its breakdown point.

H_4 and H_5 microheater

The auxiliary microheaters H_4 and H_5 were not utilized for this device as the band-edge observed at cross- or bar ports of the MZI is found to be as good as the transmission characteristics of isolated SWG waveguides, except a band-edge shift of about 5 nm

($\lambda_{edge} \sim$ 1570 nm).

3.2.5 Transient characteristics

We have studied the transient response of the device D_{H33} at three output ports using microheater H_3 and by launching laser light operating at little higher than the band-edge (λ = 1571 nm) but not completely falling in the flat-top passband region. A 12

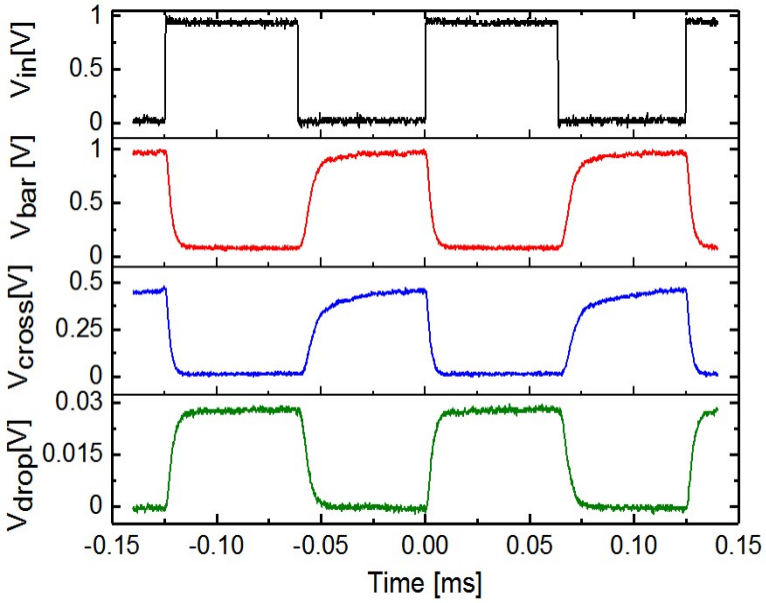

Figure 3.33: Simultaneous thermo-optically modulated light output powers in arbitrary units (measured by a photodiode) at bar-, cross-, and drop ports for an input laser light operating at λ = 1571 nm (slightly above λ_{edge}): (a) square pulse electrical signal (at 12 kHz) applied to the microheater H_3; (b) bar port; (c) cross port; and (d) drop port (Device : D_{H33}).

kHz square wave of amplitude 2.8 V was applied from a function generator to drive the microheater H_3 and the time-domain optical response in all the three output ports were collected using a photodetector (THORLABS PDA10CS InGaAs photodetector) and recorded in a digital storage oscilloscope. They are shown in Figure 3.33; exhibiting an average rise time of $\sim$5 μs and fall time of $\sim$4 μs. The modulation of applied electrical power to microheater H_3 results into a red-shift modulation of band-edge. The bar port and the cross port follow the same transient characteristics, whereas the drop port response is complimentary to the bar/cross port transient response. Thus the device is capable of converting electrical signal into optical signal in triplicate. Thus if the

microheater H_3 is replaced by a high-speed p-n junction diode, then it can be used as a high-speed optical modulator with two identical signal stream and one complimentary signal stream at three different output ports.

3.3 Summary

In summary, an ultra broadband add-drop filter/switch circuit is designed and demonstrated in SOI substrate. The integrated optical circuit is basically a 2×2 balanced MZI designed by cascading two wavelength independent directional couplers acting as 3-dB power splitters. Two identical SWG waveguides are adiabatically integrated in two arms of the MZI. They are designed to operate in TE-polarization with a well defined band-edge wavelength $\lambda_{edge} \sim 1565$ nm (roll-off > 70 dB/nm) dividing its fundamental stopband ($\lambda < \lambda_{edge}$) and guiding passband ($\lambda > \lambda_{edge}$). The stopband and passband of the SWG could be filtered efficiently at the drop port and cross/bar port of the MZI, respectively. Table 3.10 draws a comparison of the demonstrated add-drop filter with the

Table 3.10: Comparison with recently demonstrated devices (MZI with Bragg gratings)

Literature	ER (dB)	BW (nm)	Insertion loss (dB)	
			Drop port	Bar port
Wang et. al.[146]	40	5	5	13
Saber et. al. [140]	25	7	2	4.2
This work	35	40	2	2

recent demonstrated devices in literature. It is clear that the broadband SWG add-drop filter demonstrated by us is relatively superior to the existing technologies in terms of reflection bandwidth and insertion loss. Five different microheaters are also integrated at different locations of the MZI for phase correction and switching applications. The band-edge wavelength could be thermo-optically tuned with a slope efficiency of 22 pm/mW. The passband switching between bar- and cross port is demonstrated with more than 15 dB extinction; measured switching power $P_\pi \sim 54$ mW. Thermo-optic modulation is also demonstrated simultaneously at cross-, bar- and drop ports for an operating wavelength λ = 1571 nm (slightly above λ_{edge}). The rise-time and fall-time in thermo-optic modulation is recorded as $\sim$5 μs and $\sim$4 μs, respectively. The lower switching time could be accomplished because of the integration of microheater directly

on the silicon slab (in contrast to the conventional microheater integrated over the top cladding oxide). In future, this thermo-optic microheater can be replaced by a p-n junction waveguide for high-speed switching and perhaps for high-speed modulator circuit. Moreover, the optical insertion loss of the device can be reduced by introducing deeply etched access waveguide bends [142] and switching power, P_{π} (microheater sensitivity, S_H) can also be reduced (increased) by trench isolation and may be with an improved design of microheater (e.g., meander configuration).

CHAPTER 4

Linear-edge Filter

In the previous chapter, we discussed about the design and demonstration of on-chip broadband filters using SWG waveguides. While these filters exhibit significant out-of-band suppression ($>$ 35 dB), a major shortcoming is the lack of a smooth band-edge and the existence of significant side-lobes/ripples in the reflection and transmission spectra. The recent advancements in integrated silicon photonics call for the need of broadband (both stopband and passband) and high-extinction filters with a linear and smooth edge roll-off; especially in non-linear optical and microwave photonic signal processing either for residual pump rejection or for unwanted side-band suppression [147, 148]. A suitably designed edge filter with a linear roll-off can also be potentially used in lab-on-chip optical sensors where a wavelength-encoded measurement can be translated to a cost-effective readout mechanism similar to earlier demonstrations using fiber optics [149]. A recent demonstration of a rectangular edge filter using a multi-moded asymmetric side-wall grating reported an edge-extinction of $>$ 40 dB at the rate of 118 dB/nm [128]. But, it also had significant side-lobes and ripples in the transmission spectra.

The side-lobe amplitudes and the rolloff-slope characteristics of a filter depend upon the form of the perturbation-amplitude envelope κ(z) [150]. By appropriately choosing a κ(z) envelope, one can reduce the sidelobe level by several orders of magnitude while maintaining high peak reflectivity without degrading the roll-off rate. Thus, the shape of the reflection spectrum depends on S_κ and the shape of the function κ(z). Adopting the 'window' function concept from traditional digital filter theory, Cross et al.[151] established that the reflection spectrum of a grating reduces to the Fourier transform of the perturbation-amplitude envelope $\kappa(z)$ along the length of the grating. Thus, a suitable κ(z) function which has low-transform sidelobes are favorable candidates to produce filters with low-reflection sidelobes. Various apodization techniques have been explored for κ along the grating length to remove side-lobes and thereby smoothen edge roll-off in filtering characteristics [152, 153, 154, 155]. However, all these demonstrations are

focused on DBR structures (weaker perturbations) and hence aim at smoothening the edges of narrow-band notch filter responses (bandwidth < 10 nm).

In [155], apodized sidewall gratings in SOI rib waveguides was first demonstrated to reduce the side-lobe levels in the transmission spectra. The apodization was achieved by linearly increasing the sidewall grating width towards the center of the waveguide. It was proved that a linear variation in sidewall grating width gives rise to a raised cosine apodization of κ thus resulting in a filter response with minimal side-lobes. Though this technique of width tapering is relatively more fabrication friendly with standard lithography techniques, the devices were mostly designed for narrow-band applications.

In this chapter, we present a robust design and demonstration of a compact apodized SWG waveguide in SOI substrates for broadband applications. We use the linear apodization technique of the grating so as to obtain raised cosine $\kappa(z)$ apodization. The filter exhibits a ripple-free broad passband followed by a linearly rolled-off, highly extinguished ultra-broad stop-band around the Bragg wavelength.

4.1 SWG waveguide design

Fig. 4.1 shows the schematic illustration of the proposed integrated optical SWG-based device to be realized in the 220-nm SOI platform (with the buried oxide (BOX) layer of 2 μm) for the demonstration of the desired edge-filter characteristics operating in the optical C+L bands. The desired apodization is achieved by linearly modulating the

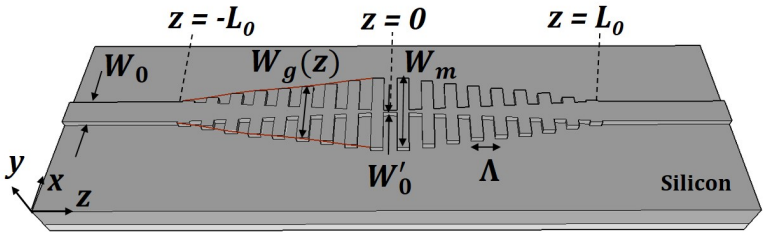

Figure 4.1: Schematic 3-D view of the apodized SWG waveguide along with the input/output access waveguides

SWG waveguide width $W_g(z_i)$ and the rib width $W_0(z_i)$ towards the center (from both

sides) given by the following expressions:

$$W_g(z_i) = W_0 + \frac{W_m - W_0}{L_0}(L_0 - |z_i|) \tag{4.1}$$

$$W_0(z_i) = W_0' + \frac{W_0 - W_0'}{L_0}|z_i| \tag{4.2}$$

where $z_i = z_{i-1} + \Lambda$ ($i = 1, 2, 3, ...N; L_g = 2N\Lambda$), W_m and W_0' are the widths of the grating and rib waveguide at the center respectively, W_0 is the width of the access waveguides and $2L_0 = L_g$ is the total length of the SWG waveguide. The period Λ and the duty cycle δ may be maintained constant throughout the length of the device to keep the design as simple as possible. The width-dependent average effective index $n_{eff}(z_i)$ and the coupling strength $\kappa(z_i)$ of the i^{th} cell for a particular wavelength in the stop-band can be estimated using Effective Medium Theory (EMT) and Lumerical 2D MODE Solutions. Initially, the shallow-etched SWG layer is treated as a homogeneous waveguide medium with the weighted average refractive index estimated using EMT for transverse electric (TE) polarization operating at λ (wavelength in free space) given by [72]:

$$n_{||}(z_i, \lambda) = [f_A(z_i)n_{Si}^2(\lambda) + \{1 - f_A(z_i)\}n_{air}^2(\lambda)]^{1/2} \tag{4.3}$$

where $f_A(z_i)$ is the fractional area occupied by silicon in the top grating layer of the i^{th} cell (see Fig. 4.2(a)). The effective index $n_{eff}(z_i, \lambda)$ of the guided mode is then

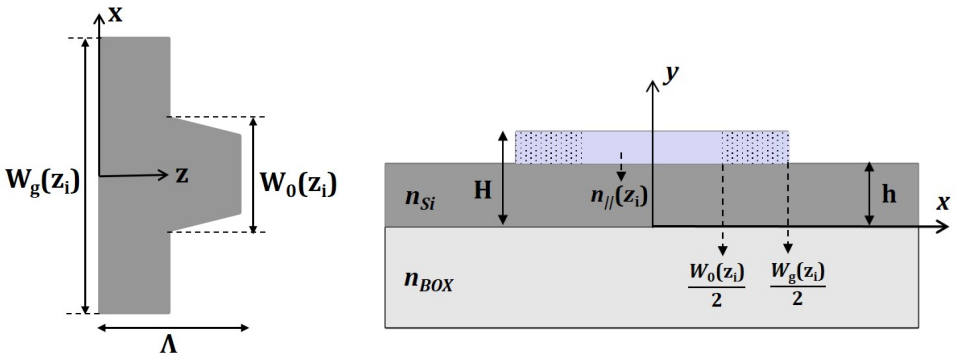

(a) (b)

Figure 4.2: (a) Top view of i^{th} cell of the grating showing width parameters $W_g(z_i)$ and $W_0(z_i)$; and (b) cross-sectional view of the equivalent rib waveguide of the i^{th} cell with refractive index estimated using effective medium theory.

evaluated for an optical equivalent waveguide with the rib or grating layer refractive

index of $n_{||}(z_i, \lambda)$ and the bottom silicon slab height h with $n_{si}(\lambda)$ as shown in Fig. 4.2(b), using Lumerical MODE Solutions. The wavelength-dependent refractive indices of bulk silicon and the BOX layer are considered according to Sellmeier's equations in this calculation. The calculated effective index $n_{eff}(z_i, \lambda)$ and locally normalized mode field distribution $\mathcal{E}(x, y, z_i, \lambda)$ of the i^{th} cell are then used to evaluate the backward coupling coefficient $\kappa(z_i, \lambda)$ for the guided fundamental mode as given by [156, 128]:

$$\kappa(z_i, \lambda) = \frac{n_{Si}^2(\lambda) - n_{air}^2(\lambda)}{n_{eff}(z_i, \lambda)} \left(\frac{2}{\lambda}\right) \Gamma(z_i, \lambda) \tag{4.4}$$

where $\Gamma(z_i, \lambda) = \int_{x_1}^{x_2} \int_{y_1}^{y_2} |\mathcal{E}(x, y, z_i, \lambda)|^2 dxdy$; $x_1 = \frac{W_0'(z_i)}{2}$; $x_2 = \frac{W_g(z_i)}{2}$; $y_1 = h$ and $y_2 = H$ (device layer thickness). We have studied two different apodization schemes with $W_0' = W_0 = 450$ nm and $W_0' = 100$ nm, respectively (keeping all other parameters unchanged) to compare the filter characteristics. The SWG waveguide is designed ($\Lambda = 285$ nm; duty cycle $\delta = 0.5$; $W_m = 2.5\ \mu m$) to transmit wavelengths above $\lambda_{edge} \sim 1550$ nm (Chapter-2). The etch depth of the SWG waveguides is kept unchanged (60 nm) as that of the access waveguides (rib width = 450 nm and slab height, $h = 160$ nm) to support the fundamental TE-polarized mode over a wavelength span $1525 < \lambda < 1625$ nm (C + L bands). We have considered $L_g = 2L_0 = 50\ \mu m$ in both the cases.

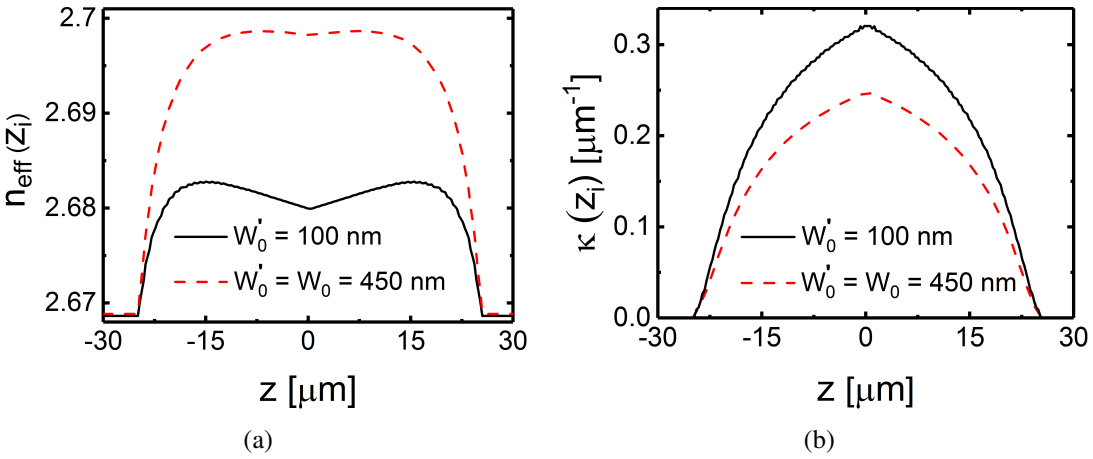

Figure 4.3: Comparison between two different apodized SWG waveguides with W_0' = 100 nm and 450 nm, respectively using EMT: (a) calculated $n_{eff}(z_i)$ profiles; and (b) calculated $\kappa(z_i)$ profiles. The calculations are carried out for TE polarization operating at λ = 1550 nm (L_g = 50 μm, W_m = 2.5 μm).

Figures 4.3(a) and 4.3(b) are showing the calculated $n_{eff}(z_i)$ and $\kappa(z_i, \lambda)$ along the length of the SWG waveguide calculated at λ = 1550 nm for two different values of W_0'

(100 nm and 450 nm). Thus the proposed apodization structure ensures smooth transitions of the effective index of the guided fundamental mode from the SWG waveguide to the input/output access waveguides. The transition is smoother and more adiabatic for W_0' = 100 nm ($< W_0$) compared to that of W_0' = 450 nm ($W_0' = W_0$). More importantly, the profiles of $\kappa(z)$ in both cases are closely resembling to a raised cosine window function which will eventually ensure filter responses with reduced side-lobes [155]. However, the magnitude of $\kappa(z)$ is higher for smaller values of W_0' ($< W_0$). Thus we have shown with numerical simulations that with a linear width apodization of a given SWG waveguide (keeping all other parameters fixed), one can easily obtain the desired apodization profile of κ to reduce the side-lobes of the Bragg stop-band. With the knowledge of $n_{eff}(z)$ and $\kappa(z)$ profiles of the device, one can approximately evaluate the center wavelength λ_{sb}^{c} of the stop-band (Bragg wavelength), its spectral width $\Delta\lambda_{sb}$ (stop-band) and the stop-band-to-passband extinction ratio (ER) for an apodized grating as [127]:

$$\lambda_{sb}^{c} \approx \left(\frac{\Lambda}{L_s}\right) S_g \tag{4.5}$$

$$\Delta\lambda_{sb} \approx \frac{1}{\pi}\left(\frac{\Lambda}{L_s}\right)^2 S_\kappa S_g \tag{4.6}$$

$$ER(\lambda \in \Delta\lambda_{sb}) = 10\log_{10}[1 - \tanh^2(S_\kappa)] \tag{4.7}$$

where we have introduced two parameters S_g (effective optical path length) and S_κ (effective backward coupling) given by:

$$S_g = \int_{-L_s}^{+L_s} n_{eff}(z, \lambda_{sb}^{c}) dz \tag{4.8}$$

$$S_\kappa = \int_{-L_s}^{+L_s} \kappa(z, \lambda_{sb}^{c}) dz \tag{4.9}$$

In the above equations, we assumed the effective length of the Bragg grating $L_B = 2L_s$ (which is smaller than the device length L_g) contributing to the Bragg reflection at λ_{sb}^{c}. For a given device length L_g, the value of L_B depends on its apodization profile (can be correlated with Fig. 4.3(a)). We have considered L_s as a fitting parameter which can be extracted either from numerical simulations or from experimental results for a given device of length (L_g) and apodization function. Thus it is clear from equations (4.5) - (4.7) and Fig. 4.3(a) that the parameter S_g can be engineered significantly by controlling

the value of W_0' alone. However, the minimum value of W_0' is fixed by the lithography resolution limit and process-related reproducibility. Also, S_κ is larger in the case of the device with W_0' = 100 nm leading to larger stop-bandwidth and out-of-band suppression. The detailed transmission and reflection characteristics of the proposed devices can be

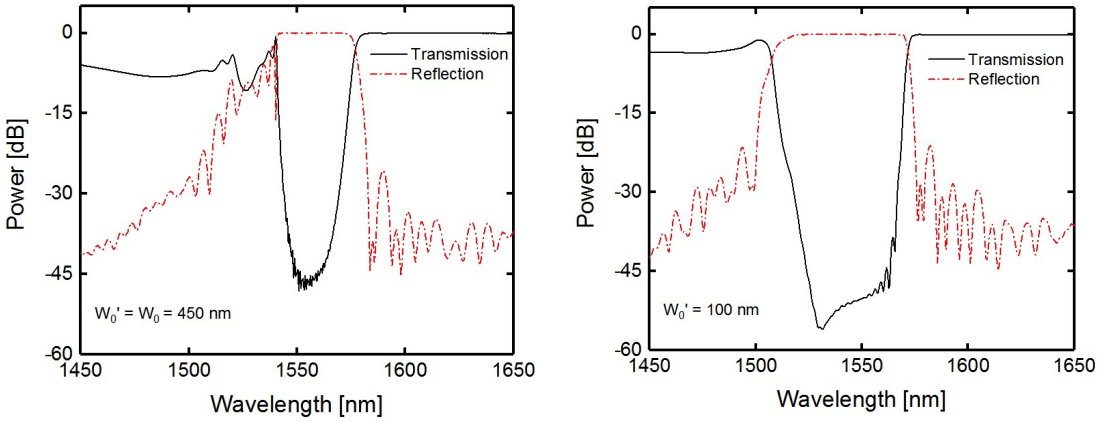

(b)

Figure 4.4: 3D-FDTD transmission (solid line) and reflection (dashed line) characteristics (for TE-polarization) of the device for (a) W_0' = W_0 = 450 nm and (b) W_0' = 100 nm; See text for other parameters.

computed more accurately using 3D-FDTD and the corresponding simulation results for W_0' = 450 nm and W_0' = 100 nm are shown in Figure 4.4(a) and 4.4(b) respectively. The reflection characteristics were obtained by placing a frequency monitor behind the mode source. The side-lobes are significantly suppressed in the transmission as well as reflection spectrum at the right (long-wavelength) edge of the stop-bands for both the device structures. However, side-lobes/ripples are still present at the left short-wavelength edges which are due to the positive slopes of the apodization functions [157]. Following the predictions from couple mode theory, the FDTD simulations also reveal that SWG waveguide with W_0' = 100 nm has broader and deeper stopband with linear band-edge roll-off due to higher value of $\kappa(z_i, \lambda)$. Again smaller value of W_0' results into stronger $\kappa(z)$ modulation. However, we have used W_0' = 100 nm for rest of our studies considering lithography limit and fabrication reproducibility in our labs. The extinction of the stopband can be enhanced by increasing the device length L_g without altering any other parameters. Figure 4.5(a) shows the transmission response of the apodized SWG waveguides of three different lengths (L_g = 30 μm, 50 μm and 70 μm) with W_m = 2.5 μm. The results clearly exhibit flat-top passbands for $\lambda > \lambda_{edge} \sim$ 1570

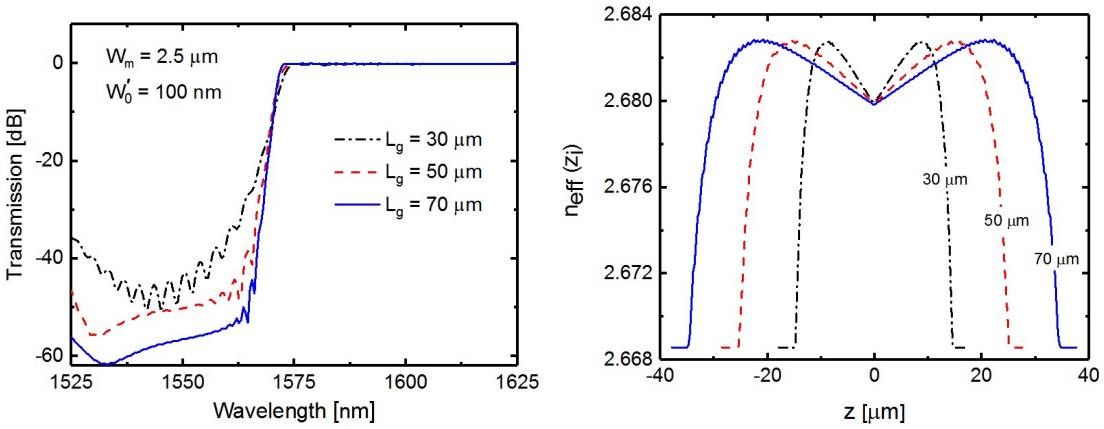

(b)

Figure 4.5: (a) 3D-FDTD transmission response and (b) calculated $n_{eff}(z_i)$ profiles (for TE-polarization) of the device with W_m=2.5 μm and W_0' = 100 nm for three different values of L_g. See text for other parameters.

nm with smooth edge roll-off. As expected, the longest device (L_g = 70 μm) exhibits the highest stopband extinction of $\sim$ 60 dB. However, the SWG passband edge wavelength λ_{edge} remains nearly same for all L_g values. This is due to the fact that the peak effective index of the device is independent of L_g when all other parameters remain unchanged. This is evident from the length dependent interpolated $n_{eff}(z_i)$ profiles shown in Figure 4.5(b). Even though the rate of change of n_{eff} becomes smaller with increase in L_g, the peak value of effective index and hence the pass-band edge remains unaltered. However, the slope of the band-edge becomes steeper with increasing L_g. The desired value of

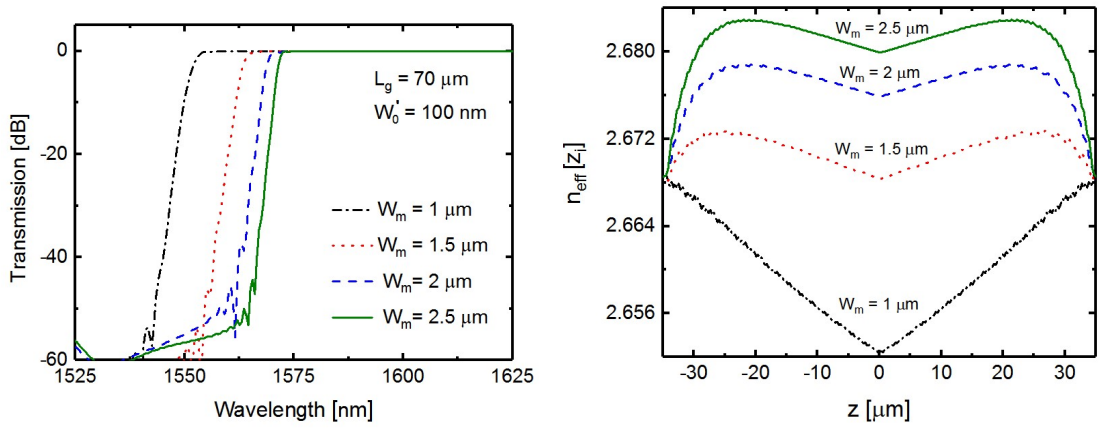

(b)

Figure 4.6: (a) 3D-FDTD transmission response and (b) calculated $n_{eff}(z_i)$ profiles (for TE-polarization) of the device with L_g = 70 μm and W_0' = 100 nm for four different values of W_m. See text for other parameters.

λ_{edge} can be obtained by engineering the maximum width of SWG waveguide at the center (W_m). The transmission characteristics for apodized SWG waveguides with L_g = 70 μm simulated for a set of W_m values are shown in Figure 4.6(a). The red-shift in band-edge wavelength with the increase of W_m is a direct result of differential changes in S_κ, S_g and L_B which can be approximated as:

$$\Delta\lambda_{edge} = \frac{d}{dW_m}\left[\lambda_{sb}^{c} + \frac{\Delta\lambda_{sb}}{2}\right]\Delta W_m \tag{4.10}$$

It is evident that the λ_{edge} could be detuned significantly with W_m. However, this red-shift slows down for larger values of W_m. This is expected since the n_{eff} increase is initially large and gradually saturates for larger values of W_m as shown in Figure 4.6(b).

4.2 Experimental Results and Discussion

The integrated edge filters with input/output photonic wire waveguides and terminated with grating couplers were fabricated in 220 nm SOI substrate (BOX layer - 2 μm, handle wafer - 500 μm). The input/output access waveguides (and reference waveguides) were designed with W_0 = 450 nm and h = 160 nm to ensure TE polarized single mode guidance (as discussed in Chapter-3). All the fabricated devices are 3-mm long (measured between input and output grating couplers) and fabricated by e-beam lithography (using negative tone HSQ resist) and subsequent dry etching (ICP-RIE). The same fabrication process steps described in Chapter-3 have been followed here also. For a given waveguide cross-sectional geometry with fixed period and duty-cycle, we have fabricated four sets of devices to study the influence of apodized grating length L_g and width W_m on band-edge position, roll-off and extinction ratio of the edge filter. The details of the fabricated device (sample S_3) are given in Table 4.1 and the corresponding mask file is shown in Figure 4.7. Some devices were found to be defective due to fabrication induced errors and overdose issues. We will be reporting the results of some of the best devices below: Figure 4.8(a) shows the SEM image of the fabricated SWG waveguides of lengths L_g = 30 μm, 50 μm and 70 μm integrated with input/output rib waveguides along with a reference waveguide. The grating width W_m is fixed as 2.5 μm. Figure 4.8(b) shows the SEM image of the 30 μm long SWG waveguide along with zoomed

Table 4.1: List of fabricated devices on sample S_3 for Λ = 285 nm and δ = 0.5.

Set no.	Device type	Device No.	Device parameters W_m	L_g
1	Straight wg	D_1	-	-
	SWG wg	D_2, D_3	1 μm	30 μm
	SWG wg	D_4, D_5	1 μm	50 μm
	SWG wg	D_6, D_7	1 μm	70 μm
2	Straight wg	D_8	-	-
	SWG wg	D_9, D_{10}	1.5 μm	30 μm
	SWG wg	D_{11}, D_{12}	1.5 μm	50 μm
	SWG wg	D_{13}, D_{14}	1.5 μm	70 μm
3	Straight wg	D_{15}	-	-
	SWG wg	D_{16}, D_{17}	2 μm	30 μm
	SWG wg	D_{18}, D_{19}	2 μm	50 μm
	SWG wg	D_{20}, D_{21}	2 μm	70 μm
4	Straight wg	D_{22}	-	-
	SWG wg	D_{23}, D_{24}	2.5 μm	30 μm
	SWG wg	D_{25}, D_{26}	2.5 μm	50 μm
	SWG wg	D_{27}, D_{28}	2.5 μm	70 μm

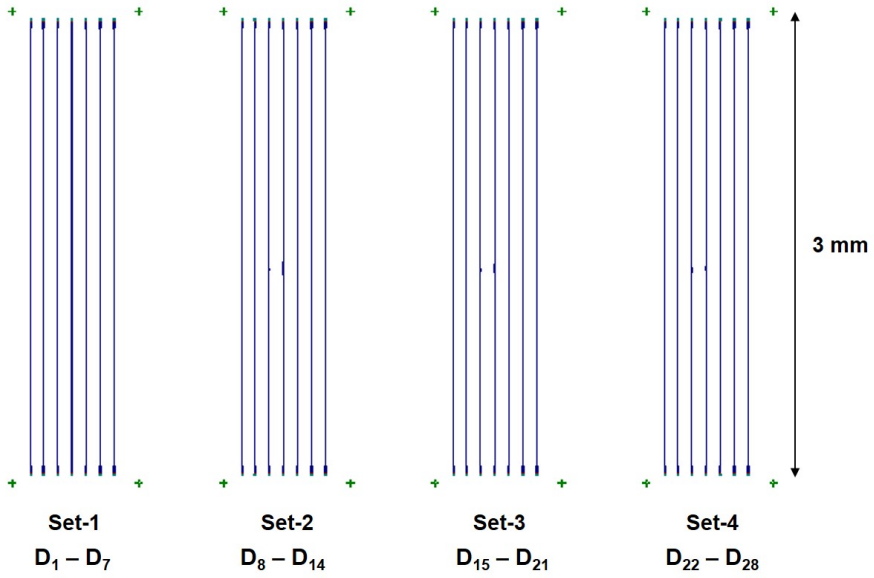

Figure 4.7: Mask layout of the fabricated devices made in GDS II format using Raith Nanosuite software.

image of the central region of SWG indicating little rounding effects along the grating edges. Besides, the grating duty cycle is found to be slightly higher than 50% ($\delta > 0.5$). The optical characterization set-up used is same as the one described in Chapter-3. The normalized transmission characteristics of the devices (D_{23}, D_{25} and D_{27}) for different values of L_g with same width W_m = 2.5 μm are shown in Figure 4.9. As expected, the

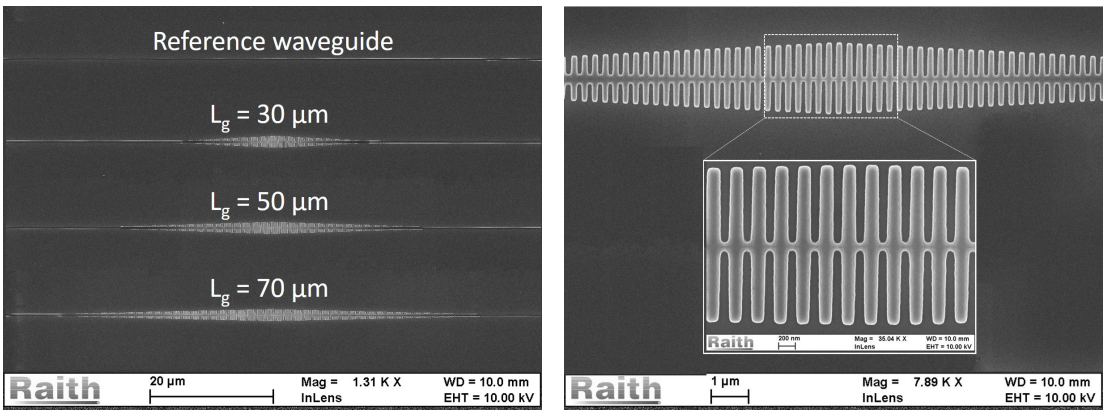

(a) (b)

Figure 4.8: SEM images of the fabricated devices: (a) SWG waveguides with different apodization lengths along with a reference rib waveguide; (b) zoomed section of a 30-μm-long apodized SWG waveguide.

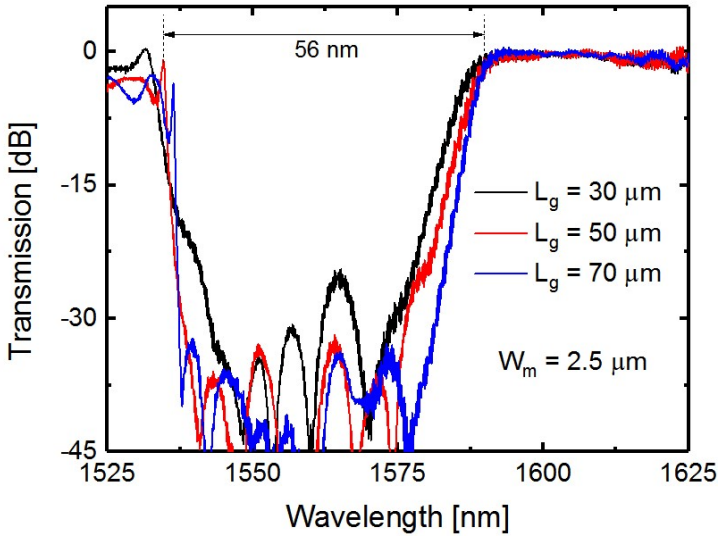

Figure 4.9: Normalized transmission spectra of the fabricated devices (D_{23}, D_{25} and D_{27}) for different values of L_g with same width W_m = 2.5 μm.

values of λ_{sb}^{c} ($\sim$ 1560 nm) and $\Delta\lambda_{sb}$ ($\sim$ 56 nm) are found to be unchanged for all the three devices. However, the most important observations are a flat-top SWG waveguide transmission at longer wavelengths ($\lambda > \lambda_{edge} \sim$ 1580 nm) with negligible insertion loss ($<$ 0.5 dB) and a smooth band-edge roll-off as predicted in simulation results. The values of ER ($>$ 40 dB) and of band-edge slope (3-4 dB/nm) are increased with the device length. The lower values of ER, $\Delta\lambda_{sb}$ and longer values of λ_{sb}^{c} obtained from the experimental results compared to those obtained from the FDTD simulations may be attributed to the underestimation of the experimental ER values and deviations in

δ ($>$ 0.5) for fabricated devices as described earlier. Oscillations are observed within

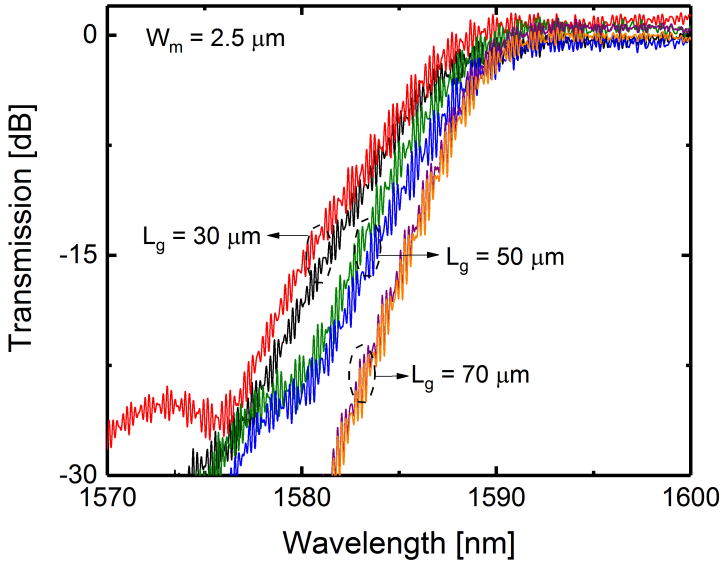

Figure 4.10: Comparison of the transmission spectra of the above devices (D_{23}, D_{25} and D_{27}) with their respective copies (D_{24}, D_{26} and D_{28}).

the stop-band of the fabricated devices, which is mainly due to the noise-level detection limit of the characterization setup. The typical insertion loss between the input and output grating couplers of a reference waveguide exceeds 15 dB. This results in a transmitted power level of $<$ -30 dBm in the SWG passband for the wavelength-tunable laser source used in our characterization setup and hence the stop-band power level reduces to $<$ -70 dBm for a 40 dB extinction. The undesirable noise modulations towards the longer wavelengths is due to the poor coupling efficiency of input/output grating couplers. Figure 4.10 shows the comparison of the transmission spectra of the above devices (D_{23}, D_{25} and D_{27}) with their respective copies (D_{24}, D_{26} and D_{28}). It can be seen that the values of λ_{sb}^{c} and band-edge slope are nearly same from device to device. Further we analyzed the edge filter characteristics of the devices D_6, D_{13} and D_{20} for different values of W_m keeping L_g as a constant parameter (L_g = 70 μm). We observed that λ_{edge} shifts towards longer wavelengths with increasing W_m (see Fig. 4.11). Though the wavelength shift trend follows the simulation results, the simulated and experimental band-edge values do not exactly match. Also, the ripples in the roll-off edge range from $\pm$0.2 dB for W_m = 1 μm to $\pm$2 dB for W_m = 2.5 μm. All these deviations may be attributed to the fabrication-induced edge rounding and δ variations in the SWG waveguides with larger W_m as described earlier. This can be visualized in the inset of Figure 4.11 which shows the SEM images of the grating structures having W_m = 1 μm

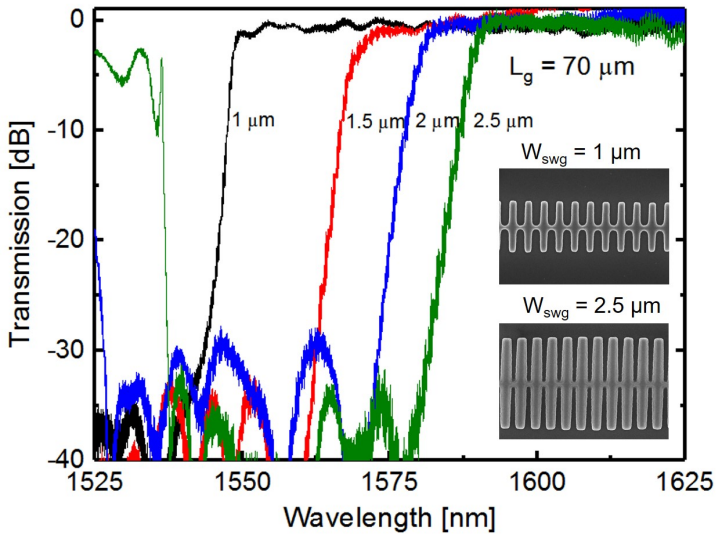

Figure 4.11: Normalized transmission spectra of the fabricated devices (D_6, D_{13} and D_{20}) for different values of W_m with same length L_g = 70 μm.

and 2.5 μm. While the former one has a duty-cycle of 0.5, the duty-cycle of the latter has increased to 0.8. Thus apodization length and width of the grating are the two major factors that decide the filter characteristics like band-edge wavelength, extinction ratio and edge roll-off.

4.3 Summary

In summary, an integrated optical edge filter is designed and demonstrated using an apodized SWG waveguide in the SOI platform. The filter band-edge exhibits a smooth roll-off with a stop-band extinction of $>$ 40 dB. The transmission band-edge (λ_{edge}) of the proposed device can be positioned by setting appropriately the value of W_m, while keeping the grating period Λ and all other waveguide parameters unaltered. The typical edge slope of $\sim$ 3.5 dB/nm is obtained for a SWG waveguide with L_g = 70 μm and W_m = 2.5 μm. The slope of the filter edge can be engineered by tailoring SWG waveguide length L_g. It is worth mentioning that increasing the etch depth and thus increasing the contrast will also strongly enhance the band-edge slope, which we have not considered in this thesis. Such a filter design can be potentially used for various integrated silicon photonics functions, e.g., band rejection, switching, modulations, wavelength-dependent delays and lab-on-chip sensing.

CHAPTER 5

Refractive Index Sensor

Integrated label-free optical sensors have immense potential to be employed in many fields such as medical science, food quality control, defense applications, environmental safety, etc. Immunity to electromagnetic interference, fast response, high sensitivity, compactness and robustness are some of the key factors which bring photonic sensors into the spotlight [158]. Most of the integrated photonic sensors demonstrated so far are based on evanescent field sensing, i.e., these devices facilitate interaction between the analyte and the evanescent tail of the guided mode to induce a change in the effective index of the mode. This change in effective index is translated into a measurable quantity depending on the device configuration, say, resonant wavelength in a ring resonator or photonic crystal cavity, output power intensity in a Mach-Zehnder interferometer etc. Furthermore, they offer the capability of being incorporated in lab-on-chip diagnostics that is proficient to perform point-of-care (P-O-C) measurements at an affordable cost. Various photonic label-free sensors have been developed in silicon photonics platform to deliver accurate diagnostics, such as ring resonators [38, 39], photonic crystal cavities [41], DBR gratings [42] etc. However, a high resolution optical spectrum analyser (OSA) and tunable laser source (TLS) are often required to operate these devices thereby making it a costly affair. On the other hand, transmitted intensity or power read out optical sensors neither require expensive TLS nor a high-end OSA [43]. The Mach-Zehnder Interferometer (MZI) based configuration has proven to be an excellent sensing platform and there has been considerable research interest in demonstrating MZI sensors that facilitate increased light-matter interaction such as MZI with slow-light photonic crystal in one arm [159], porous silicon MZIs [160], MZIs with slot waveguides [161] etc. However, these configurations suffer from some challenges like the need for a separate interaction window for the sensing arm of MZI which adds to a critical lithography step and a large footprint, usually in the order of several millimeters. Also, the sensitivity and limit of detection (LOD) of an MZI based optical sensor rely on how efficiently the sensing arm interacts with cladding analytes.

In this chapter, we investigate an integrated optical MZI device in SOI platform whose phase difference between the two arms can be suitably engineered to act as a wavelength / intensity interrogation sensor for a range of wavelengths ($\lambda \sim 1550$ nm). This is achieved by using SWG as a sensing waveguide in one of the MZI arms. We first carry out the step by step design and analysis of each component in the MZI circuit, namely, sensing arm (SWG waveguide), reference arm (straight waveguide), 3 dB power splitters etc. It is followed by the sensitivity calculation of the MZI device by simulating the wavelength dependent phase response and transfer function of the MZI as a function of different cladding refractive indices (n_c). Finally, MZI based refractive index sensor is fabricated and tested using the optimized design parameters obtained from simulation results.

5.1 Device Design and Simulations

Figure 5.1 shows the schematic illustration of the proposed integrated optical MZI sensor in SOI platform. One arm of the MZI which is integrated with SWG waveguide acts as the sensor arm and the other acts as the reference arm. The interferometer uses

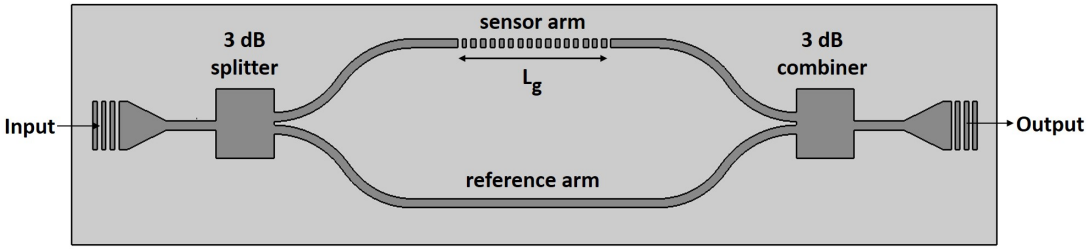

Figure 5.1: Schematic 2D illustration of the proposed integrated optical MZI sensor with SWG waveguide in signal arm and a straight waveguide in the reference arm.

3 dB power splitter/combiner on either sides and is accessed by photonic wire waveguides which are designed for single mode TE polarization guidance and terminated with grating couplers for fiber to/from chip light couplings. When the interferometer input is excited by a light signal, it is equally divided into two arms, propagate through the signal arm and reference arm and get combined at the output after passing through the 3-dB combiner. The output spectrum is modulated by the difference in the phase shifts

experienced by the light propagating through the two arms. The wavelength dependent power transfer function of an MZI can be mathematically expressed as

$$\mathcal{T}(\lambda) = \frac{P_{out}}{P_{in}} = \frac{1}{2}[1 + \cos\Delta\Phi(\lambda)] \tag{5.1}$$

where P_{out}, P_{in} are the output and input power, $\Delta\Phi(\lambda)$ is the phase difference between the two arms given by

$$\Delta\Phi(\lambda) = \frac{2\pi}{\lambda}\Delta n_{eff}(\lambda)L_g \tag{5.2}$$

where L_g is the length of the SWG waveguide and $\Delta n_{eff}(\lambda)$ is the effective refractive index difference between the signal arm and the reference arm at an operating wavelength λ. The wavelength dependent response of the transfer function can be customized to the desired shape by designing the SWG parameters in the signal arm, width of the reference arm, 3-dB coupler and length of the MZI arms. In the following sections, the design of each component will be discussed and finally come up with an optimal MZI design to act as an integrated optical sensor with high sensitivity.

5.1.1 SWG Waveguide: Sensitivity Studies

In this section, we will discuss the potential of using SWG waveguide as a sensing platform by investigating its capability to tailor dispersion characteristics and spatial mode field distribution thereby enhancing the light-matter interaction. Due to the air-gaps between the gratings, the electric field gets delocalized and hence the field is enhanced at the side-walls as well as between the silicon blocks. This improved light-matter interaction is the seed for high sensing capability of SWG waveguides. Figure 5.2 shows the 3-D schematic representation of a SWG waveguide used for sensing applications. The top cladding has refractive index n_{clad}, which is generally a low index material (bio-receptor/analyte). Typically, the sensitivity of a waveguide is denoted in two ways: change in the waveguide mode effective index n_{eff} as a function of change in refractive index of the top cladding n_{clad} (bulk sensitivity, S_b) or as a function of increase in the adsorbed layer thickness (surface sensitivity, S_s) [162]:

$$S_b = \frac{\partial n_{eff}}{\partial n_{clad}} RIU/RIU \tag{5.3}$$

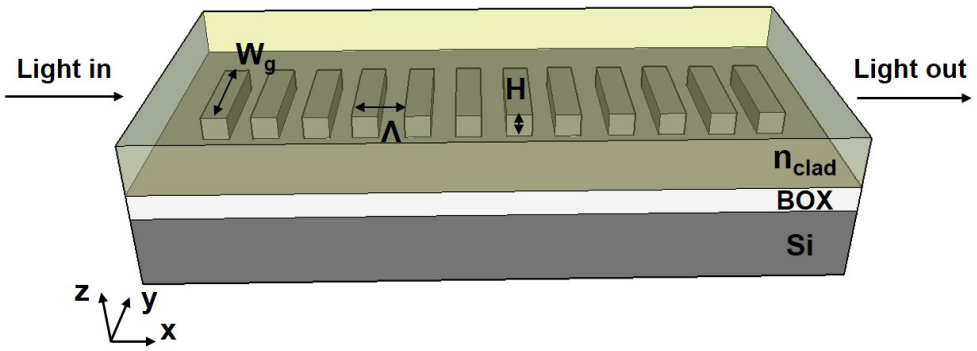

Figure 5.2: Schematic 3D view of the SWG waveguide for bio-sensing in silicon on insulator platform.

and

$$S_s = \frac{\partial n_{eff}}{\partial t} RIU/nm \tag{5.4}$$

where t is the thickness of the adsorbed layer. Figures 5.3(a) and 5.3(b) show the schematic illustration of how a 2-D SWG waveguide can be utilized for bulk sensing and surface sensing respectively. In the bulk sensing scenario, the refractive index change occurs over the entire sample whereas in the case of surface sensing, the change in refractive index occurs over a small area above the sensor region. Aqueous base (DI water: $n_c \sim 1.31$) is often used as the solvent medium for the analyte in bulk sensitivity measurements. Whereas for surface sensitivity calculations, where biomolecules are often grown on the sample, one needs to consider the cladding refractive index of the specific bio-molecule in the design. In this thesis, we limit our discussions to bulk sensitivity case only.

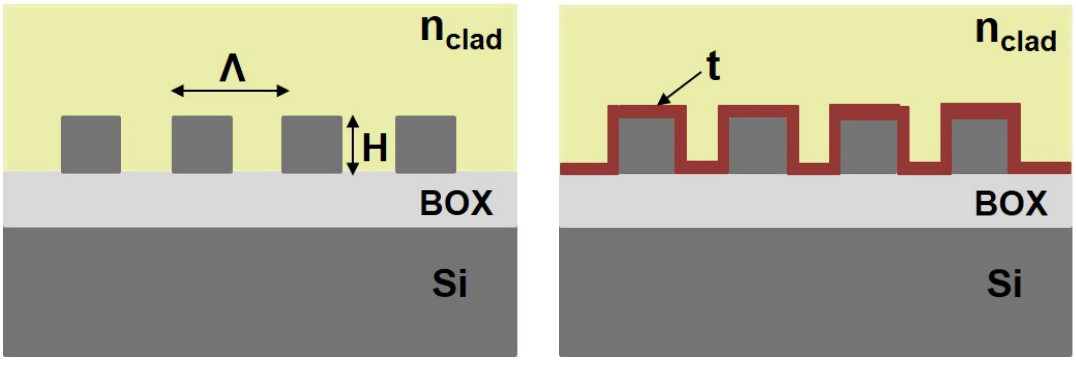

(a) (b)

Figure 5.3: Schematic illustration of (a) bulk sensitivity and (b) surface sensitivity.

In order to realize sensors with higher sensitivity and lower limit of detection, it is important to study the influence of different geometrical parameters of the grating such as etch depth, period (Λ), width (W_g), duty-cycle (δ) etc. In this study, we consider fully etched SWG waveguides (H = 220 nm) to facilitate improved interaction of the cladding analyte with the delocalized mode in the grating gaps. We analyze the bulk sensitivity of the SWG waveguide by assuming the upper cladding to be DI water ($n_c \sim$ 1.31 at λ = 1550 nm). The SWG waveguide can be designed to operate in the 1550 nm regime by suitably choosing the grating parameters to ensure that no Bragg reflection occurs, i.e., the device always operates in the SWG guidance regime. We first discuss

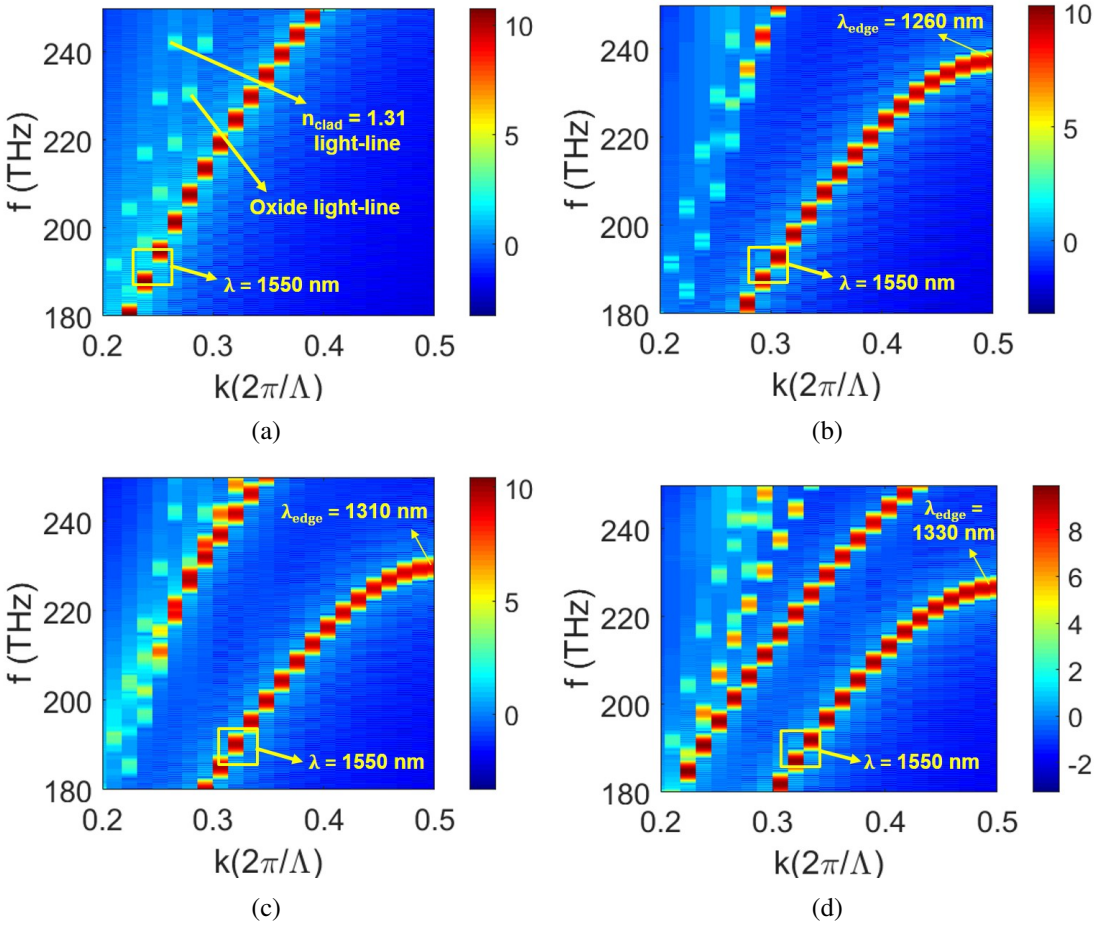

Figure 5.4: The band-structure diagrams calculated for sub-wavelength gratings with (a) W_g = 500 nm (λ_{edge} = 1.12 μm), (b) W_g = 1 μm (λ_{edge} = 1.26 μm), (c) W_g = 1.5 μm (λ_{edge} = 1.31 μm) and (d) W_g = 2 μm (λ_{edge} = 1.33 μm) keeping Λ = 250 nm, δ = 0.5, n_c = 1.31 and TE polarization.

the dependence of the SWG waveguide sensitivity on the grating width W_g assuming all other parameters fixed. For this, it is essential to ensure that the SWG waveguide

operates in the 1550 nm regime for all the grating widths. Figure 5.4 shows the band-structure diagrams calculated for sub-wavelength gratings with Λ = 250 nm, δ = 0.5, n_c = 1.31 and W_g = 500 nm, 1 μm, 1.5 μm and 2 μm. The band-structure diagrams were calculated by using 3-D FDTD simulator tool as described in Section-2.2.1 of Chapter-2. We observe that when W_g increases from 500 nm to 2 μm, the band-edge shifts down in frequency due to increase in the effective refractive index (Equation-2.9). It is evident that in all the cases, the operating wavelength $\lambda \sim$ 1550 nm is far away from the band-edge, i.e. in the deep SWG waveguide regime. Now we study the wavelength dependent effective index variation of the fundamental TE polarized Bloch mode for W_g = 500 nm (black), 1 μm (red), 1.5 μm (blue) and 2 μm (green) as shown in Figure 5.5. For each grating width, two cladding indices have been considered: n_{clad} =

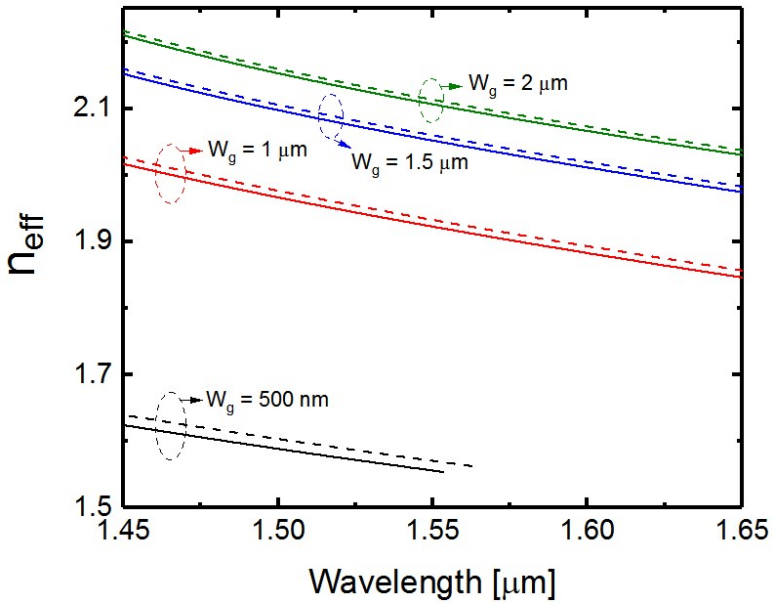

Figure 5.5: Wavelength dependent effective index variation of SWG waveguide as a function of grating width W_g for n_{clad} = 1.31 (solid lines) and 1.32 (dashed lines).

1.31 (solid lines) and n_{clad} = 1.32 (dashed lines). When the grating width is increased, the effective index of the fundamental Bloch mode increased significantly which is expected due to the increased silicon material. Also, the shift in effective refractive index as a function of change in cladding index is reducing with increase in the grating width. When W = 500 nm, S_b is relatively high and the sensitivity drops to smaller values with increase in W. This can be clearly understood by visualizing the mode field distribution in the silicon center and gap center for various grating widths calculated

at $\lambda \sim 1550$ nm as shown in Figure 5.6. The lateral cross-section of the mode fields

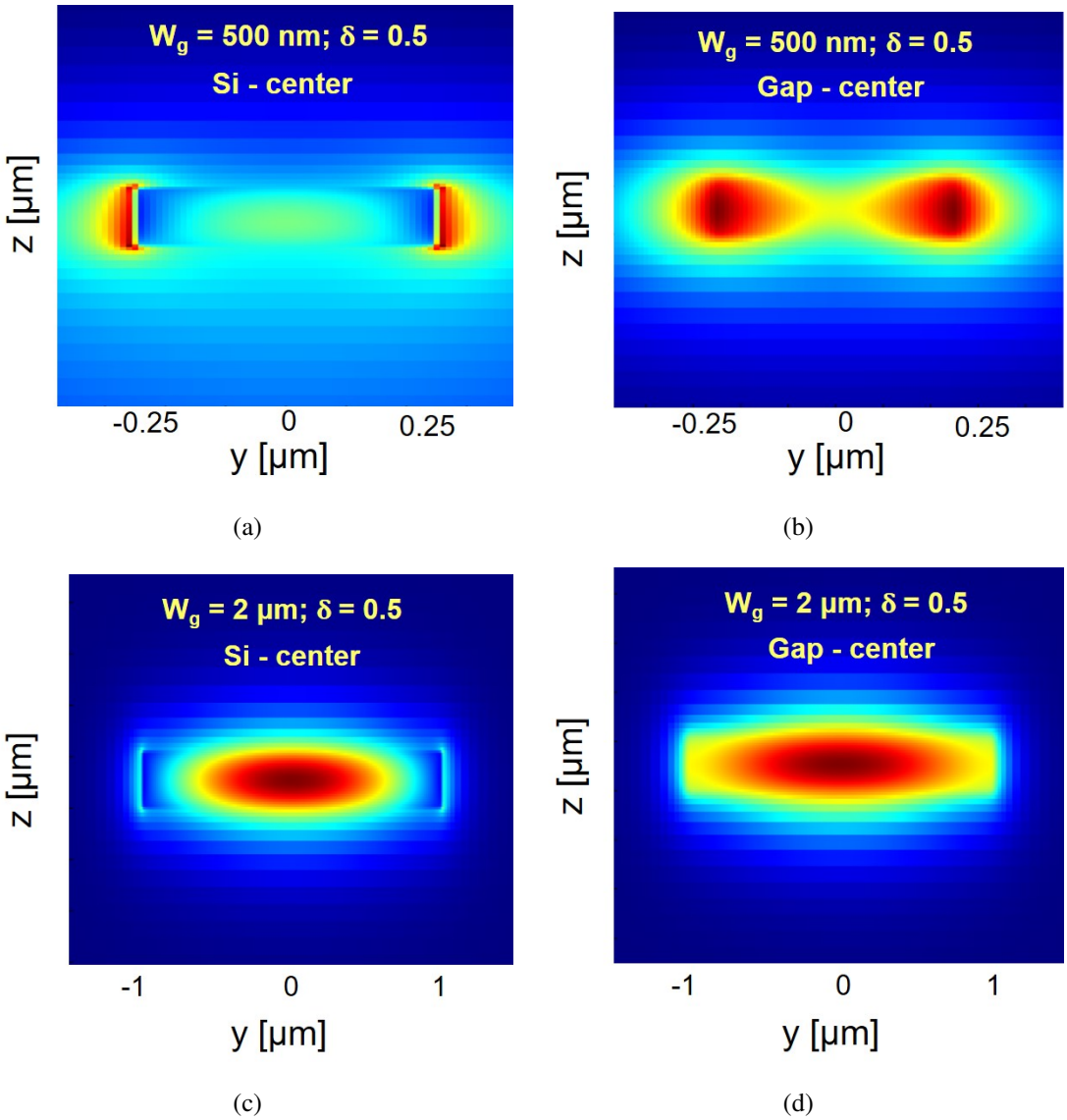

Figure 5.6: The cross-sectional TE mode profiles $|E(x_0, y, z)|$ at $\lambda = 1550$ nm for SWG waveguides at center of silicon segment (left) and center of gap region (right) for $W_g = 500$ nm (top) and $W_g = 2$ μm (bottom) at $\Lambda = 250$ nm and $\delta = 0.5$.

shown on the left hand-side are those in the center of silicon segment whereas those on the right are the center of gap regions. When $W_g = 500$ nm, it is evident that the field is mostly delocalized and significant amount of mode is present towards the sidewalls of the grating region (Figure 5.6(a)) as well as the gap region (Figure 5.6(b)). This facilitates the enhanced interaction of the analyte in the cladding region with the guided mode of the SWG waveguide. However, when $W_g = 2$ μm, the mode is mostly confined towards the center of the silicon segment (Figure 5.6(c)) and gap region (Figure 5.6(d))

thereby reducing the mode-analyte interaction and hence sensitivity.

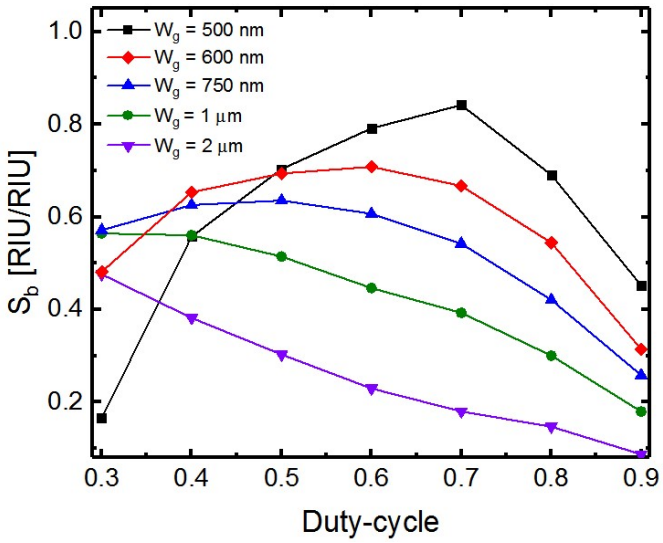

Figure 5.7: Bulk sensitivity of SWG waveguide as a function of duty cycle calculated for TE polarized fundamental mode at λ = 1550 nm for different grating widths.

Another important design parameter that decides the sensitivity of the SWG waveguide is the duty-cycle δ. Figure 5.7 shows the dependence of bulk sensitivity of SWG waveguide on duty-cycle for different grating widths. For sensitivity studies, the refractive index of the cladding, n_c is varied from 1.31 to 1.32. Ideally, a reduction in duty-cycle should delocalize the mode field from the silicon blocks and hence increase the sensitivity. However, we observe that when W_g = 500 nm, the sensitivity increases initially with increase in duty-cycle, reaches a maximum value around δ = 0.7 and then drops down. When the grating width is increased to 750 nm, the maximum sensitivity shifts towards lower duty-cycle and for W_g = 1 μm and 2 μm, sensitivity is maximum when the duty-cycle is minimum. This trend can be explained if we have a look at the SWG waveguide mode field behaviour in the silicon blocks and gap region as a function of duty-cycle as shown in Figure 5.8 for TE polarization at λ = 1550 nm. The left hand side shows the mode field distribution at the center of silicon grating cross-section while those on the right corresponds to the center of the gap region. When W_g = 500 nm and δ = 0.3 (Figures 5.8(a) and 5.8(b)), two effects occur simultaneously due to the relatively higher refractive index of the underlying BOX layer (1.45 as compared to 1.33): the mode volume in the gap region increases thereby enhancing the sensitivity, at the same time, the mode gets displaced to the BOX layer thereby reducing the sensitivity. Hence,

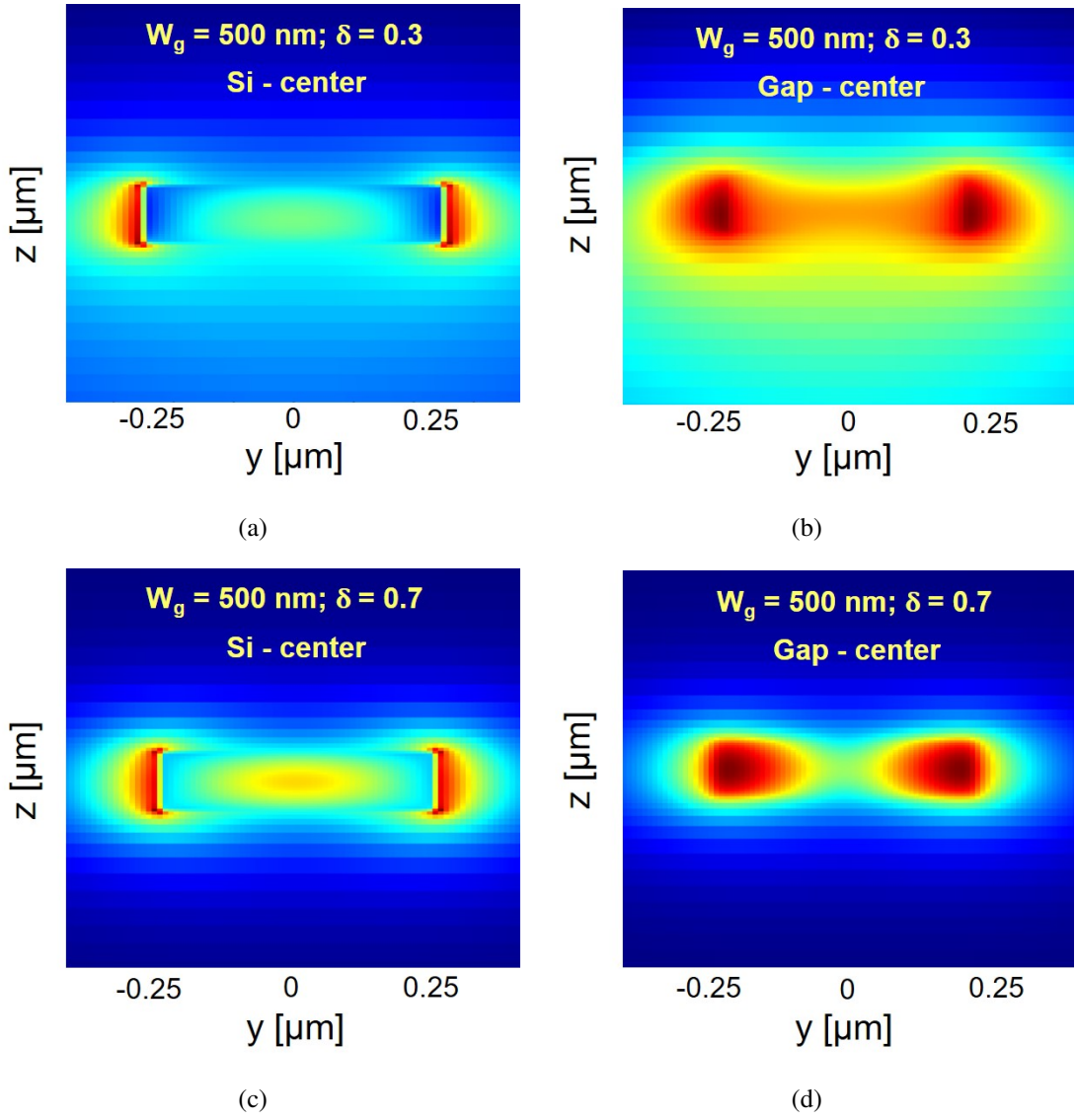

Figure 5.8: The cross-sectional TE mode profiles $|E(x_0, y, z)|$ at λ = 1550 nm for SWG waveguides at center of silicon segment (left) and center of gap region (right) for δ = 0.3 (top) and 0.7 (bottom) at Λ = 250 nm and W_g = 500 nm.

maximum sensitivity is obtained at a point where both the effects reciprocate, i.e. at δ = 0.7 as shown in Figures 5.8(c) and 5.8(d). However for larger grating widths, the sensitivity drops with increase in duty-cycle as the mode gets more confined into the silicon block with increase in duty-cycle and hence has less overlap with the cladding. Thus we can conclude that the sensitivity of SWG waveguide is higher for narrow waveguide widths due to increased interaction of the mode field with the cladding. However, if the width of the waveguide is less, the duty cycle needs to be higher to ensure maximum sensitivity. In a recent paper, it has been reported that though the bulk sensitivity of

SWG waveguide is more for smaller values of W_g, larger widths yield more consistent sensing results when the analyte concentration is low [163]. This is expected since larger grating width implies more silicon region and hence more robust to variation in molecular locations. Thus we decided to go ahead with SWG grating width W_g = 2 μm to have a robust device at the same time reasonable sensitivity. According to the constraints of the fabrication process, the grating width and duty-cycle can be optimally chosen to obtain a reasonably high sensitivity.

5.1.2 Reference arm design

The reference arm which is comprised of a straight waveguide is to be designed to operate for single mode TE polarization. The length of the reference arm is fixed to be the same length as the SWG waveguide in the signal arm. Another important criteria is that if the reference arm is designed such that it is immune to changes in the cladding index n_c, we can avoid the need for a separate interaction window for the signal arm, thus making the fabrication of the device easier and less critical. The reference arm can be made insensitive to cladding index by increasing the waveguide width. Figure

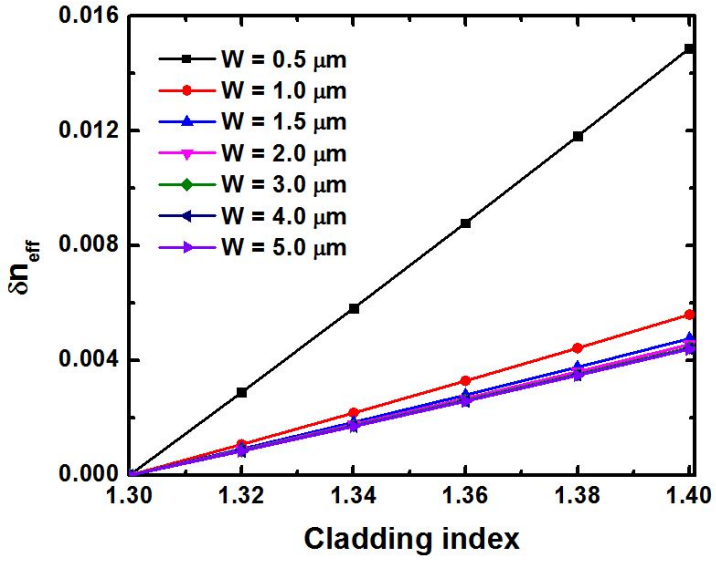

Figure 5.9: Change in effective refractive index δn_{eff} of the TE-guided fundamental mode in reference arm of the proposed MZI as a function of cladding refractive index (n_c) with waveguide width as a parameter (calculated for $\lambda \sim$ 1550 nm).

5.9 shows the change in effective refractive index δn_{eff} of the TE-guided fundamental

mode in reference arm of the proposed MZI as a function of cladding refractive index (n_c) with waveguide width as a parameter (calculated for $\lambda \sim 1550$ nm). It can be observed that for a waveguide width $W > 2$ μm, there is negligible change in the effective refractive index in response to change in cladding index. Hence we fix the reference waveguide width to be 2 μm for further studies. Single mode guidance can be ensured by integrating adiabatic taper into and out of the input/output photonic wire waveguides.

5.1.3 3-dB coupler design

A 1×2 multi-mode interferometer (MMI) is used for the MZI configuration to act as broadband 50:50 splitter and combiner. Compared to WIDC described in Chapter 3, MMI power splitters are robust to fabrication errors [164]. The schematic of a 1 × 2 MMI beam splitter is shown in Figure 5.10. The multi-mode waveguide section consists

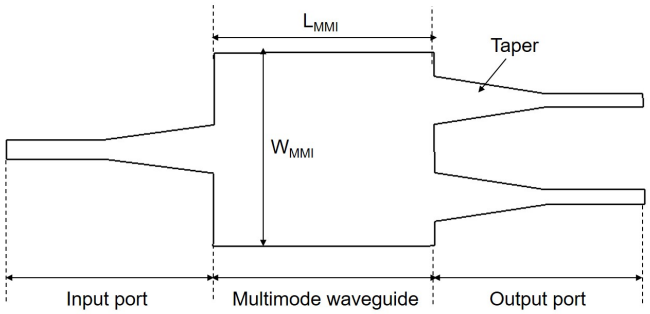

Figure 5.10: Schematic diagram of a 1 × 2 MMI optical power splitter.

of a core region having width W_{MMI} and length L_{MMI}. Initially, we fix the wavelength λ = 1550 nm, which means the MMI splitter is designed to have maximum power output at a wavelength of 1550 nm. Next we decide the width of the MMI core region, W_{MMI}. While deciding the MMI width, two factors need to be considered. First, the two output waveguides of 1 × 2 MMI are placed at $\frac{W_{MMI}}{4}$ with respect to the center of MMI. So, there should be sufficient distance between the centers of output waveguides to ensure fabrication tolerance. The second critical factor is that the multi-mode core should support at least three optical modes for proper interference to take place. We chose the MMI core width, W_{MMI} to be 4 μm to ensure compact dimensions. Lumerical MODE Solutions was used to calculate the number of supported modes λ = 1550 nm to ensure the multi-mode guidance of the MMI core. Next we need to design the length of the

MMI, L_{MMI}. We first determine the beat length between the first two lowest order modes given by [165]:

$$L_\pi = \frac{4 n_{eff} W_{MMI}^2}{3\lambda_0} \tag{5.5}$$

where n_{eff} = 2.82482 is the effective index of the fundamental mode in the multi-mode core region at free-space wavelength λ_0 = 1550 nm and W_{MMI} = 4 μm. This yields L_π = 38.88 μm. The required length for a 1 $\times$ 2 MMI to form a 2-fold image is given by

$$L_{3dB} = \frac{3}{8} L_\pi \tag{5.6}$$

In our case, the optimal length for 3-dB splitting is L_{3dB} = 14.6 μm. In addition, 10 μm long tapers are integrated at the input as well as output ports to ensure adiabatic mode transition between the MMI section and the access waveguides. Figure 5.11(a) shows the transmission response at one of the output waveguides of MMI coupler calculated using Lumerical 3D FDTD.

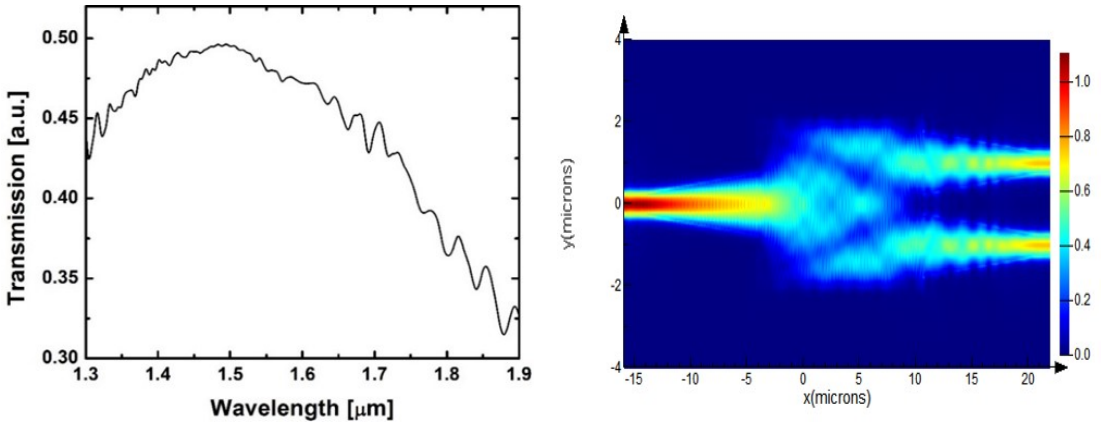

(a) (b)

Figure 5.11: (a) The transmitted power of the TE fundamental guided mode at one of the output ports of the MMI coupler calculated as a function of wavelength using Lumerical 3D FDTD and (b) the visualization of the field propagation through the MMI region by placing a mode field monitor.

The MMI response is highly wavelength dependent with maximum power output at λ = 1550 nm. Each of the output waveguides show about 0.49 of the input power. The difference from the ideal value of 0.5 could be attributed to the small numerical errors in the simulation. The mode propagation through the MMI region is visualized in Figure 5.11(b) by placing a mode field monitor along the length of the MMI in the

Lumerical 3D FDTD.

5.1.4 Wavelength independent interference

Now that the individual components for the MZI based intensity interrogation sensor are designed, we will discuss the wavelength dependent phase response of the MZI as a function of SWG waveguide (signal arm) width. Our motive is to obtain a wavelength independent phase response over the desired range of operating wavelength for utilizing it as an intensity interrogator. We fix the reference arm width to be 2 μm as discussed in Section 3.1.2 so that it is relatively insensitive to change in cladding refractive index. The phase difference between the signal arm and reference arm of the MZI is given by

$$\Delta\Phi(\lambda) = 2\pi L_g \frac{\Delta n_{eff}(\lambda)}{\lambda} \tag{5.7}$$

where $\Delta n_{eff}(\lambda)$ is the change in effective refractive index of the signal arm and reference arm. From the above equation, it is evident that for a fixed grating length L_g, the phase response of the MZI circuit depends primarily on $\Delta n_{eff}(\lambda)/\lambda$. Figure 5.12 shows the phase response curve per unit length of the MZI, $\Delta\Phi(\lambda)/L_g$ calculated as a function of wavelength for grating widths W_g = 750 nm, 1 μm and 2 μm. Solid and dashed lines correspond to Λ = 250 nm and 260 nm respectively and the cladding index is assumed to be n_c = 1.31. It is clear that the phase response is nearly independent of wavelength for a certain range of wavelengths. This wavelength independent response shifts towards longer wavelengths with increase in grating width. When the period of the grating is increased from 250 nm to 260 nm, wavelength independent phase response slightly shifts towards longer wavelengths. We fix the grating period Λ = 260 nm for further studies since it was giving nearly wavelength independent response around λ = 1550 nm when W_g = 2 μm and n_c = 1.31. Another factor to be noted is that the peak phase difference values decrease with increase in grating width. However, we had already discussed in the previous section that larger values of W_g yield more consistent sensitivity values due to its inherent robustness to variations in molecular locations. The phase response per unit length of the MZI as a function of wavelength for cladding indices n_c = 1.31, 1.315 and 1.32 ($\sim$ water cladding) were simulated using 3-D FDTD (Lumerical Solutions,

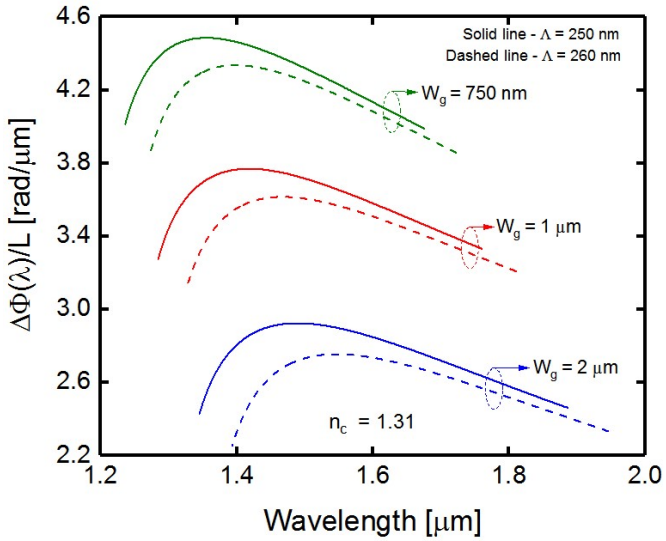

Figure 5.12: Calculated phase response curve per unit length of the proposed MZI as a function of wavelength for different grating widths. Solid and dashed lines correspond to Λ = 250 nm and 260 nm, respectively and the cladding index is assumed to be n_c = 1.31.

Inc.) for W_g = 1 μm and 2 μm as shown in Figures 5.13(a) and 5.13(b) respectively. In both the cases, the increase in cladding index n_c decreases the difference $\Delta n_{eff}(\lambda)$

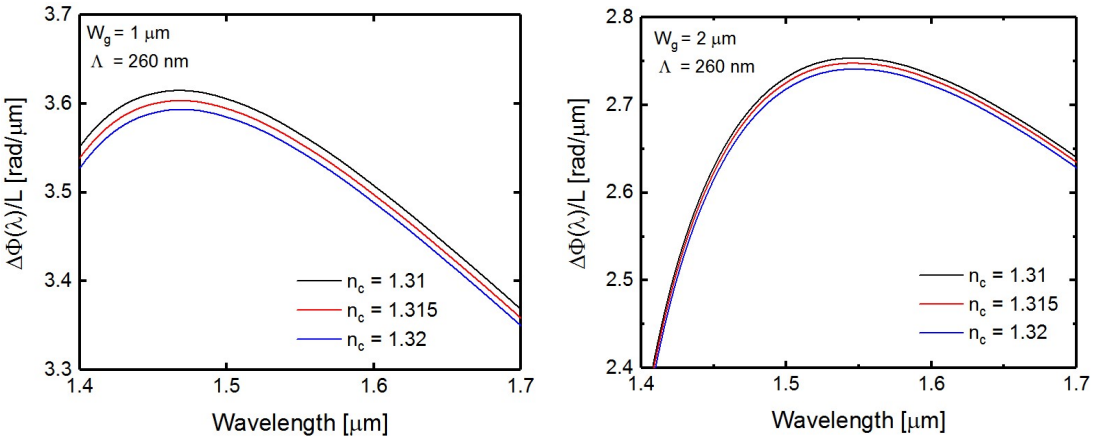

(a) (b)

Figure 5.13: Calculated phase difference (per unit length) between SWG arm and reference arm of the MZI for (a) W_g = 1 μm and (b) W_g = 2 μm for different cladding refractive indices ($n_c \sim$ water). Other parameters are Λ = 260 nm, duty cycle δ = 0.5 and etch depth = 220 nm and W_{ref} = 2 μm.

thereby reducing the phase difference between the two arms. In the wavelength band of interest to us (1525 nm $\leq \lambda \leq$ 1625 nm), this drop in phase response with respect to cladding analyte is falls in the wavelength dependent phase response curve for W_g = 1 μm. On the other hand, when W_g = 2 μm, this corresponds to a wavelength indepen-

dent vertical translation of the nearly flat phase difference region as observed in Figure 5.13(b). Thus, we can utilize the same MZI device as an intensity interrogator as well as wavelength interrogator for a given wavelength range of operation by just engineering the width of the grating.

Another critical design parameter in sensitivity calculations is the length of the signal arm (SWG waveguide length) and reference arm. From Equations 5.1 and 5.2, it is clear that the sensitivity of the MZI device increases just by increasing the length of both the arms. Because of the sinusoidal dependence of the output intensity on the phase difference between the two arms of the MZI, the estimation of device sensitivity is dependent on the operating point. The length of the SWG arm should be designed such that for a chosen range of cladding indices, the interferometer is tuned to the linear region of the transmission curve, i.e.

$$L_g = \frac{(4m+1)\lambda}{4\Delta n_{eff}} \tag{5.8}$$

where m is an integer $(0, 1, 2, 3, ..)$. Taking all the above mentioned factors into account, Figure 5.14 shows the schematic of the proposed integrated optical MZI sensor in SOI platform. The signal arm of the MZI is comprised of a SWG waveguide with

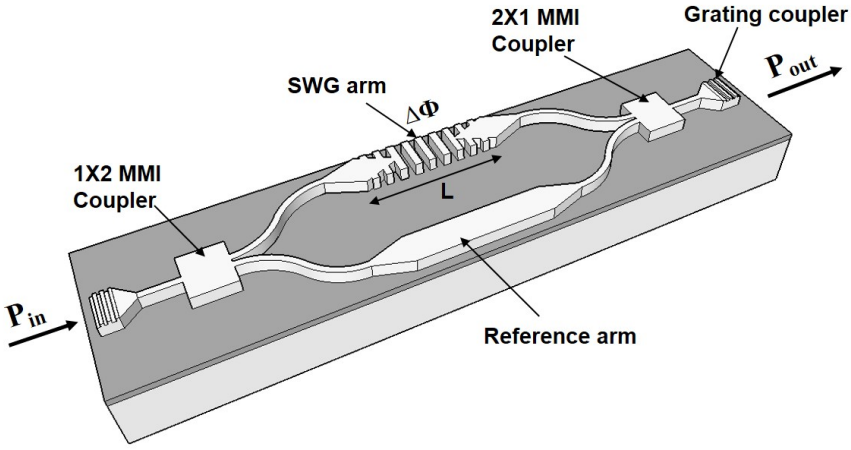

Figure 5.14: Schematic 3D view of the proposed integrated optical MZI sensor in SOI platform.

SWG tapers on both sides to reduce the impedance mismatch. The SWG waveguide is designed to operate in the 1550 nm regime by suitably choosing the grating period Λ = 260 nm, duty cycle δ = 0.5 and etch depth = 220 nm. The reference arm, comprised of a straight waveguide with the same length as that of the signal arm, is designed to operate for single mode TE polarization by integrating adiabatic taper into and out of

the I/O photonic wire waveguides. The reference arm is kept 2 μm wide so that it is nearly immune to changes in the cladding index (n_c). The MZI uses 50:50 MMI splitter and combiner with 150 μm long and 25 μm wide s-bends on either sides. The interferometer is accessed on either sides by photonic wire waveguides (500 nm $\times$ 220 nm) which are designed for single mode TE polarization (as shown in Figure 2.2(b)) and terminated with grating couplers for efficient light coupling. Figure 5.15 shows the transfer function of this MZI device calculated as per Equation 5.1 using MATLAB for cladding refractive indices around water (n_c = 1.31, 1.315, 1.32, 1.325 and 1.33). Both the SWG arm and reference arm are designed for length, L_g = 100 μm (m = 43)

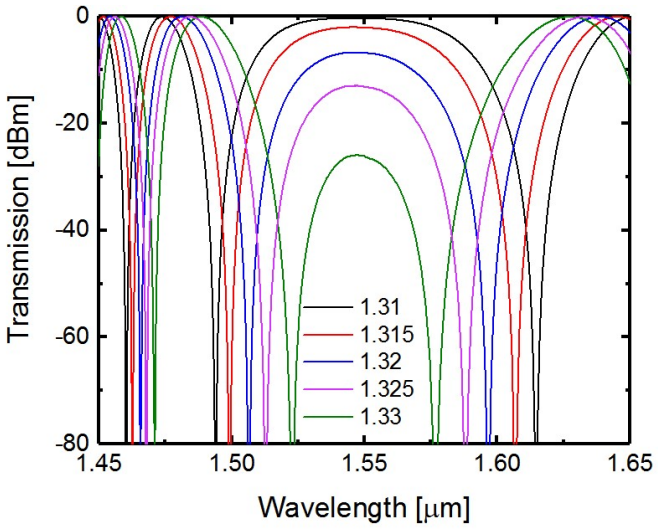

Figure 5.15: Calculated transmission ($\mathcal{T}$) of the proposed MZI as a function of n_c for W_g = 2 μm. Other parameters are Λ = 260 nm, duty cycle δ = 0.5 and etch depth = 220 nm, W_{ref} = 2 μm and L_g = 100 μm.

to get a linear sensitivity response. The interference spectrum exhibits sinusoidal behavior except in the 1.5 μm to 1.6 μm region where the interference pattern exhibits a wide free spectral range (FSR). This wide FSR region corresponds to the range of wavelengths for which $\Delta\Phi$ is nearly wavelength independent. As a result, in this region, the intensity translates from maxima to minima with increase in n_c independent of wavelength. For wavelengths shorter than 1.5 μm, the interference patterns are red shifted with increase in n_c, while for wavelengths longer than 1.6 μm, blue shift is observed. Thus, the MZI can be used as an intensity interrogation based refractive index sensor around λ = 1550 nm as shown in Figure 5.15. The sensitivity of the MZI is calculated based on the change in intensity at the output of the MZI device with respect to

cladding refractive index n_c for a specific wavelength. A sensitivity of 6 dB/0.01 RIU change in n_c is observed in the linear operating region. The same MZI can be used as a wavelength interrogator based refractive index sensor if we operate around λ = 1630 nm. The bulk sensitivity of the MZI around n_c is calculated to be $\sim$ 900 nm/RIU. These sensitivity values are much high compared to the existing wavelength based integrated optical refractive index sensors reported in literature.

5.2 Device Fabrication and Experimental Results

5 sets of the proposed MZI sensor was fabricated on a commercially available 220 nm SOI platform using EBL and ICP-RIE. Table 5.1 shows the list of devices to be fabricated in each set and their design considerations for carrying out the refractive index sensing experiments. Each set contains a reference strip waveguide (D_1), reference

Table 5.1: List of fabricated devices for sensing experiments

Sample	Sample details	Design parameters
S_4	D_1: Reference waveguide D_2: SWG waveguide D_3: MZI device	L_g = 100 μm W_{swg} = 2 μm W_{ref} = 2 μm

SWG waveguide (D_2) and MZI device (D_3) with SWG as one of the sensing arms. Two-step lithography-etch cycle was adopted to fabricate the devices since the grating couplers were designed for shallow etching and the MZI device and reference waveguides were designed for deep etching. Figure 5.16(a) shows the mask layout of the sensor device designed in GDS II format using RAITH Nanosuite software. The total length of the SWG-strip waveguide structure between the input/output edge coupler was 5 mm and the devices were placed 300 μm apart. Figure 5.16(b) shows the zoomed-in view of the adiabatic transition tapers (20 μm long) integrated at the interface of SWG waveguide and access waveguides for mode matching. The schematic illustration of the two-step fabrication process flow adopted for realizing the MZI device is shown in Figure 5.17. All the spin coating, patterning and etching parameters used for fabricating both the steps are detailed in Table 3.4, 3.5 and 3.6 of Chapter 3. After cleaning the SOI sample using the procedure outlined in Appendix C, the entire set of devices was

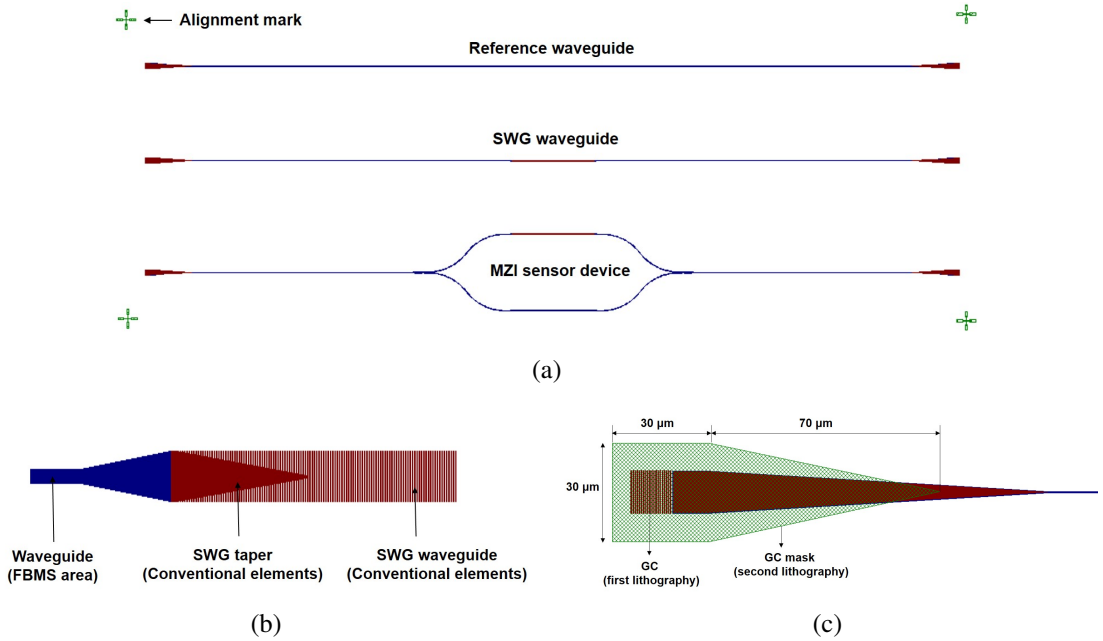

Figure 5.16: (a) Mask layout of the MZI device along with the reference SWG waveguide, straight waveguide and alignment marks designed using RAITH Nanosuit; A zoomed-in view of the (b) SWG spot-size converter and (c) GC region along with the masking layer for second step EBL.

patterned using EBL with HSQ negative tone resist and etched down to $\sim$ 60 nm using ICP-RIE. In the second step, without removing the HSQ mask of the previous step, the device was coated with a second layer of HSQ to mask the grating coupler regions. The mask structure shown in Figure 5.16(c) was critically aligned over the sample using the three-point alignment procedure available in RAITH Nanosuite software. Due to inevitable fabrication issues like beam current fluctuations and stage drifting, a misalignment of $\leq$ 70 nm was observed after patterning. The GC mask is designed such that it acts as an adiabatic taper connecting the shallow etched GC and the fully etched access waveguide. The masked regions were then fully etched down to the BOX layer and the residual HSQ was removed by dipping the sample in HF solution for 10 seconds followed by DI water rinse. A schematic illustration of the GC region after 2 step etching is shown in Figure 5.18. Figure 5.19(a) shows the optical micro-graph of the center portion of the MZI device with SWG waveguide in signal arm and straight waveguide in reference arm. A reference straight waveguide is also shown on the top. Figure 5.19(b) to 5.19(e) show the zoomed-in SEM images of 1 $\times$ 2 MMI splitter, SWG region with taper, adiabatic slab taper in the GC region after two-step etching and GC close-up view respectively. Table 5.2 draws a comparison of the designed and measured device

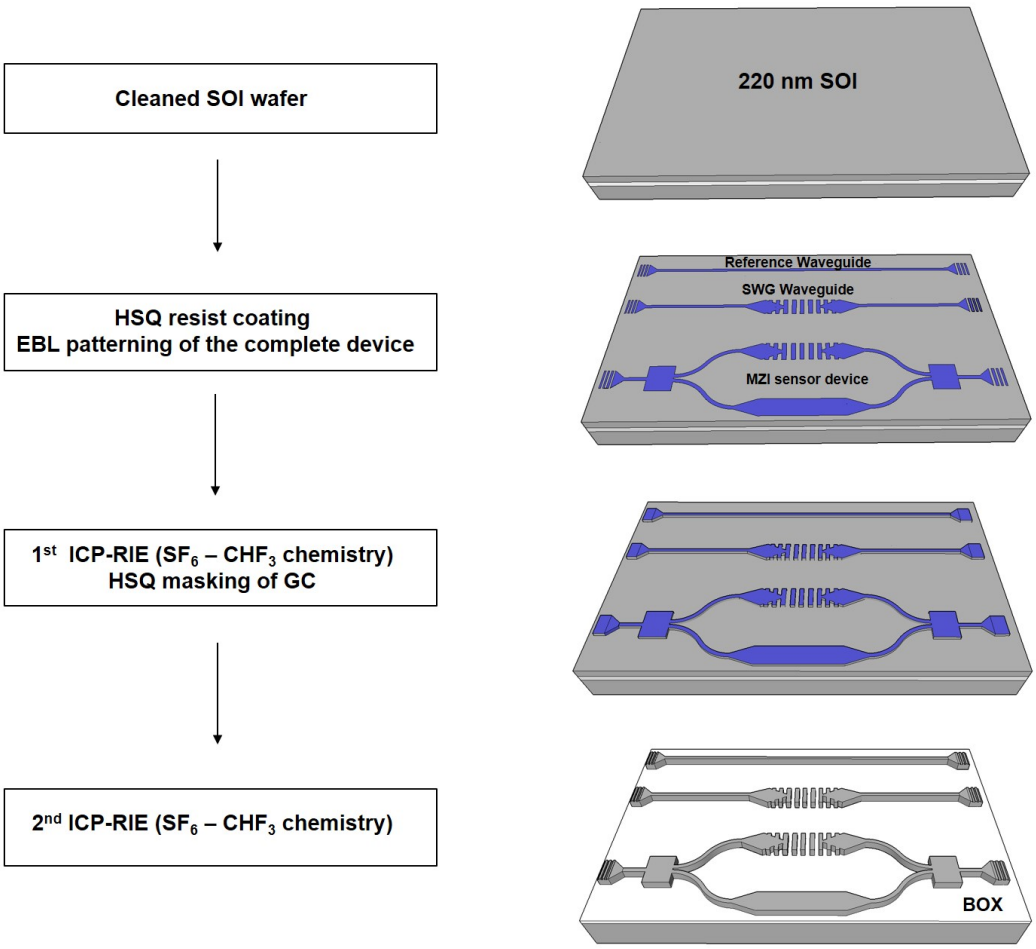

Figure 5.17: 2-step fabrication process flow (left) and 3D schematic (right) of the MZI device along with the reference SWG waveguide and straight waveguide on 220 nm SOI platform using electron beam lithography and ICP-RIE.

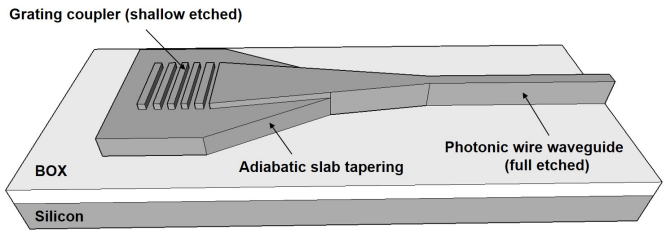

Figure 5.18: 3-D schematic of the shallow etched grating coupler region adiabatically tapered into a fully etched photonic wire waveguide.

dimensions of SWG waveguide, I/O photonic wire waveguide and grating coupler region. The deviations in measured values from the design parameters may be attributed to fabrication related errors like electron beam current fluctuations, proximity effects, etching non-uniformity etc. The fabricated devices were characterized using the fiber-optic probe station described in Chapter-3. A schematic and photograph of the same are shown in Figures 5.21(a) and 5.21(b) respectively. For sensing experiments, we have

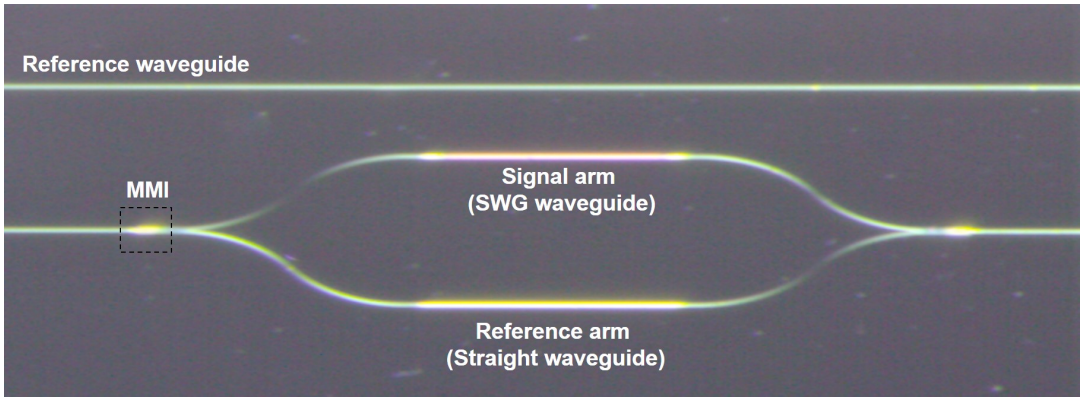

(a)

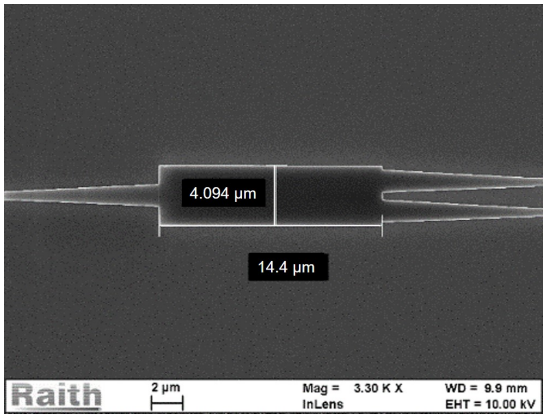

(b)

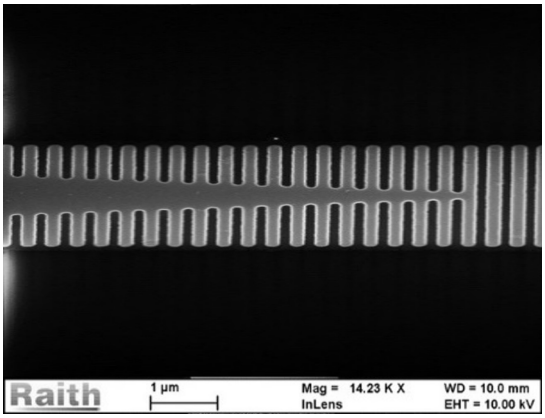

(c)

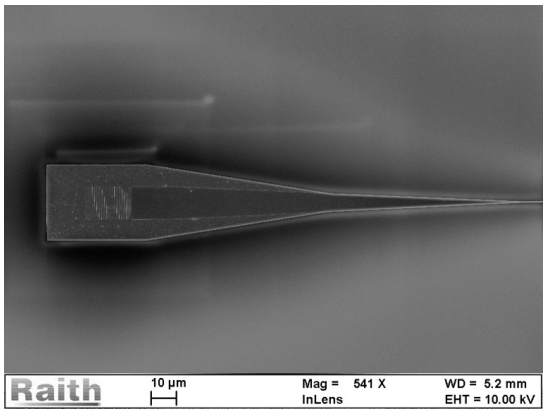

(d)

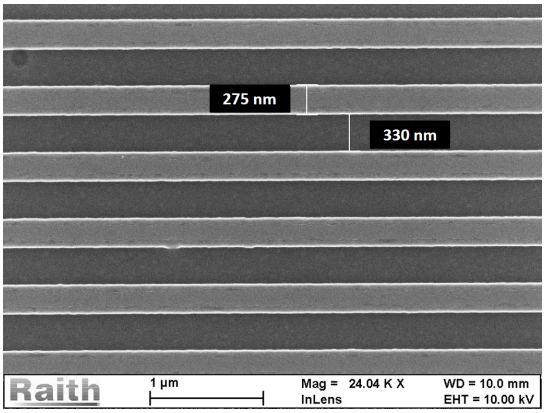

(e)

Figure 5.19: (a) Optical micro-graph of the fabricated MZI device and reference waveguide; Zoomed-in SEM images of (b) 1 $\times$ 2 MMI splitter; (c) SWG region with taper; (d) Adiabatic slab taper in the GC region after two-step etching and (e) GC close-up view.

used commercial refractive index liquids which are procured from Cargille Labs. The sensing experiments are carried out by carefully dispensing a drop of analyte liquid on to the sample via a syringe as shown in Figure 5.21(b). We will discuss the transmission

Table 5.2: Comparison of the designed and measured device dimensions

Parameter	Designed	Measured
Duty-cycle	0.5	0.6
PhWW width	500 nm	600 nm
Etch depth	60 nm (step-1)	
	220 nm (step-2)	$\pm$ 10 nm
GC duty-cycle	0.5	0.48-0.55

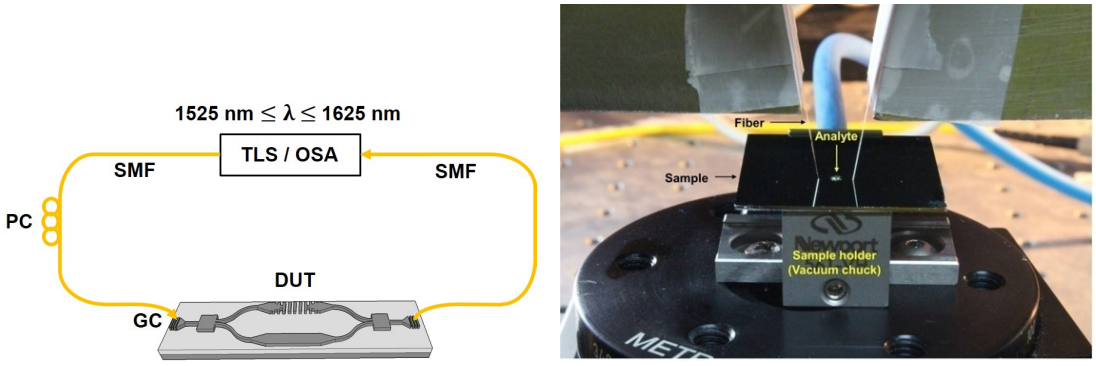

(a) (b)

Figure 5.21: (a) Schematic and (b) photograph of the characterization set-up used for sensing experiment; TLS: Tunable Laser Source, OSA: Optical spectrum analyzer, DUT: Device under test, SMF: Single mode fiber, GC: Grating coupler [124].

characteristics of one set of devices (D_1, D_2 and D_3) in the following section to demonstrate the proof of concept. Figure 5.22 shows the measured transmission spectra of a fabricated reference waveguide D_1 (black curve) along with a reference SWG waveguide D_2 (red curve) integrated with access waveguides via 10 μm long adiabatic tapers

on either sides. The wavelength dependent response of the rib waveguide is due to the

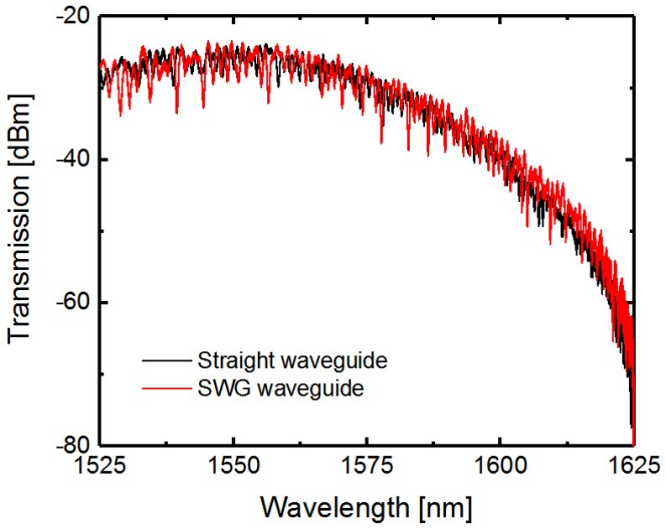

Figure 5.22: Transmission spectra of 100 μm long SWG waveguide (D_2) integrated with access waveguides and the reference waveguide (D_1).

bandwidth limitation of input/output grating couplers. The SWG waveguide response shows ripples ($\pm$ 2 dB) over the desired wavelength range. This is due to the sidewall roughness in the gratings and access waveguides as a result of deep etching. However, there is no significant excess loss for the SWG waveguide when compared with the transmission of reference rib waveguide (IL $<$ 1 dB). We then measured the wavelength dependent transmission of the MZI sensor device (D_3) with cladding refractive indices n_c = 1.31, 1.32 and 1.33 to compare with the simulated results. Figure 5.23(a) shows the measured transmission spectra obtained for the integrated SWG-MZI device for air as top cladding (black curve) as well as for different values of n_c. The transmission response of MZI with air cladding shows a broadband response as expected with negligible insertion loss. The MZI response also shows significant ripples in the spectrum as that of the SWG waveguide. It can be observed that there is an evident drop in the intensity upon increasing n_c from 1.31 to 1.33. The wavelength range from 1570 nm to 1580 nm is zoomed and showed in Figure 5.23(b) to clearly show the drop in intensity with respect to cladding refractive index. Approximately 5 dB/0.01 RIU change in n_c was observed for an MZI with signal arm and reference arm length of 100 μm. This is close to the obtained simulation results for a 100 μm long signal arm and reference arm (6 dB/0.01 RIU). However, experimental results show that the device lies within the linear operating regime for n_c ranging from 1.31 to 1.33. This is in contrast to the theoretical

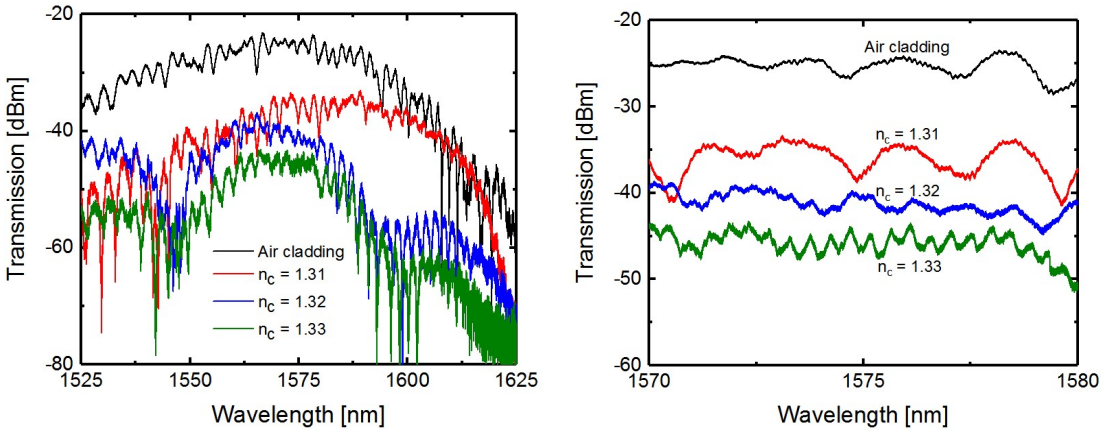

Figure 5.23: (a) Measured transmission spectra of the MZI (D_3) for cladding indices 1.31, 1.32 and 1.33 and (b) the zoomed in spectra to show the drop in intensity upon increasing the n_c.

calculation (Figure 5.15) where the transmitted power dropped down by $\sim$ 30 dB upon increasing n_c from 1.32 to 1.33 indicating that the device is no longer operating in the linear operating regime. We also observe that the nearly wavelength independent phase translation is occurring around $\lambda \sim 1575$ nm (designed to occur around $\lambda \sim 1550$ nm). These differences in the theoretical and experimental calculations could be attributed to the fabrication related imperfections in the MZI device thereby altering the Δn_{eff} between the signal arm and reference arm and hence the required length to tune the interferometer to the linear region of the transmission curve (see equation 5.8). These results are preliminary investigation results and more optimization runs are required for efficient sensor demonstration. Nevertheless, the results are quite encouraging and a comprehensive study in this area can lead to the demonstration of refractive index sensor devices by using simple broadband LED sources.

5.3 Summary

In summary, we have demonstrated a SWG based asymmetric MZI sensor designed for operating at a wavelength $\lambda \sim 1550$ nm. The phase difference between the signal arm and reference arm of the MZI is engineered to obtain a nearly wavelength independent response around $\lambda \sim 1550$ nm. The potential of the SWG waveguide as an effective

sensor platform is explored through simulations by varying different grating parameters. We have used SWG waveguide with W_g = 2 μm to obtain a refractive index sensor which is robust at the same time shows high sensitivity. The reference arm of the device is designed to avoid the need for a separate isolation window for the sensing arm. The device has a length dependent scalable sensitivity. The calculated sensitivity was around 6 dB/0.01 RIU for cladding indices n_c around 1.31 (water). The experimental results show a measured sensitivity of 5 dB/0.01 RIU for a sensing arm of length 100 μm. The deviation of the experimentally measured sensitivity from the designed one can be attributed to fabrication imperfections. This translates to a bulk sensitivity of 8 $\times$ 2π rad/ RIU for an active sensor length of 100 μm. Few of the conventional silicon based interferometric sensors using photonic wire waveguides reported in literature report a bulk sensitivity of 460 $\times$ 2π rad/ RIU for an active sensor length of 2 mm [166] and 300 $\times$ 2π rad/ RIU for an active sensor length of 1.5 mm [167]. However, these devices employ conventional photonic wire waveguides for interferometry and hence require arm length in the order of millimeters to achieve the desired sensitivity. Also, they use an additional lithography step to mask the reference arm. To the best of our knowledge, MZI with a signal arm of SWG waveguide in SOI has not been demonstrated for sensing applications till date. The design flexibility of SWG waveguide parameters provide lot of room for optimisation and further improve the device sensitivity. The obtained results are highly encouraging and provide useful insights for efficient sensor design and demonstration in the future.

CHAPTER 6

Summary and Conclusions

The major contribution of this PhD research is the design and demonstration of integrated optical sub-wavelength grating waveguide based silicon photonics devices for sensing and filtering applications. The major research outcome has been described in preceding five chapters. The entire thesis work and future scopes of research have been summarized in this concluding chapter.

6.1 Thesis Summary

In the introduction chapter, an overview on the evolution of silicon photonics technology was given starting from the pioneering works that served as key technology milestones in the field to the advanced and high performance silicon photonic quantum photonic circuits. We then discussed about various types of silicon waveguides which are imperative for any integrated optical device. Thereafter, the concept and working principle of SWG waveguide was introduced followed by a comprehensive review of the SWG based device designs that have been demonstrated in the field of optical communication and sensing. The challenges in the existing application specific device designs were identified and a set of research objectives were defined.

In chapter 2, the theory of sub-wavelength gratings was discussed and a detailed study was carried out on the different geometry parameters that are instrumental in designing SWG waveguides in a 220 nm SOI platform. It was concluded that the grating period (Λ), corrugation width (d), slab-height (h), grating width (W_g) are the key design parameters to be considered while designing a SWG waveguide for a specific application. Finally, we also investigated various taper designs that can ensure smooth and adiabatic transition of the guided optical mode from the feeder waveguide to SWG waveguide and vice-versa.

In chapter 3, an ultra broadband add-drop filter/switch circuit is designed and demonstrated using a 2×2 balanced MZI designed by cascading two wavelength independent directional couplers acting as 3-dB power splitters. Two identical SWG waveguides are adiabatically integrated in two arms of the MZI. They are designed to operate in TE-polarization with a well defined band-edge wavelength $\lambda_{edge} \sim 1565$ nm (roll-off > 70 dB/nm) dividing its fundamental stopband ($\lambda < \lambda_{edge}$) and guiding passband ($\lambda > \lambda_{edge}$). The stopband and passband of the SWG could be filtered efficiently at the drop port and cross/bar port of the MZI, respectively. Five different microheaters are also integrated at different locations of the MZI for phase correction and switching applications. The band-edge wavelength could be thermo-optically tuned with a slope efficiency of 22 pm/mW. The passband switching between bar- and cross port is demonstrated with more than 15 dB extinction; measured switching power $P_{\pi} \sim$ 54 mW. Thermo-optic modulation is also demonstrated simultaneously at cross-, bar- and drop ports for an operating wavelength λ = 1571 nm (slightly above λ_{edge}). The rise-time and fall-time in thermo-optic modulation is recorded as $\sim$5 μs and $\sim$4 μs, respectively. The lower switching time could be accomplished because of the integration of microheater directly on the silicon slab (in contrast to the conventional microheater integrated over the top cladding oxide).

In chapter 4, an integrated optical edge filter is designed and demonstrated using apodized SWG waveguide. The filter band-edge exhibits smooth roll-off with a stopband extinction of > 40 dB. The typical edge slope of ~ 3.5 dB/nm is obtained for a SWG waveguide with L_g = 70 μm and W_m = 2.5 μm. The slope of the filter edge can be engineered by tailoring SWG waveguide length L_g. More importantly, the transmission band-edge (λ_{edge}) of the proposed device can be precisely positioned by appropriately setting the value of W_m, while keeping the grating period Λ and all other waveguide parameters unaltered.

In chapter 5, we have designed and demonstrated a SWG based asymmetric MZI sensor engineered such that the phase difference between the light propagating through two arms of the MZI are nearly flat over a range of wavelengths ($\lambda \sim 1550$ nm). We first studied the potential of using SWG waveguide as a sensing arm by investigating the influence of different grating parameters. It was concluded that smaller grating width

resulted in improved sensitivity but at the cost of robustness and repeatability. The reference arm width was designed to be 2 μm to make it immune to changes in cladding index. The calculated phase sensitivity of such a device is 6 dB/0.01 change in n_c. The device has a length dependent scalable sensitivity and does not require a separate interaction window for the sensing arm thereby reducing the fabrication complexity. The experimental results show a measured sensitivity of 5 dB/0.01 change in n_c.

6.2 Future Scopes

The detailed study and demonstration of integrated SWG waveguides for sensing and filtering applications opens the gateway to many interesting avenues of research for various silicon photonics applications. For example, the broadband add-drop filter/switch circuit demonstrated in chapter-4 can replace the conventionally used off-chip high extinction filters in quantum photonic circuits. Figure 6.1 shows the schematic of the experimental set-up used for on-chip photon pair generation using spontaneous four wave mixing [168]. Once the photon pair generation happens in the coupled resonator

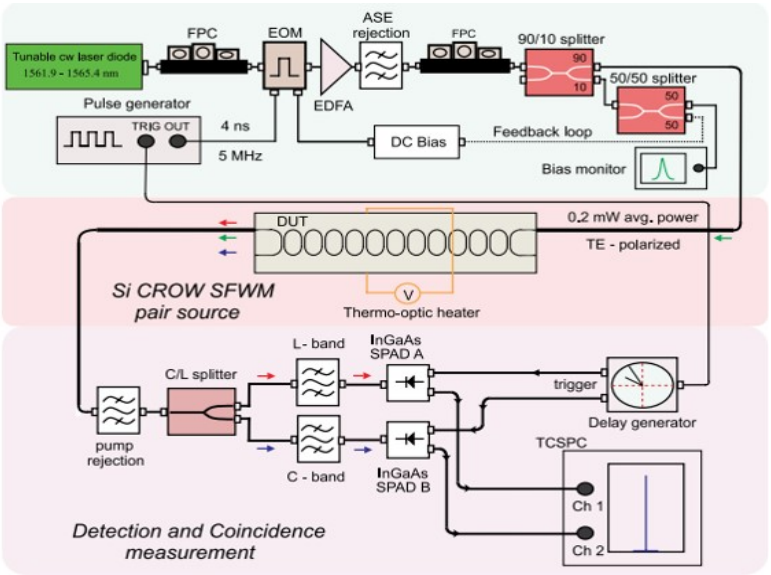

Figure 6.1: Schematic of the experimental set-up for photon pair generation using spontaneous four-wave mixing [168]

.

oscillator waveguide comprising of 11 cascaded microrings and the pump signal is suppressed, the generated signal and idler photons are initially separated using an off-chip

C/L band splitter followed by a series of narrow band filters. The off-chip filters which are being currently used display high passband to stopband extinction exceeding 150 dB but suffer from relatively large coupling loss and packaging expenses. Contrary to this, an on-chip C/L band splitter could potentially provide a compact and energy efficient solution by providing higher integration density and display better performance.

The linear edge filter discussed in chapter-5 can be designed for an improved roll-off factor which could make it potentially useful as an on-chip passive optical filter for RF modulated single sideband suppression in microwave photonic phase shifters [147] and for single-sideband PAM-4 intensity-modulation circuits [148]. The band-edge roll-off can be improved either by further increasing the grating length or by increasing the etch depth of the grating [169]. Figure 6.2(a) shows the topological layout of an

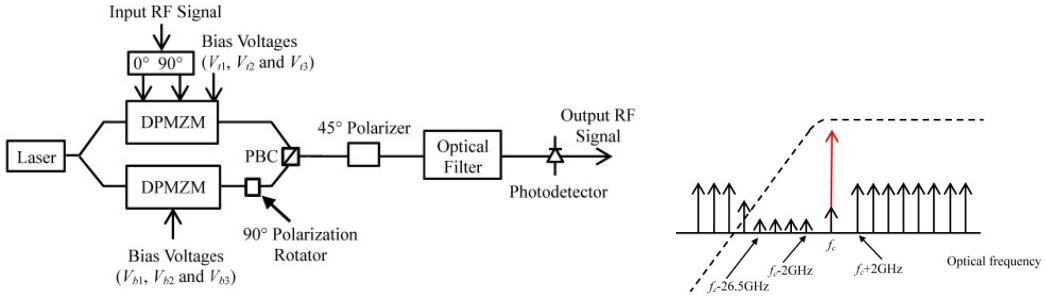

Figure 6.2: (a) Schematic topology of the broadband photonic microwave phase shifter and (b) the output of the SSB modulation circuit along with the frequency response of the optical filter used in the phase shifter (dashed line) [147].

ultra broad microwave photonic phase-shifter circuit, the details of which have been discussed in [147]. An optical filter with frequency response as shown in dashed line in Figure 6.2(b) can be designed to suppress the undesired left sideband of a hybrid SSB modulation circuit over a wide frequency range. The minimum edge roll-off required for such a filter is $\sim$ 120 dB/nm which can be achieved by increasing the length of the apodized SWG waveguide. The same linear edge filters can also be potentially used in lab-on chip optical sensors where a wavelength encoded measurement can be translated to a cost-effective readout mechanism similar to what was demonstrated earlier using fiber optics [149]. The schematic of an intensity interrogation sensor circuit is shown in Figure 6.3 [170]. The light from the broadband source (BBS) passes through the 3-dB coupler and reach the a fiber Bragg grating (FBG) filter which acts as the sensing

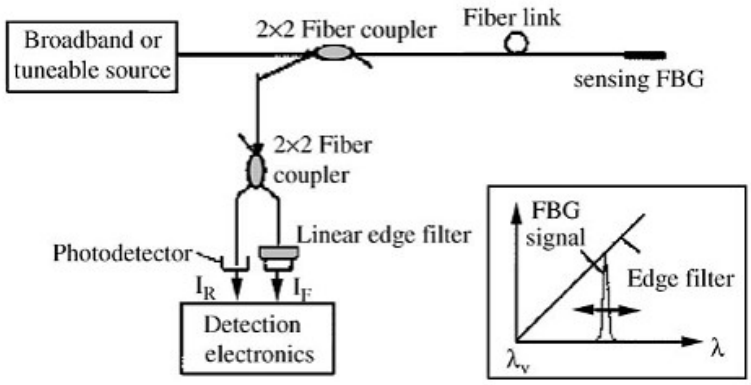

Figure 6.3: 2D schematic layout of the proposed intensity interrogation sensor using linear edge filter

element. The narrow wavelength band reflected from the FBG reaches the linear edge filter. By measuring the intensity change of the edge filter output with respect to the shift in the FBG response, the wavelength shift induced by the measurand is obtained. By taking a ratio of the signal intensity to the reference intensity, the circuit can be made immune to power fluctuations from the light source.

Having said all these, it is important to mention that this thesis work has completely focused on devices that operate for TE polarization. It would be highly desirable to design SWG waveguides that are polarization independent because the optical fibers generally do not conserve the polarization state of light. Also, TM polarized light is always a good choice for conducting sensing experiments due to the increased light-analyte interaction. Another challenging task is to design and demonstrate compact linear edge filters with steep edge-profiles ($>$ 100 dB/nm) which is very much essential for the upcoming quantum and RF photonics research fields.

APPENDIX A

MZI circuit components

In this section, we discuss the design and working principle of grating coupler and wavelength independent directional coupler used in this thesis.

A.1 Grating Coupler : Working principle

Grating coupler has been used throughout this PhD thesis to couple light from standard single mode fiber (SMF) to photonic wire waveguides and vice-versa. The advantage of using grating coupler is that it can be fabricated along with other devices and eliminates the need for additional steps like end facet preparation as in the case of conventional end fire coupling mechanisms. Grating coupler also facilitates light coupling to and from any location on the chip being tested. However, the bandwidth can be limited due to the dispersive operating principle of the grating couplers. The grating coupler design used in this thesis has been adopted from the PhD thesis of Sujith [124]. Figure A.1(a) shows the schematic of the grating coupler assisted SMF to waveguide coupling. The grating,

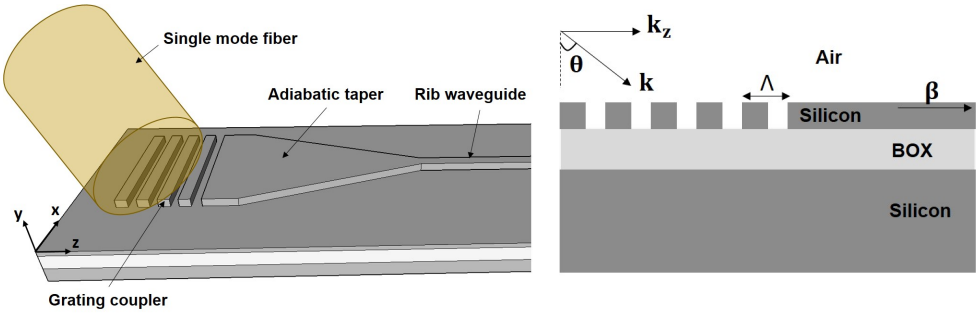

(a) (b)

Figure A.1: (a) Schematic illustration of the grating coupler region along with the input fiber tilted at an angle and (b) Cross-sectional schematic of the grating coupler region.

which couples light from an out-of-plane SMF into the planar silicon waveguide, is

followed by an in-plane taper to couple to a single-mode photonic wire waveguide. Cross-sectional schematic of the gratings along with the waveguide region is shown in Figure A.1(b). When light with a wavevector **k** is incident on the waveguide from a SMF, it undergoes diffraction and a suitable combination of grating period, coupling angle and wavelength cause a fraction of the diffracted light to be coupled to the guided mode in the waveguide using the phase matching condition given as:

$$\beta - k_z = \frac{2\pi}{\Lambda} \tag{A.1}$$

where $\beta = \frac{2\pi}{\lambda_0} n_{eff}$ is the propagation constant of the guided mode of the waveguide, k_z = **k** sin θ = $\frac{2\pi}{\lambda_0}$ sin θ is the z component of the wavevector **k** and Λ is the grating period. Using Eq. A.1, for a grating coupler in a 220 nm SOI to operate in the 1550 nm wavelength region, the optimal grating period is calculated as Λ = 610 nm with duty-cycle δ = 0.5 and slab height $\sim$ 160 nm. The measured 3-dB bandwidth of the above grating coupler was observed to be $\sim$ 70 nm around λ = 1550 nm and typical insertion loss was around 6-dB per facet.

A.2 Directional Coupler : Working principle

The directional coupler design used in this thesis has been adopted from the PhD thesis of Ramesh [126]. Directional coupler is a 2 $\times$ 2 passive power coupling/splitting device consisting of two waveguides spaced closely to each other as shown in Figure A.2. Depending on the length of the coupling region (L_{DC}) and the gap between the two

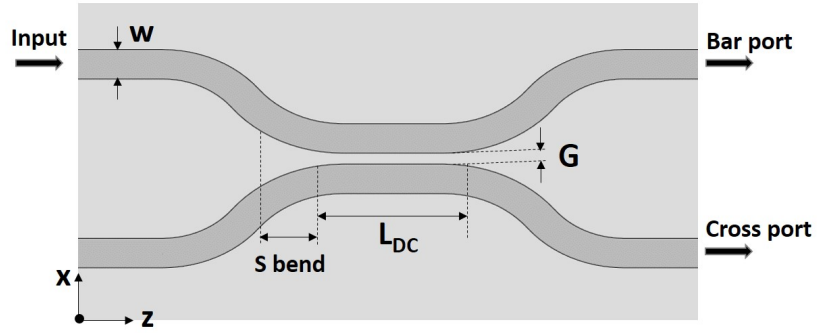

Figure A.2: Schematic 2D illustration of the directional coupler in SOI.

waveguides (G), exchange of power happens between the guided modes of the two adjacent waveguides. The coupling of modes between the two parallel waveguides can be explained either using coupled-mode theory or super-mode theory [129]. In super-mode analysis, the coupled waveguides are considered as a composite structure that can support higher order modes. In a coupled waveguide system, if the two single mode waveguides are identical, the evanescent fields of the guided modes in the gap overlap with each other and two supermodes are formed: symmetric (fundamental mode) and anti-symmetric modes (first order mode), which can be expressed as

$$E_s(x, y, z) = E_s(x, y)e^{(j\beta_s z)} \tag{A.2}$$

$$E_a(x, y, z) = E_a(x, y)e^{(j\beta_a z)} \tag{A.3}$$

where E_s and E_a are the electric field profiles of the symmetric supermode and anti-symmetric supermode respectively with propagation constants β_s and β_a given by

$$\beta_s = \frac{2\pi}{\lambda} n^s_{eff}(\lambda) \qquad \beta_a = \frac{2\pi}{\lambda} n^a_{eff}(\lambda) \tag{A.4}$$

Since $n^a_{eff} > n^s_{eff}$, both the modes travel with different phase velocities and the phase difference between them, $\Delta\Phi = (\beta_s - \beta_a)z$ determines the fraction of power coupled from one waveguide to another at any distance z.

$$P_b(\lambda) = cos^2\kappa L_{DC} \cdot P_{in}(\lambda) = |t|^2(\lambda) \tag{A.5}$$

$$P_c(\lambda) = sin^2\kappa L_{DC} \cdot P_{in}(\lambda) = |k|^2(\lambda) \tag{A.6}$$

where t is the self coupling coefficient and k is the cross coupling coefficient expressed as

$$t = cos(\kappa L_{DC}) \qquad k = e^{-j\pi/2} sin(\kappa L_{DC}) \tag{A.7}$$

where $e^{-j\pi/2}$ denotes the phase difference between the field amplitudes. The coupling strength κ, which is defined as the fraction of electric field amplitude per unit length exchanged between the waveguides is expressed as

$$\kappa(\lambda) = \frac{\beta_s(\lambda) - \beta_a(\lambda)}{2} = \frac{\pi\Delta n(\lambda)}{\lambda} \tag{A.8}$$

In general, the transfer function of a 2 × 2 DC is expressed as

$$T_{DC}(\lambda) = \begin{bmatrix} cos[\kappa(\lambda)L_{DC}] & -jsin[\kappa(\lambda)L_{DC}] \\ -jsin[\kappa(\lambda)L_{DC}] & cos[\kappa(\lambda)L_{DC}] \end{bmatrix} \tag{A.9}$$

and the 3-dB coupling length of the DC is given by

$$L_{3dB}(\lambda) = \frac{(2m+1)\pi}{4\kappa(\lambda)} \tag{A.10}$$

where m = 0,1,2,3... The value of $\Delta\Phi(\lambda)$ can be engineered appropriately by optimizing the waveguide parameters.

A.2.1 Condition for wavelength independent coupling

The free spectral range (FSR) of the transmitted waves at the bar and cross port can be derived from Eq. A.4 and A.5 as

$$\Delta\lambda = \frac{-\lambda^2}{L_{DC}\Delta n_g} \tag{A.11}$$

where

$$\Delta n_g(\lambda) = \Delta n(\lambda) - \lambda\frac{d}{d\lambda}[\Delta n(\lambda)] \tag{A.12}$$

where Δn_g is the differential group index of the supermodes. If a DC is designed such that the differential group index is 0, the FSR becomes infinity, i.e. DC will exhibit wavelength independent transmission characteristics. In other words,

$$\frac{d\kappa(\lambda)}{d\lambda} = -\frac{\pi}{\lambda^2}\Delta n_g(\lambda) \sim 0 \tag{A.13}$$

Hence the condition for WIDC is given by

$$\Delta n_g(\lambda) = 0 \Rightarrow \kappa(\lambda) \text{ constant for all } \lambda\text{s} \tag{A.14}$$

Using the above equations, the WIDC with optimized waveguide parameters (W = 350 nm; h = 160 nm) on a 220 nm SOI exhibits broadband uniform coupling over a

wavelength range 1525 nm $\leq \lambda$ 1625 nm. for TE polarization. The 3-dB coupling length was designed to be L_{DC} = 4 μm. In addition to the DC design, one needs to take care of the bend-induced losses and additional coupling incurred by the S- bends also. The proposed WIDC geometry is designed with S-bends of radius 180 μm to suppress the effect of bend region in coupling length and coupling characteristics.

APPENDIX B

Effective medium theory for SWG waveguides

Light propagation in a sub-wavelength periodic structure can be described by the effective medium theory according to which different materials periodically arranged at a sub-wavelength scale can be approximated as a homogeneous effective medium [72]. Consider a SWG waveguide comprising of alternating layers of materials with refractive indices n_1 and n_2 respectively. The periodicity Λ is designed to be $\Lambda < \lambda$ (max n_1, n_2)) which ensures the suppression of incident light (of wavelength λ) diffraction independent of the angle of incidence. The effective refractive index of a wave with electric field parallel to the plane of incidence (TE polarization),is approximated as

$$n_{||} = (f n_1^2 + (1-f) n_2^2)^{1/2} \tag{B.1}$$

and electric field perpendicular to the plane of incidence (TM polarization),

$$n_{\perp} = (f n_1^{-2} + (1-f) n_2^{-2})^{-1/2} \tag{B.2}$$

where $f = a/\Lambda$ is the volume fraction of the material with index n_1. The effective refractive index of the guided mode in a SWG waveguide is thus a polarization dependent weighted average of the bulk indices of the constituent materials.

APPENDIX C

Additional Information on Fabrication

C.1 Silicon Cleaning Procedure

Table C.1: Standard silicon cleaning procedure

Steps	Chemical used	Procedure
Organic impurities removal	Trichloroethylene	▷ Ultrasonic agitation for 2 minutes ▷ Heating at 80 °C till bubbles come
TCE residues removal	Acetone	▷ Ultrasonic agitation for 2 minutes ▷ Heating at 80 °C till bubbles come ▷ Rinse under running DI water ▷ Blow dry with nitrogen gas
Oxide layer formation	Nitric acid	▷ Heating at 60 °C till fumes come ▷ Rinse under running DI water ▷ Blow dry with nitrogen gas
Oxide layer removal	HF	▷ Dip in dilute HF (HF:DI water::1:10) for 40 seconds ▷ Rinse under running DI water ▷ Blow dry with nitrogen gas

C.2 Spin coating procedure

1. Dehydrate the SOI sample over a hot plate at 180^0C for 10 minutes. Let the sample cool down to room temperature.
2. Place the sample over the vacuum chuck in the spin coating unit and do a dummy run with the optimized coating parameters.
3. Blow dry the sample with nitrogen air-gun to remove any dust remaining on the sample

4. Pour 3-4 drops of resist (HSQ/PMMA) on to the sample using a fresh syringe and filter if required.
5. Once the spin coating is over, remove the resist using Acetone from the corner of the sample which is to be clamped on the sample holder. This is to ensure proper conductivity between the sample and the clamp.
6. Prebake the sample on a hot-plate at 180^0C for 2 minutes.

C.3 Electron beam lithography : Writing strategies

Raith-150 TWO electron-beam lithography system facilitates two patterning techniques: (a) Conventional patterning and (b) Fixed Beam Moving Stage (FBMS) patterning.

C.3.1 Conventional patterning

Here, the patterning area is divided into small squares called write fields and the patterns are written in each write field in a sequential order. The stage which holds the sample is positioned such that the electron gun is fixed at the middle of the first write field and the electron beam deflects throughout the write field area. The stage then moves to position the next write field below the electron gun and the patterning continues in a sequential manner. The main drawback of this patterning technique is that a small misalignment in the stage positioning between adjacent write-fields may cause stitching error between the write fields. Practically, there will always be a positioning error of $\pm$ 100 nm which makes it unsuitable for patterning long structures such as waveguides which have lengths in the order of millimeters. This issue can be overcome using FBMS technique.

C.3.2 Fixed Beam Moving Stage

In FBMS patterning technique, the beam remains fixed and the stage moves continuously as per the mask design. This facilitates stitch-free patterning of longer structures. The width of the FBMS line can be predefined though it cannot be changed within a

single component. The photonic waveguides, which span to several millimeters are often defined as FBMS paths since their width remains the same throughout. Aligning the FBMS patterns with the conventional patterns is critical due to the stage positioning error which is inevitable.

C.4 Micro-heater fabrication details

The microheaters were defined in two cycles of metalization followed by lift-off processes: aluminum for the contact pads and titanium for the heaters [126]. The windows for the contact pads and micro-heaters were defined using EBL. Aluminum was deposited using thermal evaporation technique whereas titanium was deposited by electron beam evaporation technique. The details of the process steps are given below:

C.4.1 Aluminium contact pad integration

1. **Resist coating:** For opening the windows for metalization, positive PMMA A8 resist was spun coat on the SOI substrate which already contained the passive devices. The spin coating parameters used are given in Table C.2.

Table C.2: Optimized spin coating parameters of PMMA A-8 resist to obtain 300 nm resist thickness

Spin parameters	Thickness
Speed : 600 rpm Acceleration : 7000 rpm/s Time : 40 s	300 nm

2. **Electron beam lithography**: Windows for the Aluminium contact pads (250 μm $\times$ 200 μm) are patterned over the PMMA A-8 resist using Electron beam lithography (Raith 150 TWO) and developed using MIBK:IPA developer solution. The optimized patterning and developing parameters are given in Table C.3.

3. **Aluminium deposition**: Aluminium layer of about 100 nm thickness was deposited over the sample using thermal evaporation unit (HPVT-305G).

4. **Lift-off process:** Aluminium is lifted off along with the underlying resist layer from regions outside the windows by ultrasonic agitation in Acetone at 60^0C for 10 minutes followed by cleaning in DI water.

Table C.3: Optimized EBL parameters for patterning and developing the windows for the contact pads and microheaters

Column parameters	Patterning/Developing parameters
Acceleration voltage : 20 kV Aperture : 30 μm Working distance : 10 mm Write field : 100 μm $\times$ 100 μm	Area dose : 150 μC/cm^2 Development : 30 sec in MIBK:IPA (1:3) and 10 sec in IPA

C.4.2 Titanium microheater integration

The resist coating and the lithography parameters used for patterning Titanium microheater lines are the same as those used for Aluminium contact pads, as detailed in Table C.2 and Table C.3. However, thermal evaporation was used to deposit Titanium (Hind Hi Vac BC 300T) of $\sim$ 80 nm thickness. The lift-off process was carried out using ultrasonic agitation in Acetone at 60^0C for 2 minutes. Ample care was taken to prevent the re-deposition of Titanium metal flakes over the devices.

APPENDIX D

DOCTORAL COMMITTEE

CHAIR PERSON : Prof. Anil Prabhakar

Professor
Department of Electrical Engineering
Indian Institute of Technology, Madras

GUIDE : Prof. Bijoy Krishna Das

Professor
Department of Electrical Engineering
Indian Institute of Technology, Madras

CO-GUIDE : Prof. Nandita DasGupta

Professor
Department of Electrical Engineering
Indian Institute of Technology, Madras

MEMBERS : Prof. Enakshi Bhattacharya

Professor

Department of Electrical Engineering

Indian Institute of Technology, Madras

: Dr. Ananth Krishnan

Assistant Professor

Department of Electrical Engineering

Indian Institute of Technology, Madras

: Dr. Manu Jaiswal

Assistant Professor

Department of Physics

Indian Institute of Technology, Madras

APPENDIX E

List of Publications Based on Thesis

Journals

1. **Sumi R.**, N DasGupta and B. K. Das, "Integrated optical linear edge filter using apodized sub-wavelength grating waveguide in SOI", IEEE Photonics Technology Letters, Vol. 31, No. 17, pp. 1449 - 1452, September 2019.

2. **Sumi R.**, R. K. Gupta, N DasGupta and B. K. Das, "Ultra Broadband Add-Drop Filter/Switch Circuit using Sub-Wavelength Grating Waveguides", IEEE Journal of Selected Topics in Quantum Electronics (2019), Vol. 25, No. 3, pp. 1 - 11, May/June 2019.

3. B. K. Das, N. DasGupta, S. Chandran, S. Kurudi, P. Sah, R. Nandi, R. K. Gupta, **Sumi R.**, et. al, "Silicon Photonics Technology : Ten Years of Research at IIT Madras", Asian Journal of Physics, Vol. 25, No. 7, pp. 923 - 955, 2016.

Conference (Presentations / Proceedings/Symposium)

1. Meena B, **Sumi R.** and B. K. Das, "Fabry-perot cavity resonances in apodized sub-wavelength grating waveguides.", International Conference on Fibre Optics and Photonics, Optical Society of America, 12-15 December 2018, Delhi, India (poster).

2. **Sumi R.**, Nandita DasGupta, and Bijoy K Das, "Integrated optical edge filter using apodized sub-wavelength grating waveguide in SOI, European Conference on Integrated Optics (ECIO-2018), May 30 - June 1 2018, Valencia, Spain (poster)

3. **Sumi R**, R K Gupta, Nandita DasGupta, and Bijoy K Das, "Integrated Optical Ultra-Broadband Add-Drop Filter in Silicon-On-Insulator Platform." Optical Fiber Communications Conference and Exposition (OFC), Optical Society of America, 11 - 15 March 2018, San Diego, USA (oral).

4. **Sumi R.**, Nandita DasGupta, and Bijoy K Das, "Integrated optical Mach-Zehnder interferometer with a sensing arm of sub-wavelength grating waveguide in SOI, IEEE Sensors - 2017, October 29 - November 1 2017, Glasgow, UK (poster).

5. **Sumi R.**, Nandita DasGupta, and Bijoy K Das, "Integrated silicon photonics periodic nanostructures for sensing applications", Symposium on Photonic Crystals: 30 Years of Photonic Crystals - the Indian Scenario, 21 - 23 September 2017, IIT Kanpur (poster).

6. **Sumi R.**, P. Sah, and Bijoy K Das, "Integrated 1D photonic crystal devices with SOI waveguides", Symposium on Photonic Crystals: 30 Years of Photonic Crystals - the Indian Scenario, 21 - 23 September 2017, IIT Kanpur (invited).

7. **Sumi R.**, Nandita DasGupta, and Bijoy K Das, " Demonstration of integrated optical 2D photonic crystal waveguides in SOI for sensing applications.", International Conference on Fibre Optics and Photonics, Optical Society of America, 04 - 08 December 2016, Kanpur, India (oral).

REFERENCES

[1] L. Vivien and L. Pavesi, *Handbook of Silicon Photonics*. Taylor & Francis, 2016.

[2] S. Latkowski and D. Lenstra, "Lasers in inp generic photonic integration technology platforms," *Advanced Optical Technologies*, vol. 4, no. 2, pp. 179–188, 2015.

[3] C. Wang, M. Zhang, X. Chen, M. Bertrand, A. Shams-Ansari, S. Chandrasekhar, P. Winzer, and M. Lončar, "Integrated lithium niobate electro-optic modulators operating at CMOS-compatible voltages," *Nature*, vol. 562, no. 7725, p. 101, 2018.

[4] A. Rao and S. Fathpour, "Compact lithium niobate electrooptic modulators," *IEEE Journal of Selected Topics in Quantum Electronics*, vol. 24, no. 4, pp. 1–14, 2018.

[5] A. Boes, B. Corcoran, L. Chang, J. Bowers, and A. Mitchell, "Status and potential of lithium niobate on insulator (lnoi) for photonic integrated circuits," *Laser & Photonics Reviews*, vol. 12, no. 4, p. 1700256, 2018.

[6] J. Wang and S. Lee, "Ge-photodetectors for si-based optoelectronic integration," *Sensors*, vol. 11, no. 1, pp. 696–718, 2011.

[7] D. Marris-Morini, V. Vakarin, J. M. Ramirez, Q. Liu, A. Ballabio, J. Frigerio, M. Montesinos, C. Alonso-Ramos, X. Le Roux, S. Serna, D. Benedikovic, D. Chrastina, L. Vivien, and G. Isella, "Germanium-based integrated photonics from near-to mid-infrared applications," *Nanophotonics*, vol. 7, no. 11, pp. 1781–1793, 2018.

[8] R. Soref and J. Lorenzo, "Single-crystal silicon: a new material for 1.3 and 1.6 μm integrated-optical components," *Electronics Letters*, vol. 21, no. 21, pp. 953–954, 1985.

[9] R. Soref and J. Larenzo, "All-silicon active and passive guided-wave components for λ= 1.3 and 1.6 μm," *IEEE Journal of Quantum Electronics*, vol. 22, no. 6, pp. 873–879, 1986.

[10] R. A. Soref, D. McDaniel, and B. R. Bennett, "Guided-wave intensity modulators using amplitude-and-phase perturbations," *Journal of Lightwave Technology*, vol. 6, no. 3, pp. 437–444, 1988.

[11] G. Abstreiter, "Engineering the future of electronics," *Physics World*, vol. 5, no. 3, p. 36, 1992.

[12] R. A. Soref, "Silicon-based optoelectronics," *Proceedings of the IEEE*, vol. 81, no. 12, pp. 1687–1706, 1993.

[13] D. Albares and R. Soref, "Silicon-on-sapphire waveguides," in *Integrated Optical Circuit Engineering IV*, vol. 704. International Society for Optics and Photonics, 1987, pp. 24–26.

[14] R. Soref, F. Namavar, and J. Lorenzo, "Optical waveguiding in a single-crystal layer of germanium silicon grown on silicon," *Optics Letters*, vol. 15, no. 5, pp. 270–272, 1990.

[15] B. N. Kurdi and D. G. Hall, "Optical waveguides in oxygen-implanted buried-oxide silicon-on-insulator structures," *Optics Letters*, vol. 13, no. 2, pp. 175–177, 1988.

[16] J. Schmidtchen, A. Splett, B. Schuppert, K. Petermann, and G. Burbach, "Low loss singlemode optical waveguides with large cross-section in silicon-on-insulator," *Electronics Letters*, vol. 27, no. 16, pp. 1486–1488, 1991.

[17] X. Zheng, E. Chang, P. Amberg, I. Shubin, J. Lexau, F. Liu, H. Thacker, S. S. Djordjevic, S. Lin, Y. Luo, J. Yao, J.-H. Lee, K. Raj, R. Ho, J. E. Cunningham, and A. V. Krishnamoorthy, "A high-speed, tunable silicon photonic ring modulator integrated with ultra-efficient active wavelength control," *Optics Express*, vol. 22, no. 10, pp. 12 628–12 633, 2014.

[18] B. Milivojevic, C. Raabe, A. Shastri, M. Webster, P. Metz, S. Sunder, B. Chattin, S. Wiese, B. Dama, and K. Shastri, "112gb/s dp-qpsk transmission over 2427km ssmf using small-size silicon photonic iq modulator and low-power cmos driver," in *Optical Fiber Communication Conference*. Optical Society of America, 2013, pp. OTh1D–1.

[19] D. Pérez-Galacho, D. Marris-Morini, R. Stoffer, E. Cassan, C. Baudot, T. Korthorst, F. Boeuf, and L. Vivien, "Simplified modeling and optimization of silicon modulators based on free-carrier plasma dispersion effect," *Optics Express*, vol. 24, no. 23, pp. 26 332–26 337, 2016.

[20] M. Douix, D. Marris-Morini, C. Baudot, S. Crémer, D. Rideau, D. Perez-Galacho, A. Souhaité, R. Blanc, E. Batail, N. Vulliet *et al.*, "Design of integrated capacitive modulators for 56 Gbps operation," in *Group IV Photonics (GFP), 2016 IEEE 13th International Conference on*. IEEE, 2016, pp. 5–7.

[21] R. Soref and J. Hendrickson, "Proposed ultralow-energy dual photonic-crystal nanobeam devices for on-chip n x n switching, logic, and wavelength multiplexing," *Optics Express*, vol. 23, no. 25, pp. 32 582–32 596, 2015.

[22] G. de Valicourt, S. Chandrasekhar, S. Randel, Y.-K. Chen, M. Mestre, Y. Pointurier, S. Bigo, J.-M. Fedeli, L. Bramerie, J.-C. Simon *et al.*, "16-channel 100 GHz-spaced integrated polarization diversity silicon-based slot-blocker for high data rate reconfigurable networks," in *Optical Fiber Communications Conference and Exhibition (OFC), 2016*. IEEE, 2016, pp. 1–3.

[23] J. R. Hendrickson, R. Soref, and R. Gibson, "Improved $2\times$ 2 Mach-Zehnder switching using coupled-resonator photonic-crystal nanobeams," *Optics Letters*, vol. 43, no. 2, pp. 287–290, 2018.

[24] Q. Huang, K. Jie, Q. Liu, Y. Huang, Y. Wang, and J. Xia, "Ultra-compact, broadband tunable optical bandstop filters based on a multimode one-dimensional photonic crystal waveguide," *Optics Express*, vol. 24, no. 18, pp. 20 542–20 553, 2016.

[25] C. Sun, M. T. Wade, Y. Lee, J. S. Orcutt, L. Alloatti, M. S. Georgas, A. S. Waterman, J. M. Shainline, R. R. Avizienis, S. Lin *et al.*, "Single-chip microprocessor that communicates directly using light," *Nature*, vol. 528, no. 7583, pp. 534–538, 2015.

[26] A. H. Atabaki, S. Moazeni, F. Pavanello, H. Gevorgyan, J. Notaros, L. Alloatti, M. T. Wade, C. Sun, S. A. Kruger, H. Meng *et al.*, "Integrating photonics with silicon nanoelectronics for the next generation of systems on a chip," *Nature*, vol. 556, no. 7701, p. 349, 2018.

[27] J. Wang, S. Paesani, Y. Ding, R. Santagati, P. Skrzypczyk, A. Salavrakos, J. Tura, R. Augusiak, L. Mančinska, D. Bacco *et al.*, "Multidimensional quantum entanglement with large-scale integrated optics," *Science*, vol. 360, no. 6386, pp. 285–291, 2018.

[28] D. A. Miller, "Device requirements for optical interconnects to silicon chips," *Proceedings of the IEEE*, vol. 97, no. 7, pp. 1166–1185, 2009.

[29] [Online]. Available: http://www.intel.com

[30] [Online]. Available: http://www.acacia.com

[31] K. Zinoviev, L. G. Carrascosa, J. Sánchez del Río, B. Sepúlveda, C. Domínguez, and L. M. Lechuga, "Silicon photonic biosensors for lab-on-a-chip applications," *Advances in Optical Technologies*, vol. 2008, 2008.

[32] D.-X. Xu, A. Densmore, P. Cheben, M. Vachon, R. Ma, S. Janz, A. Delâge, J. Schmid, J. Lapointe, Y. Li *et al.*, "Silicon photonic wire devices for biosensing and communications," in *Asia Communications and Photonics Conference and Exhibition*. IEEE, 2010, pp. 52–53.

[33] E. Luan, H. Shoman, D. Ratner, K. Cheung, and L. Chrostowski, "Silicon photonic biosensors using label-free detection," *Sensors*, vol. 18, no. 10, p. 3519, 2018.

[34] V. M. Lavchiev, B. Jakoby, U. Hedenig, T. Grille, P. Irsigler, G. Ritchie, J. Kirkbride, and B. Lendl, "Silicon photonics in the mid-infrared: Waveguide absorption sensors," in *SENSORS, 2014 IEEE*. IEEE, 2014, pp. 645–648.

[35] T. Wall, J. McMurray, G. Meena, V. Ganjalizadeh, H. Schmidt, and A. Hawkins, "Optofluidic lab-on-a-chip fluorescence sensor using integrated buried arrow (barrow) waveguides," *Micromachines*, vol. 8, no. 8, p. 252, 2017.

[36] L. Liu, X. Zhou, J. S. Wilkinson, P. Hua, B. Song, and H. Shi, "Integrated optical waveguide-based fluorescent immunosensor for fast and sensitive detection of microcystin-lr in lakes: Optimization and analysis," *Scientific reports*, vol. 7, no. 1, p. 3655, 2017.

[37] J. G. Wangüemert-Pérez, A. Hadij-ElHouati, A. Sánchez-Postigo, J. Leuermann, D.-X. Xu, P. Cheben, A. Ortega-Moñux, R. Halir, and Í. Molina-Fernández, "Subwavelength structures for silicon photonics biosensing," *Optics & Laser Technology*, vol. 109, pp. 437–448, 2019.

[38] G. A. Rodriguez, S. Hu, and S. M. Weiss, "Porous silicon ring resonator for compact, high sensitivity biosensing applications," *Optics Express*, vol. 23, no. 6, pp. 7111–7119, 2015.

[39] S. Chandran, R. K. Gupta, and B. K. Das, "Dispersion enhanced critically coupled ring resonator for wide range refractive index sensing," *IEEE Journal of Selected Topics in Quantum Electronics*, vol. 23, no. 2, pp. 1–9, 2017.

[40] S. M. Grist, S. A. Schmidt, J. Flueckiger, V. Donzella, W. Shi, S. T. Fard, J. T. Kirk, D. M. Ratner, K. C. Cheung, and L. Chrostowski, "Silicon photonic microdisk resonators for label-free biosensing," *Optics express*, vol. 21, no. 7, pp. 7994–8006, 2013.

[41] S. Chakravarty, Y. Zou, W.-C. Lai, and R. T. Chen, "Slow light engineering for high Q high sensitivity photonic crystal microcavity biosensors in silicon," *Biosensors and Bioelectronics*, vol. 38, no. 1, pp. 170–176, 2012.

[42] P. Prabhathan, V. Murukeshan, Z. Jing, and P. V. Ramana, "Compact SOI nanowire refractive index sensor using phase shifted Bragg grating," *Optics Express*, vol. 17, no. 17, pp. 15 330–15 341, 2009.

[43] J. Zhou, Y. Wang, C. Liao, B. Sun, J. He, G. Yin, S. Liu, Z. Li, G. Wang, X. Zhong *et al.*, "Intensity modulated refractive index sensor based on optical fiber michelson interferometer," *Sensors and Actuators B: Chemical*, vol. 208, pp. 315–319, 2015.

[44] A. Rickman, G. Reed, and F. Namavar, "Silicon-on-insulator optical rib waveguide loss and mode characteristics," *Journal of Lightwave Technology*, vol. 12, no. 10, pp. 1771–1776, 1994.

[45] V. R. Almeida, Q. Xu, C. A. Barrios, and M. Lipson, "Guiding and confining light in void nanostructure," *Optics Letters*, vol. 29, no. 11, pp. 1209–1211, 2004.

[46] P. Müllner and R. Hainberger, "Structural optimization of silicon-on-insulator slot waveguides," *IEEE Photonics Technology Letters*, vol. 18, no. 24, pp. 2557–2559, 2006.

[47] C. Koos, L. Jacome, C. Poulton, J. Leuthold, and W. Freude, "Nonlinear silicon-on-insulator waveguides for all-optical signal processing," *Optics Express*, vol. 15, no. 10, 2007.

[48] C. Koos, P. Vorreau, T. Vallaitis, P. Dumon, W. Bogaerts, R. Baets, B. Esembeson, I. Biaggio, T. Michinobu, F. Diederich *et al.*, "All-optical high-speed signal processing with silicon–organic hybrid slot waveguides," *Nature Photonics*, vol. 3, no. 4, p. 216, 2009.

[49] L. Shen, Z. Ruan, S. Zheng, A. Wang, J. Liu, S. Li, and J. Wang, "Experimental demonstration of silicon strip and slot waveguides for 2 μm chip-scale optical data transmission," in *CLEO: QELS_Fundamental Science*. Optical Society of America, 2017, pp. JW2A–131.

[50] T. Claes, J. G. Molera, K. De Vos, E. Schacht, R. Baets, and P. Bienstman, "Label-free biosensing with a slot-waveguide-based ring resonator in silicon on insulator," *IEEE Photonics Journal*, vol. 1, no. 3, pp. 197–204, 2009.

[51] W. Zhang, S. Serna, X. Le Roux, C. Alonso-Ramos, L. Vivien, and E. Cassan, "Analysis of silicon-on-insulator slot waveguide ring resonators targeting high q-factors," *Optics Letters*, vol. 40, no. 23, pp. 5566–5569, 2015.

[52] W. Zhang, S. Serna, X. Le Roux, L. Vivien, and E. Cassan, "Highly sensitive refractive index sensing by fast detuning the critical coupling condition of slot waveguide ring resonators," *Optics Letters*, vol. 41, no. 3, pp. 532–535, 2016.

[53] A. Bera, M. Kuittinen, S. Honkanen, and M. Roussey, "Silicon slot waveguide fano resonator," *Optics Letters*, vol. 43, no. 15, pp. 3489–3492, 2018.

[54] E. Yablonovitch, "Inhibited spontaneous emission in solid-state physics and electronics," *Physical review Letters*, vol. 58, no. 20, p. 2059, 1987.

[55] S. John, "Strong localization of photons in certain disordered dielectric superlattices," *Physical Review Letters*, vol. 58, no. 23, p. 2486, 1987.

[56] J. D. Joannopoulos, P. R. Villeneuve, and S. Fan, "Photonic crystals: putting a new twist on light," *Nature*, vol. 386, no. 6621, p. 143, 1997.

[57] A. Scherer, O. Painter, J. Vuckovic, M. Loncar, and T. Yoshie, "Photonic crystals for confining, guiding, and emitting light," *IEEE Transactions on nanotechnology*, vol. 99, no. 1, pp. 4–11, 2002.

[58] J. D. Joannopoulos, S. G. Johnson, J. N. Winn, and R. D. Meade, *Photonic crystals: molding the flow of light*. Princeton university press, 2011.

[59] M. Notomi, "Strong light confinement with periodicity," *Proceedings of the IEEE*, vol. 99, no. 10, pp. 1768–1779, 2011.

[60] R. Costa, A. Melloni, and M. Martinelli, "Bandpass resonant filters in photonic-crystal waveguides," *IEEE Photonics Technology Letters*, vol. 15, no. 3, pp. 401–403, 2003.

[61] X. Ge, Y. Shi, and S. He, "Ultra-compact channel drop filter based on photonic crystal nanobeam cavities utilizing a resonant tunneling effect," *Optics Letters*, vol. 39, no. 24, pp. 6973–6976, 2014.

[62] M. Gay, L. Bramerie, L. A. Neto, S. D. Le, J.-C. Simon, C. Peucheret, Z. Han, X. Checoury, G. Moille, J. Bourderionnet *et al.*, "Silicon-on-insulator rf filter based on photonic crystal functions for channel equalization," *IEEE Photonics Technology Letters*, vol. 28, no. 23, pp. 2756–2759, 2016.

[63] W.-C. Lai, S. Chakravarty, X. Wang, C. Lin, and R. T. Chen, "On-chip methane sensing by near-ir absorption signatures in a photonic crystal slot waveguide," *Optics Letters*, vol. 36, no. 6, pp. 984–986, 2011.

[64] B. Troia, A. Paolicelli, F. De Leonardis, and V. M. Passaro, "Photonic crystals for optical sensing: A review," in *Advances in Photonic Crystals*. InTech, 2013.

[65] Y. Liu and H. Salemink, "All-optical on-chip sensor for high refractive index sensing in photonic crystals," *EPL (Europhysics Letters)*, vol. 107, no. 3, p. 34008, 2014.

[66] R. Sumi, N. DasGupta, and B. K. Das, "Demonstration of integrated optical 2d photonic crystal waveguides in SOI for sensing applications," in *International Conference on Fibre Optics and Photonics*. Optical Society of America, 2016, pp. W4E–2.

[67] W. Jiang, L. Gu, X. Chen, and R. T. Chen, "Photonic crystal waveguide modulators for silicon photonics: Device physics and some recent progress," *Solid-State Electronics*, vol. 51, no. 10, pp. 1278–1286, 2007.

[68] Y. Terada, K. Kondo, R. Abe, and T. Baba, "Full c-band si photonic crystal waveguide modulator," *Optics Letters*, vol. 42, no. 24, pp. 5110–5112, 2017.

[69] A. Melloni, A. Canciamilla, C. Ferrari, F. Morichetti, L. O'Faolain, T. Krauss, R. De La Rue, A. Samarelli, and M. Sorel, "Tunable delay lines in silicon photonics: coupled resonators and photonic crystals, a comparison," *IEEE Photonics Journal*, vol. 2, no. 2, pp. 181–194, 2010.

[70] J. Adachi, N. Ishikura, H. Sasaki, and T. Baba, "Wide range tuning of slow light pulse in SOI photonic crystal coupled waveguide via folded chirping," *IEEE Journal of Selected Topics in Quantum Electronics*, vol. 16, no. 1, pp. 192–199, 2010.

[71] C.-J. Chung, X. Xu, G. Wang, Z. Pan, and R. T. Chen, "On-chip optical true time delay lines featuring one-dimensional fishbone photonic crystal waveguide," *Applied Physics Letters*, vol. 112, no. 7, p. 071104, 2018.

[72] S. Rytov, "Electromagnetic properties of a finely stratified medium," *Soviet Physics JEPT*, vol. 2, pp. 466–475, 1956.

[73] P. Lalanne and D. Lemercier-Lalanne, "On the effective medium theory of subwavelength periodic structures," *Journal of Modern Optics*, vol. 43, no. 10, pp. 2063–2085, 1996.

[74] P. Lalanne and J.-P. Hugonin, "High-order effective-medium theory of subwavelength gratings in classical mounting: application to volume holograms," *JOSA A*, vol. 15, no. 7, pp. 1843–1851, 1998.

[75] M. W. Farn, "Binary gratings with increased efficiency," *Applied Ooptics*, vol. 31, no. 22, pp. 4453–4458, 1992.

[76] P. Cheben, S. Janz, D.-X. Xu, B. Lamontagne, A. Delâge, and S. Tanev, "A broad-band waveguide grating coupler with a subwavelength grating mirror," *IEEE Photonics Technology Letters*, vol. 18, no. 1, pp. 13–15, 2006.

[77] R. Halir, P. J. Bock, P. Cheben, A. Ortega-Moñux, C. Alonso-Ramos, J. H. Schmid, J. Lapointe, D.-X. Xu, J. G. Wangüemert-Pérez, Í. Molina-Fernández *et al.*, "Waveguide sub-wavelength structures: a review of principles and applications," *Laser & Photonics Reviews*, vol. 9, no. 1, pp. 25–49, 2015.

[78] P. J. Bock, P. Cheben, J. H. Schmid, J. Lapointe, A. Delage, S. Janz, G. C. Aers, D.-X. Xu, A. Densmore, and T. J. Hall, "Subwavelength grating periodic structures in silicon-on-insulator: a new type of microphotonic waveguide," *Optics Express*, vol. 18, no. 19, pp. 20 251–20 262, 2010.

[79] P. J. Bock, P. Cheben, J. H. Schmid, J. Lapointe, A. Delâge, D.-X. Xu, S. Janz, A. Densmore, and T. J. Hall, "Subwavelength grating crossings for silicon wire waveguides," *Optics Express*, vol. 18, no. 15, pp. 16 146–16 155, 2010.

[80] W. Bogaerts, P. Dumon, D. Van Thourhout, and R. Baets, "Low-loss, low-cross-talk crossings for silicon-on-insulator nanophotonic waveguides," *Optics Letters*, vol. 32, no. 19, pp. 2801–2803, 2007.

[81] P. Sanchis, P. Villalba, F. Cuesta, A. Håkansson, A. Griol, J. V. Galán, A. Brimont, and J. Martí, "Highly efficient crossing structure for silicon-on-insulator waveguides," *Optics Letters*, vol. 34, no. 18, pp. 2760–2762, 2009.

[82] R. Halir, P. Cheben, J. Schmid, R. Ma, D. Bedard, S. Janz, D.-X. Xu, A. Densmore, J. Lapointe, and I. Molina-Fernández, "Continuously apodized fiber-to-chip surface grating coupler with refractive index engineered subwavelength structure," *Optics Letters*, vol. 35, no. 19, pp. 3243–3245, 2010.

[83] Z. Cheng, X. Chen, C. Wong, K. Xu, C. K. Fung, Y. Chen, and H. K. Tsang, "Focusing subwavelength grating coupler for mid-infrared suspended membrane waveguide," *Optics Letters*, vol. 37, no. 7, pp. 1217–1219, 2012.

[84] X. Xu, H. Subbaraman, J. Covey, D. Kwong, A. Hosseini, and R. T. Chen, "Complementary metal–oxide–semiconductor compatible high efficiency subwavelength grating couplers for silicon integrated photonics," *Applied Physics Letters*, vol. 101, no. 3, p. 031109, 2012.

[85] Z. Cheng, X. Chen, C. Y. Wong, K. Xu, and H. K. Tsang, "Apodized focusing subwavelength grating couplers for suspended membrane waveguides," *Applied Physics Letters*, vol. 101, no. 10, p. 101104, 2012.

[86] X. Chen, K. Xu, Z. Cheng, C. K. Fung, and H. K. Tsang, "Wideband subwavelength gratings for coupling between silicon-on-insulator waveguides and optical fibers," *Optics Letters*, vol. 37, no. 17, pp. 3483–3485, 2012.

[87] Y. Ding, H. Ou, and C. Peucheret, "Ultrahigh-efficiency apodized grating coupler using fully etched photonic crystals," *Optics Letters*, vol. 38, no. 15, pp. 2732–2734, 2013.

[88] Y. Wang, X. Wang, J. Flueckiger, H. Yun, W. Shi, R. Bojko, N. A. Jaeger, and L. Chrostowski, "Focusing sub-wavelength grating couplers with low back reflections for rapid prototyping of silicon photonic circuits," *Optics Express*, vol. 22, no. 17, pp. 20 652–20 662, 2014.

[89] Y. Wang, W. Shi, X. Wang, Z. Lu, M. Caverley, R. Bojko, L. Chrostowski, and N. A. Jaeger, "Design of broadband subwavelength grating couplers with low back reflection," *Optics Letters*, vol. 40, no. 20, pp. 4647–4650, 2015.

[90] P. J. Bock, P. Cheben, J. H. Schmid, A. Delâge, D.-X. Xu, S. Janz, and T. J. Hall, "Sub-wavelength grating mode transformers in silicon slab waveguides," *Optics Express*, vol. 17, no. 21, pp. 19 120–19 133, 2009.

[91] P. Cheben, D.-X. Xu, S. Janz, and A. Densmore, "Subwavelength waveguide grating for mode conversion and light coupling in integrated optics," *Optics Express*, vol. 14, no. 11, pp. 4695–4702, 2006.

[92] Z. Ruan, L. Shen, S. Zheng, and J. Wang, "Subwavelength grating slot (swgs) waveguide on silicon platform," *Optics Express*, vol. 25, no. 15, pp. 18 250–18 264, 2017.

[93] H. Yun, Y. Wang, F. Zhang, Z. Lu, S. Lin, L. Chrostowski, and N. A. Jaeger, "Broadband 2× 2 adiabatic 3 db coupler using silicon-on-insulator sub-wavelength grating waveguides," *Optics Letters*, vol. 41, no. 13, pp. 3041–3044, 2016.

[94] Y. Wang, Z. Lu, M. Ma, H. Yun, F. Zhang, N. A. Jaeger, and L. Chrostowski, "Compact broadband directional couplers using subwavelength gratings," *IEEE Photonics Journal*, vol. 8, no. 3, pp. 1–8, 2016.

[95] L. Liu, Q. Deng, and Z. Zhou, "Subwavelength-grating-assisted broadband polarization-independent directional coupler," *Optics Letters*, vol. 41, no. 7, pp. 1648–1651, 2016.

[96] R. Halir, A. Maese-Novo, A. Ortega-Moñux, I. Molina-Fernández, J. Wangüemert-Pérez, P. Cheben, D.-X. Xu, J. Schmid, and S. Janz, "Colorless directional coupler with dispersion engineered sub-wavelength structure," *Optics Express*, vol. 20, no. 12, pp. 13 470–13 477, 2012.

[97] V. Donzella, A. Sherwali, J. Flueckiger, S. M. Grist, S. T. Fard, and L. Chrostowski, "Design and fabrication of SOI micro-ring resonators based on sub-wavelength grating waveguides," *Optics Express*, vol. 23, no. 4, pp. 4791–4803, 2015.

[98] J. Flueckiger, S. Schmidt, V. Donzella, A. Sherwali, D. M. Ratner, L. Chrostowski, and K. C. Cheung, "Sub-wavelength grating for enhanced ring resonator biosensor," *Optics Express*, vol. 24, no. 14, pp. 15 672–15 686, 2016.

[99] Z. Cheng, X. Chen, C. Y. Wong, K. Xu, and H. K. Tsang, "Mid-infrared suspended membrane waveguide and ring resonator on silicon-on-insulator," *IEEE Photonics Journal*, vol. 4, no. 5, pp. 1510–1519, 2012.

[100] Z. Wang, X. Xu, D. Fan, Y. Wang, and R. T. Chen, "High quality factor subwavelength grating waveguide micro-ring resonator based on trapezoidal silicon pillars," *Optics Letters*, vol. 41, no. 14, pp. 3375–3378, 2016.

[101] H. Yan, L. Huang, X. Xu, S. Chakravarty, N. Tang, H. Tian, and R. T. Chen, "Unique surface sensing property and enhanced sensitivity in microring resonator biosensors based on subwavelength grating waveguides," *Optics Express*, vol. 24, no. 26, pp. 29 724–29 733, 2016.

[102] L. Huang, H. Yan, X. Xu, S. Chakravarty, N. Tang, H. Tian, and R. T. Chen, "Improving the detection limit for on-chip photonic sensors based on subwavelength grating racetrack resonators," *Optics Express*, vol. 25, no. 9, pp. 10 527–10 535, 2017.

[103] J. Wang, I. Glesk, and L. R. Chen, "Subwavelength grating filtering devices," *Optics Express*, vol. 22, no. 13, pp. 15 335–15 345, 2014.

[104] Z. Tu, D. Gao, M. Zhang, and D. Zhang, "High-sensitivity complex refractive index sensing based on fano resonance in the subwavelength grating waveguide micro-ring resonator," *Optics Express*, vol. 25, no. 17, pp. 20 911–20 922, 2017.

[105] A. Ortega-Monux, L. Zavargo-Peche, A. Maese-Novo, I. Molina-Fernández, R. Halir, J. Wangüemert-Pérez, P. Cheben, and J. Schmid, "High-performance multimode interference coupler in silicon waveguides with subwavelength structures," *IEEE Photonics Technology Letters*, vol. 23, no. 19, pp. 1406–1408, 2011.

[106] A. Maese-Novo, R. Halir, S. Romero-García, D. Pérez-Galacho, L. Zavargo-Peche, A. Ortega-Moñux, I. Molina-Fernández, J. Wangüemert-Pérez, and P. Cheben, "Wavelength independent multimode interference coupler," *Optics Express*, vol. 21, no. 6, pp. 7033–7040, 2013.

[107] A. Ortega-Moñux, C. Alonso-Ramos, A. Maese-Novo, R. Halir, L. Zavargo-Peche, D. Pérez-Galacho, I. Molina-Fernández, J. G. Wangüemert-Pérez, P. Cheben, J. H. Schmid *et al.*, "An ultra-compact multimode interference coupler with a subwavelength grating slot," *Laser & Photonics Reviews*, vol. 7, no. 2, pp. L12–L15, 2013.

[108] J. Yang and Z. Zhou, "Double-structure, bidirectional and polarization-independent subwavelength grating beam splitter," *Optics Communications*, vol. 285, no. 6, pp. 1494–1500, 2012.

[109] Y. Xu and J. Xiao, "Compact and high extinction ratio polarization beam splitter using subwavelength grating couplers," *Optics Letters*, vol. 41, no. 4, pp. 773–776, 2016.

[110] S.-H. Jeong, D. Shimura, T. Simoyama, M. Seki, N. Yokoyama, M. Ohtsuka, K. Koshino, T. Horikawa, Y. Tanaka, and K. Morito, "Low-loss, flat-topped and spectrally uniform silicon-nanowire-based 5th-order CROW fabricated by arf-immersion lithography process on a 300-mm SOI wafer," *Optics express*, vol. 21, no. 25, pp. 30 163–30 174, 2013.

[111] D. M. Beggs, T. P. White, L. O'Faolain, and T. F. Krauss, "Ultracompact and low-power optical switch based on silicon photonic crystals," *Optics letters*, vol. 33, no. 2, pp. 147–149, 2008.

[112] T. Lee, D. Lee, and Y. Chung, "Design and simulation of fabrication-error-tolerant triplexer based on cascaded mach–zehnder inteferometers," *IEEE Photonics Technology Letters*, vol. 20, no. 1, pp. 33–35, 2007.

[113] M. Thorhauge, L. H. Frandsen, and P. I. Borel, "Efficient photonic crystal directional couplers," *Optics letters*, vol. 28, no. 17, pp. 1525–1527, 2003.

[114] L. Xu, Y. Wang, A. Kumar, D. Patel, E. El-Fiky, Z. Xing, R. Li, and D. V. Plant, "Polarization beam splitter based on mmi coupler with swg birefringence engineering on SOI," *IEEE Photonics Technology Letters*, vol. 30, no. 4, pp. 403–406, 2018.

[115] J. Wang, I. Glesk, and L. Chen, "Subwavelength grating Bragg grating filters in silicon-on-insulator," *Electronics Letters*, vol. 51, no. 9, pp. 712–714, 2015.

[116] J. Wang, R. Ashrafi, R. Adams, I. Glesk, I. Gasulla, J. Capmany, and L. R. Chen, "Subwavelength grating enabled on-chip ultra-compact optical true time delay line," *Scientific Reports*, vol. 6, p. 30235, 2016.

[117] J. Čtyrokỳ, J. G. Wangüemert-Pérez, P. Kwiecien, I. Richter, J. Litvik, J. H. Schmid, Í. Molina-Fernández, A. Ortega-Moñux, M. Dado, and P. Cheben, "Design of narrowband Bragg spectral filters in subwavelength grating metamaterial waveguides," *Optics Express*, vol. 26, no. 1, pp. 179–194, 2018.

[118] D. Charron, J. St-Yves, O. Jafari, S. LaRochelle, and W. Shi, "Subwavelength-grating contradirectional couplers for large stopband filters," *Optics Letters*, vol. 43, no. 4, pp. 895–898, 2018.

[119] B. Naghdi and L. R. Chen, "Silicon photonic contradirectional couplers using subwavelength grating waveguides," *Optics Express*, vol. 24, no. 20, pp. 23 429–23 438, 2016.

[120] B. Liu, Y. Zhang, Y. He, X. Jiang, J. Peng, C. Qiu, and Y. Su, "Silicon photonic bandpass filter based on apodized subwavelength grating with high suppression ratio and short coupling length," *Optics Express*, vol. 25, no. 10, pp. 11 359–11 364, 2017.

[121] B. Naghdi and L. R. Chen, "Spectral engineering of subwavelength-grating-based contradirectional couplers," *Optics Express*, vol. 25, no. 21, pp. 25 310–25 317, 2017.

[122] J. G. Wangüemert-Pérez, P. Cheben, A. Ortega-Moñux, C. Alonso-Ramos, D. Pérez-Galacho, R. Halir, I. Molina-Fernández, D.-X. Xu, and J. H. Schmid, "Evanescent field waveguide sensing with subwavelength grating structures in silicon-on-insulator," *Optics Letters*, vol. 39, no. 15, pp. 4442–4445, 2014.

[123] E. Luan, H. Yun, L. Laplatine, Y. Dattner, D. M. Ratner, K. C. Cheung, and L. Chrostowski, "Enhanced sensitivity of subwavelength multibox waveguide microring resonator label-free biosensors," *IEEE Journal of Selected Topics in Quantum Electronics*, vol. 25, no. 3, pp. 1–11, 2019.

[124] S. Chandran, "Integrated optical microring resonator in SOI for wide range refractive index sensing," Ph.D. dissertation, 2017.

[125] P. Sah, "Integrated photonic filters with distributed Bragg reflector in silicon on insulator," Ph.D. dissertation, 2018.

[126] K. Ramesh, "Broadband silicon photonics devices with wavelength independent directional couplers," Ph.D. dissertation, 2019.

[127] A. Yariv *et al.*, *Optical electronics in modern communications*. Oxford University Press, USA, 1997, vol. 1.

[128] P. Sah and B. K. Das, "Integrated optical rectangular-edge filter devices in SOI," *IEEE/OSA Journal of Lightwave Technology*, vol. 35, no. 2, pp. 128–135, 2017.

[129] A. Yariv and P. Yeh, "Photonics," 2007.

[130] M. Yamada and K. Sakuda, "Analysis of almost-periodic distributed feedback slab waveguides via a fundamental matrix approach," *Applied optics*, vol. 26, no. 16, pp. 3474–3478, 1987.

[131] M. Gnan, W. Hopman, G. Bellanca, R. De Ridder, R. De La Rue, and P. Bassi, "Closure of the stop-band in photonic wire Bragg gratings," *Optics Express*, vol. 17, no. 11, pp. 8830–8842, 2009.

[132] D. Pérez-Galacho, R. Halir, L. Zavargo-Peche, J. Wangüemert-Pérez, A. Ortega-Moñux, I. Molina-Fernández, and P. Cheben, "Adiabatic transitions for subwavelength grating waveguides," in *European Conference on Integrated Optics (ECIO)*, 2012.

[133] Y. Qin, Y. Yu, W. Wu, and X. Zhang, "Integrated tunable optical add/drop filter for polarization and wavelength multiplexed signals," *Optics Express*, vol. 24, no. 7, pp. 7069–7078, 2016.

[134] H. Li, Y. Bai, X. Dong, E. Li, Y. Li, Y. Liu, and W. Zhou, "Optimal design of an ultrasmall SOI-based $1\times$ 8 flat-top AWG by using an MMI," *The Scientific World Journal*, vol. 2013, 2013.

[135] K. Debnath, K. Welna, M. Ferrera, K. Deasy, D. G. Lidzey, and L. O'Faolain, "Highly efficient optical filter based on vertically coupled photonic crystal cavity and bus waveguide," *Optics Letters*, vol. 38, no. 2, pp. 154–156, 2013.

[136] A. D. Simard and S. LaRochelle, "Complex apodized Bragg grating filters without circulators in silicon-on-insulator," *Optics Express*, vol. 23, no. 13, pp. 16 662–16 675, 2015.

[137] W. Shi, H. Yun, C. Lin, M. Greenberg, X. Wang, Y. Wang, S. T. Fard, J. Flueckiger, N. A. Jaeger, and L. Chrostowski, "Ultra-compact, flat-top demultiplexer using anti-reflection contra-directional couplers for CWDM networks on silicon," *Optics Express*, vol. 21, no. 6, pp. 6733–6738, 2013.

[138] S. Romero-García, A. Moscoso-Mártir, J. Müller, B. Shen, F. Merget, and J. Witzens, "Wideband multi-stage crow filters with relaxed fabrication tolerances," *Optics express*, vol. 26, no. 4, pp. 4723–4737, 2018.

[139] Z. Qiang, W. Zhou, and R. A. Soref, "Optical add-drop filters based on photonic crystal ring resonators," *Optics express*, vol. 15, no. 4, pp. 1823–1831, 2007.

[140] M. G. Saber, Z. Xing, D. Patel, E. El-Fiky, N. Abadía, Y. Wang, M. Jacques, M. Morsy-Osman, and D. V. Plant, "A CMOS compatible ultracompact silicon photonic optical add-drop multiplexer with misaligned sidewall Bragg gratings," *IEEE Photonics Journal*, vol. 9, no. 3, pp. 1–10, 2017.

[141] D. Pérez-Galacho, D. Marris-Morini, A. Ortega-Moñux, J. Wangüemert-Pérez, and L. Vivien, "Add/drop mode-division multiplexer based on a Mach–Zehnder interferometer and periodic waveguides," *IEEE Photonics Journal*, vol. 7, no. 4, pp. 1–7, 2015.

[142] R. K. Gupta, S. Chandran, and B. K. Das, "Wavelength-independent directional couplers for integrated silicon photonics," *Journal of Lightwave Technology*, vol. 35, no. 22, pp. 4916–4923, 2017.

[143] S. Kaushal and B. K. Das, "Modeling and experimental investigation of an integrated optical microheater in silicon-on-insulator," *Applied Optics*, vol. 55, no. 11, pp. 2837–2842, 2016.

[144] R. K. Gupta and B. K. Das, "Performance analysis of metal-microheater integrated silicon waveguide phase-shifters," *OSA Continuum*, vol. 1, no. 2, pp. 703–714, 2018.

[145] S. Chandran, R. K. Gupta, and B. K. Das, "Dispersion enhanced critically coupled ring resonator for wide range refractive index sensing," *IEEE Journal of Selected Topics in Quantum Electronics*, vol. 23, no. 2, pp. 424–432, March 2017.

[146] J. Wang and L. R. Chen, "Low crosstalk Bragg grating/Mach-Zehnder interferometer optical add-drop multiplexer in silicon photonics," *Optics express*, vol. 23, no. 20, pp. 26 450–26 459, 2015.

[147] X. Wang, J. Zhang, E. H. Chan, X. Feng, and B.-o. Guan, "Ultra-wide bandwidth photonic microwave phase shifter with amplitude control function," *Optics Express*, vol. 25, no. 3, pp. 2883–2894, 2017.

[148] H.-Y. Chen, N. Kaneda, J. Lee, J. Chen, and Y.-K. Chen, "Optical filter requirements in an eml-based single-sideband pam4 intensity-modulation and direct-detection transmission system," *Optics Express*, vol. 25, no. 6, pp. 5852–5860, 2017.

[149] S. Bandyopadhyay, P. Biswas, A. Pal, S. K. Bhadra, and K. Dasgupta, "Empirical relations for design of linear edge filters using apodized linearly chirped fiber Bragg grating," *Journal of Lightwave Technology*, vol. 26, no. 24, pp. 3853–3859, 2008.

[150] M. Matsuhara and K. Hill, "Optical-waveguide band-rejection filters: Design," *Applied Optics*, vol. 13, no. 12, pp. 2886–2888, 1974.

[151] P. Cross and H. Kogelnik, "Sidelobe suppression in corrugated-waveguide filters," *Optics Letters*, vol. 1, no. 1, pp. 43–45, 1977.

[152] D. Wiesmann, C. David, R. Germann, D. Emi, and G. Bona, "Apodized surface-corrugated gratings with varying duty cycles," *IEEE Photonics Technology Letters*, vol. 12, no. 6, pp. 639–641, 2000.

[153] I. Giuntoni, D. Stolarek, J. Bruns, L. Zimmermann, B. Tillack, and K. Petermann, "Integrated dispersion compensator based on apodized SOI Bragg gratings," *IEEE Photonics Technology Letters*, vol. 25, no. 14, pp. 1313–1316, 2013.

[154] V. Veerasubramanian, G. Beaudin, A. Giguere, B. Le Drogoff, V. Aimez, and A. G. Kirk, "Design and demonstration of apodized comb filters on SOI," *IEEE Photonics Journal*, vol. 4, no. 4, pp. 1133–1139, 2012.

[155] J. Hastings, M. H. Lim, J. Goodberlet, and H. I. Smith, "Optical waveguides with apodized sidewall gratings via spatial-phase-locked electron-beam lithography," *Journal of Vacuum Science & Technology B: Microelectronics and Nanometer Structures Processing, Measurement, and Phenomena*, vol. 20, no. 6, pp. 2753–2757, 2002.

[156] M. Strain and M. Sorel, "Integrated III–V Bragg gratings for arbitrary control over chirp and coupling coefficient," *IEEE Photonics Technology Letters*, vol. 20, no. 22, pp. 1863–1865, 2008.

[157] V. Mizrahi and J. E. Sipe, "Optical properties of photosensitive fiber phase gratings," *J. Lightw. Technol.*, vol. 11, no. 10, pp. 1513–1517, 1993.

[158] L. M. Lechuga, "Optical biosensors," *Comprehensive Analytical Chemistry*, vol. 44, pp. 209–250, 2005.

[159] K. Qin, S. Hu, S. T. Retterer, I. I. Kravchenko, and S. M. Weiss, "Slow light Mach-Zehnder interferometer as label-free biosensor with scalable sensitivity," *Optics Letters*, vol. 41, no. 4, pp. 753–756, 2016.

[160] K. Kim and T. E. Murphy, "Porous silicon integrated Mach-Zehnder interferometer waveguide for biological and chemical sensing," *Optics Express*, vol. 21, no. 17, pp. 19 488–19 497, 2013.

[161] Q. Liu, X. Tu, K. W. Kim, J. S. Kee, Y. Shin, K. Han, Y.-J. Yoon, G.-Q. Lo, and M. K. Park, "Highly sensitive Mach–Zehnder interferometer biosensor based on silicon nitride slot waveguide," *Sensors and Actuators B: Chemical*, vol. 188, pp. 681–688, 2013.

[162] V. Passaro, C. Tullio, B. Troia, M. Notte, G. Giannoccaro, and F. Leonardis, "Recent advances in integrated photonic sensors," *Sensors*, vol. 12, no. 11, pp. 15 558–15 598, 2012.

[163] J. R. Bickford, P. Cho, M. E. Farrell, E. L. Holthoff, and P. Pellegrino, "The investigation of subwavelength grating waveguides for photonic integrated circuit based sensor applications," *IEEE Journal of Selected Topics in Quantum Electronics*, 2019.

[164] A. Hosseini, D. N. Kwong, Y. Zhang, H. Subbaraman, X. Xu, and R. T. Chen, "1$\times$ n multimode interference beam splitter design techniques for on-chip optical interconnections," *IEEE Journal of Selected Topics in Quantum Electronics*, vol. 17, no. 3, pp. 510–515, 2011.

[165] L. B. Soldano and E. C. Pennings, "Optical multi-mode interference devices based on self-imaging: principles and applications," *Journal of Lightwave Technology*, vol. 13, no. 4, pp. 615–627, 1995.

[166] A. Densmore, D.-X. Xu, S. Janz, P. Waldron, T. Mischki, G. Lopinski, A. Delâge, J. Lapointe, P. Cheben, B. Lamontagne *et al.*, "Spiral-path high-sensitivity silicon photonic wire molecular sensor with temperature-independent response," *Optics letters*, vol. 33, no. 6, pp. 596–598, 2008.

[167] A. Densmore, D.-X. Xu, P. Waldron, S. Janz, P. Cheben, J. Lapointe, A. Delge, B. Lamontagne, J. Schmid, and E. Post, "A silicon-on-insulator photonic wire based evanescent field sensor," *IEEE Photonics Technology Letters*, vol. 18, no. 23, pp. 2520–2522, 2006.

[168] R. Kumar, J. R. Ong, J. Recchio, K. Srinivasan, and S. Mookherjea, "Spectrally multiplexed and tunable-wavelength photon pairs at 1.55 μm from a silicon coupled-resonator optical waveguide," *Optics Letters*, vol. 38, no. 16, pp. 2969–2971, 2013.

[169] W. C. Hopman, P. Pottier, D. Yudistira, J. Van Lith, P. V. Lambeck, R. M. De La Rue, A. Driessen, H. J. Hoekstra, and R. M. De Ridder, "Quasi-one-dimensional photonic crystal as a compact building-block for refractometric optical sensors," *IEEE journal of selected topics in quantum electronics*, vol. 11, no. 1, pp. 11–16, 2005.

[170] Y. Zhao and Y. Liao, "Discrimination methods and demodulation techniques for fiber Bragg grating sensors," *Optics and Lasers in Engineering*, vol. 41, no. 1, pp. 1–18, 2004.